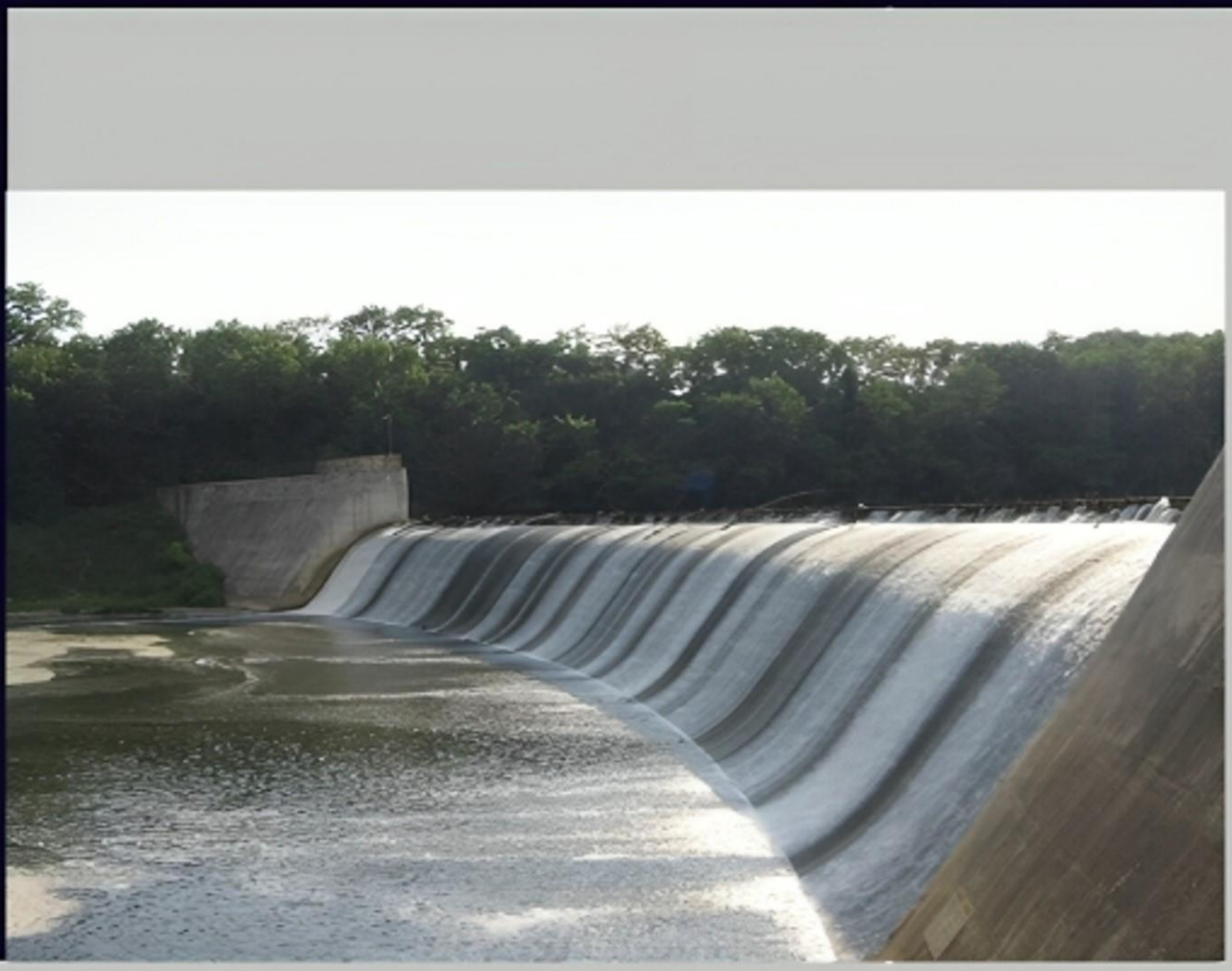
Iranian Hydraulic Association

Shahid Chamran University of Ahvaz

Journal of Hydraulic Structures

Scientific Professional Journal



April 2024
Volume 10, Issue 2

ISSN (Online): 2345-4156
https://jhs.scu.ac.ir/

Aims and Scope

Journal of Hydraulic Structures is an interdisciplinary journal which publishes high-quality peer-reviewed articles addressing the latest developments and applied methods in analysis and design, construction, maintenance, management, and operation policy of Hydraulic Structures.

The Journal aims at providing an efficient route to fast-track publication, within 10-12 weeks after manuscript submission.

The general areas covered by the Journal include:

- Advances in numerical and analytical methods applicable to hydraulic structures
- Hydro informatics and soft computing
- Hydraulic aspects of hydraulic structures
- Applied surface and subsurface hydrology and hydrometeorology
- Forecasting approaches in water resources engineering
- Economic and social aspects of hydraulic structures
- Uncertainty analysis and risk management in hydraulics and water resources engineering
- Application of Nanotechnology in hydraulic structures
- Geotechnics of hydraulic structures
- Damage detection techniques
- Technical and methodological advances in application, design/selection, production, construction materials of hydraulic structures.
- Application of Artificial Intelligence techniques in all aspects of hydraulic structures.

General Information:

Title: Journal of Hydraulic Structures

Publisher: Shahid Chamran University of Ahvaz

ISSN (Print): 2345-413X

ISSN (Online): 2345-4156

Website: https://jhs.scu.ac.ir/

Address: Faculty of Civil Engineering and Architecture, Shahid Chamran University of Ahvaz, Ahvaz, Iran

Email: jhs@scu.ac.ir

Journal of

Hydraulic Structures

Shahid Chamran University of Ahvaz

Director-in-Charge: Prof. Ali Haghighi

Editor-in-Chief: Prof. Hamid R. Ghafouri

Managing Editor: Dr. Amir H. Shafiee

Contents:

01 Editorial: Special Issue of 22nd Iranian Conference on Hydraulics

Hamid R. Ghafouri

02

Predicting Morphological Changes in Rivers Using Image Processing (Case Study: Qizil Ouzan River)

Jafar Chabokpour; Morteza Raji

11

Performance Evaluation of Artificial Intelligence Models in Estimating the Discharge Coefficient of Labyrinth Weirs with Semicircular Crests

Hamed Heydarzadeh; Sarvenaz Asef; Jafar Chabokpour; Reza Norouzi

20

Laboratory investigation of the removal pattern of salinity from the base of coastal reservoirs during the first water impounding

Shaghayegh Pourbabak; Hojjat Ahmadi; Amir Raouf; Shuqing Yang

30

Modeling of discharge Coefficient of nonlinear weirs with QNET and SVM methods

Mahdi Majedi-Asl; Tohid Omidpour Alavian; Yousef Seyfari; Mehdi Kouhdaragh

46

Investigating and predicting hydraulic jump energy loss with threshold (Experimental and regression analysis)

Hamidreza Abbaszadeh; Parisa Ebadzadeh; Rasoul Daneshfaraz; Reza Norouzi

55

Reducing the extent of vortices upstream of the sliding valve

Parisa Ebadzadeh; Hamidreza Abbaszadeh; Rasoul Daneshfaraz; Reza Norouzi

Journal of

Hydraulic Structures

Shahid Chamran University of Ahvaz

Director-in-Charge: Prof. Ali Haghighi

Editor-in-Chief: Prof. Hamid R. Ghafouri

Managing Editor: Dr. Amir H. Shafiee

Contents:

62

Determining Thermal Stratification of Zayandeh Roud Dam Reservoirs Using Two-Dimensional CE-QUAL-W2 Model

Negar Varshabi; Ramtin Moeini

72

Investigating sediment changes during dry and wet periods at both upstream and downstream stations of the Karkheh Dam

Somayeh Rezaeimanesh; Sara Parvizi; Ali Talebi

82

Laboratory investigation of the effect of hysteresis phenomenon of supercritical flow on the rough bed on the relative residual energy parameter

Ehsan Aminvash; Rasoul Daneshfaraz; Sina Sadeghfam; Seyed Bahman Mousavi

93

Mapping Vulnerability of aquifer to saltwater intrusion using fuzzy membership function

Marjan Moazamnia; Sina Sadeghfam; Alireza Babaeian Amini

106

Numerical investigation on the hydraulic parameters' effects on the circular-crested weir

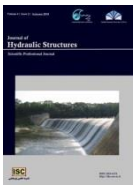
Mahdi Majedi-Asl; Hadi Arvanaghi; Mehdi Fuladipanah; Omid Ghasemzadeh; Tohid Omidpour Alavian

119

The effect of slot in reducing scour depth of cylindrical bridge pier using Flow3D software

Milad Kazemian; Kazem Esmaeili

Journal of Hydraulic Structures
J. Hydraul. Struct., 2024;10(2):1-1
DOI: 10.22055/jhs.2024.19072



OPEN ACCESS

Editorial: Special Issue of 22nd Iranian Conference on Hydraulics

Hamid Reza Ghafouri [*1]

Chief Editor's Word

During almost a decade of publication, the Journal of Hydraulic Structures (JHS) has tried to fulfill its mission of expanding engineering knowledge in related specialized fields, acting as a bridge between academic experts and executive engineers. For this purpose, in addition to receiving, reviewing and publishing high quality scientific articles that contain the latest scientific achievements in the specialized field of the journal, from now on it will try to play its role in expanding the frontiers of knowledge by publishing the selected articles of prestigious specialized conferences. This is because due to the high speed of scientific advances on the one hand, and the relatively lengthy process of writing, submitting, reviewing and publishing articles in scientific journals on the other hand, many developments in scientific fields are exposed to interested people with a relatively long delay in specialized publications, while such articles are usually presented at a faster rate in specialized conferences and meetings. Therefore, it would be good to publish a selection of the premier articles presented in prestigious conferences in JHS to facilitate publicizing the latest scientific achievements in the field.

Based on this idea, the Journal of Hydraulic Structures, through an agreement with the 22nd Iranian Conference on Hydraulics (Nov. 2023), which is one of the most prestigious national conferences in this field, agreed that the selected articles of this conference, which were peer-reviewed by the reviewers board of the conference, be published in the form of a special issue. The present collection, which was selected by the conference as the premier articles, is made available outside of the usual reviewing process of the journal and under the responsibility of the conference jury. We hope that it would be of interest to the JHS's readers.

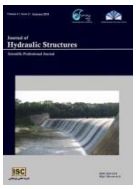
Editor-in-Chief
Journal of Hydraulic Structures

Received: 19 April 2024; Accepted: 19 April 2024

[*] Email: ghafouri_h@scu.ac.ir
[1] Department of Civil Engineering, Faculty of Civil Engineering and Architecture, Shahid Chamran University of Ahvaz, Ahvaz, Iran.

CC BY

Journal of Hydraulic Structures
J. Hydraul. Struct., 2024;10(2):2-10
DOI: 10.22055/jhs.2024.19037



OPEN ACCESS

Predicting Morphological Changes in Rivers Using Image Processing (Case Study: Qizil Ouzan River)

Jafar Chabokpour [*1]
Morteza Raji [1]

Abstract

Morphological studies are among the most important topics in river engineering, dealing with the geometric shape, bed form, and longitudinal profile of the waterway, cross-sections, deformations, and lateral migration of rivers over time. Researchers worldwide have noted the capability of satellite imagery and its integration with geographic information systems (GIS) to provide comprehensive information about river conditions and monitor spatial changes at different time intervals. In this paper, a new method is proposed to detect the current morphology of different parts of the Qizil Ouzan river and its main branches using a CNN neural network with support vector machine (SVM) and multilayer perceptron (MLP). The results of the studies show that the current meander length of the river is more than anything else the result of non-river factors such as stream piracy and mass movements like landslides and lateral collapses of waterways. Moreover, using GIS software, the meander and its changes over different time periods were obtained and compared with each other. Also, the present research aims to predict river morphological changes using image processing in MATLAB. The results demonstrate the efficacy of combining these two methods for predicting the morphological changes of the Qizil Ouzan River.

Keywords: River Bed, Image Processing, Prediction, Morphology, Sediments.

Received: 09 November 2023; Accepted: 16 April 2024

[*] E-mail: J.chabokpour@maragheh.ac.ir (**Corresponding Author**)
[1] Department of Civil Engineering, Faculty of Engineering, University of Maragheh, Maragheh, Iran.

CC BY

1. Introduction

The study of predicting morphological changes in rivers and investigating the influence of various factors on channel shape and structure is of great importance. Such studies can provide valuable insights into river behavior and how they respond to changes. The application of image processing techniques for analyzing data related to channel shape and structure can provide a powerful tool for better understanding river dynamics. It is important to identify factors influencing channel shape, including tectonic activities, slope processes, lithology, and the geological structure of the area using high-quality images with appropriate resolution for analyzing channel shape details. By conducting such studies, better planning and management of watersheds, prevention of potential hazards such as floods, and erosion control can be achieved. Furthermore, a deeper understanding of the geomorphological processes of rivers will be gained. Rivers, as natural conduits for collecting and transporting atmospheric precipitation that flows across the Earth's surface, have always been the focus of human communities. Major and minor civilizations throughout history have emerged and endured alongside these life-giving natural phenomena [1-4]. The lives, work, and efforts of many people have been directly dependent on river water, benefiting from its natural bounties. Providing drinking water and irrigation has been the primary need of human communities along riverbanks. However, many civilizations have also faced the indifference and wrath of nature throughout history. In numerous instances, floods and inundations, as well as erosion of riverbeds and banks, have inflicted significant damage on agricultural lands and the homes and dwellings of riparian residents [5]. Therefore, it is necessary to strive to understand the factors influencing erosion and changes in the natural course of rivers. Rivers and waterways are highly dynamic systems, and their position, shape, and other morphological characteristics are continuously changing over time A combination of factors, such as channel slope, flow rate, bed material characteristics, frequency and intensity of floods, etc., determine the morphology of a river in space and time [6]. In this regard, Leopold and Wolman [7] classified river morphological structures into three categories: straight, meandering, and braided, which are influenced by these factors. Among these patterns, the meandering pattern has attracted the most attention due to its prevalence in nature [8]. The river ecosystem is highly dynamic, and its lateral boundaries and morphological characteristics are continuously changing over time [9-10]. Monitoring morphological changes is the basis and foundation for solving applied geomorphological problems, and identifying and designing their processes is essential. Geomorphologists, to understand the nature and rate of changes, describe the past and present as a necessary principle and predict the future of processes [11]. On the other hand, geomorphological studies are among the most important topics in river engineering, dealing with the geometric shape, bed form, longitudinal profile of the waterway, cross-sections, deformations, and lateral migration of rivers over time [12]. Researchers worldwide have noted the capability of satellite imagery and its integration with geographic information systems (GIS) to provide comprehensive information about river conditions and monitor spatial changes at different time intervals [13-18]. Today, advances in image processing science have made it possible to calculate the morphological characteristics of rivers through photography. Due to the lack of geotechnical and soil mechanics studies (due to high costs and time-consuming nature) in many river engineering studies, image processing can be used as a suitable method for facilitating the extraction of bed material gradation curves and other particle characteristics [19]. Therefore, access to more accurate information about river morphology for hydraulic flow and flood modeling is provided, consequently increasing the accuracy of simulations.

2. Materials and methods

Qizil Ouzan is one of the longest rivers in Iran, originating from the Chehel Cheshme Mountains between Saqqez and Divandarreh in the Kurdistan and East Azerbaijan provinces. After joining the Hir River, Zanjan River, and Shahroud River, it flows into the Caspian Sea. In southern Gilan province, Qizil Ouzan merges with the flow of the Sepidrud Dam to form the large Sepidrud River. The Qizil Ouzan River passes through the western, northwestern, and northern parts of Zanjan province, forming border boundaries with Gilan, Ardabil, East Azerbaijan, West Azerbaijan, and Kurdistan provinces in some sections (Figs. 1 and 2). For this study, initially, a section of the Qizil Ouzan River between the coordinates (36°51'31.93"N, 48°57'24.57"E) and (36°52'14.30"N, 48°54'39.67"E), with an approximate length of 8,600 meters, was selected using Google Earth, and image processing was performed on that section.



Figure 1. Location of Qizil ouzan river



Figure 2. Google Earth image from one reaches of Qizil ouzan

3. Results

This paper utilizes a convolutional neural network (CNN). In this work, the Stochastic Gradient Descent (SGD) algorithm is used for training the CNN. The number of hidden layers of the neural network is set to 200. The Database folder contains images of the Qizil Ouzan River for four consecutive years from 2018 to 2021, which are used to obtain an estimate for the year 2022. For simplicity and faster processing, grayscale versions of the images are used. This work is carried out using a deep neural network. To run the processing, it is sufficient to execute the main code and wait for the features to be extracted and the results to be displayed. The implementation was done in MATLAB 2019a. The quantitative metrics used for evaluating the simulation results include classification accuracy, false positive rate, and specificity. The classification accuracy is obtained by calculating the confusion matrix. The confusion matrix is a square matrix of size C × C, where C is the number of classes. The main diagonal of this matrix contains the correctly classified samples, and the off-diagonal elements represent the samples that are incorrectly assigned to a class other than their true class. After calculating the confusion matrix, the classification accuracy and two other quantitative metrics are defined by the following Eqs. 1, and 2.

$$\mathrm{FPR} = \mathrm{FalsePositiveRate} = \frac{\mathrm{FP}}{\mathrm{FP} + \mathrm{TN}} \tag{1}$$

$$\mathrm{Specificity} = \frac{\mathrm{TN}}{\mathrm{FP} + \mathrm{TN}} \tag{2}$$

Where:

- False Positive: A result that is declared correct but is incorrectly declared correct.
- False Negative: An incorrect result that is wrongly or erroneously declared as an error.
- True Positive: A result that is declared correct and is indeed correct.
- True Negative: A result that is declared incorrect and is indeed incorrect.

3.1. Pre-processing and Image Segmentation

As mentioned earlier, before applying the satellite images of the region to the deep neural network, pre-processing steps need to be performed on the images to obtain the region of interest (ROI). In this paper, we will work on different sections for pre-processing. The general steps of pre-processing are also shown in Fig. 3. The flowchart depicts the main steps involved in a pre-processing for image data. The first step is to remove environmental noises and distortions that may be present in the raw data. Next, noises or unwanted artifacts from the surrounding areas are removed. Finally, the image quality is enhanced, and the Region of Interest (ROI) is extracted from the pre-processed image for further analysis or processing. In the second stage, the areas surrounding the river are removed using the region growing method. In this paper, the automatic seed point selection method is used. In this method, neighboring pixels are continuously examined to determine whether they should be added to the region, and this process continues until the complete ROI is extracted. The final pre-processing stage involves image quality enhancement using the Wiener filter and CLAHE (Contrast Limited Adaptive Histogram Equalization) algorithms.

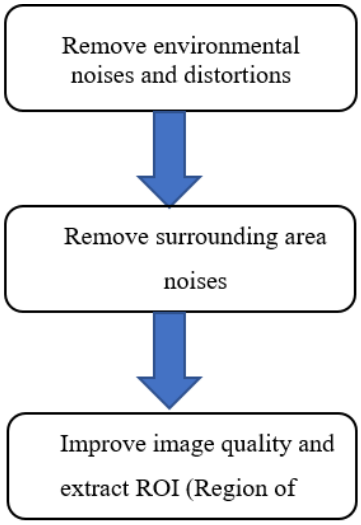


Figure 3. Preprocess flowchart for image processing

3.2. Results of Morphological Change Detection in the Region using CNN+(SVM+MLP)

Using the second fully connected layer in the convolutional neural network, a feature vector is obtained, and in this section, the results of applying this data to an SVM with a radial basis function kernel and an MLP neural network are presented. In this scenario, as before, 70% of the images were used for training and 30% for testing across all datasets. The test results of the trained network are presented in Table 1.

Table 1 - Quantitative Metric Results for Using CNN+(SVM+MLP) Method

Specificity	FPR	Classification accuracy (%)	Operated method
0.9532	0.0412	98.88	CNN+(SVM+MLP)

As observed in Table 1, the proposed method, which combines the CNN neural network with SVM and MLP, has been able to achieve higher performance and provide more desirable results. Based on this, it can be concluded that using the proposed method of this research, the detection of morphological changes in the region from satellite images is possible with an accuracy of 98.88%.

3.3. Simulation Codes

After determining the method, we move to the code written in MATLAB and execute it. After running, the neural network undergoes training. Depending on the system's speed and processor, this part may take several hours. In the end, the trained model is obtained (Fig. 4). The prediction for the year 2022 is performed here with the aid of a trained model. The final image is saved in black and white (Fig. 5).

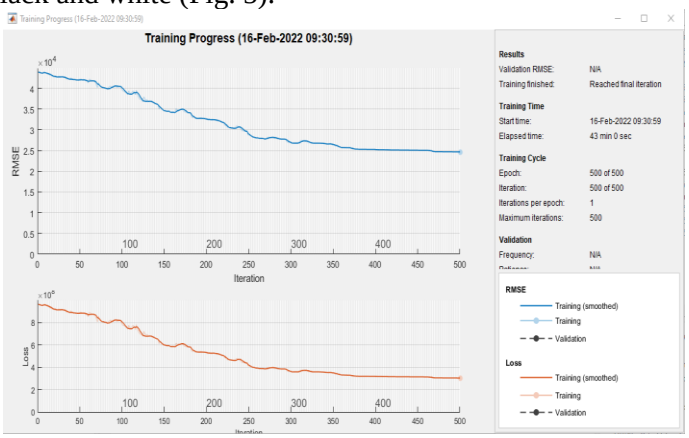


Figure 4. Trained model for image processing



Figure 5. Final output image after processing

3.4. Analysis of Some Morphological Changes

Next, we transfer the existing images in the database, as well as the final output, to ArcMap software version 10.6.1 to obtain some geomorphological properties, including the existing meander and its characteristics and the river length at that selected point, and compare them with each other. First, we GEOREFERENCE the aerial images of each year in the software separately, so that measurements at certain points are more accurate. Table 2 presents the river characteristics at a specific point and in different years for comparison. In general, any change in the loop of a meander bend, as well as a change in its geometric shape, necessitates erosion of the river banks. In all river meanders, a continuous process of erosion occurs with varying intensity on the concave or outer bank, and sediment deposition occurs on the convex or inner bank, forming point bar deposits. The cumulative effect of these two phenomena over time results in either the continuous displacement of the concave and convex bank apexes downstream or the lateral migration of the meanders perpendicular to the valley axis. In other words, there are two types of meander changes (i) Migration and progression downstream, (ii) Meander expansion and cut-off.

The actual movement of meanders in nature can be considered a combination of these two cases. Each of the above movements is also a combination of components of changes in the bends. Pure longitudinal movement in a meander results from the translation of the bend loop, while lateral movement is caused by the expansion of the bend. Both types of these changes often occur at specific locations in a meander. Meanders increase the flow length and decrease the slope. The phenomenon of meander formation can be considered as the general stages of the river's adjustment to the valley slope through which it flows. The geometry of a meander is formed by erosion and sedimentation.

Table 2. River reach characteristics during different years in fixed position

Image Year	River Length (m)	Meandering width (m)	Meandering amplitude (m)	Meandering length (m)
2010	5010	1851	1569	2043
2013	5067	2326	1925	2221
2018	5380	1949	1602	2036
2021	5410	2001	1980	2150
Final Image	5497	2361	2108	2285

In areas where the river has few bends, meander changes do not occur as cut-offs but rather as downstream migration. Since this phenomenon occurs systematically, the rate of downstream progression is regular and consistent. Based on this, the alternating movement of the meander from one bank to the other can be defined. The duration of this periodic movement depends on the return period of floods and the composition of bank materials. Therefore, this periodic movement can have different durations in different reaches of a river. However, the periodic time is usually constant within a given reach.

Based on the mentioned points and Table 2, it is observed that the changes in the meander or bend of the river over time follow an approximately constant periodic pattern. However, in 2018, the periodic and increasing changes observed in previous years have decreased and become lower than the previous year. But again, in the following year, the upward trend resumed and increased. These changes could be due to the occurrence of floods or land-use changes in the riverbed, and errors in calculations and measurements cannot be ruled out. Furthermore, the changes in the characteristics and shape of the meander over different time periods, as determined by the ArcGIS software, are shown as an example in Fig. 6.



Figure 6. Method of measurement of amplitude, length, and width of meandering

4. Conclusion

Nowadays, with the increasing expansion of various methods of acquiring discrete studies such as scanners and digital cameras, image processing has found extensive applications. The resulting images from this data are always more or less accompanied by some noise and in some cases suffer from the problem of blurring the boundaries of samples within the image, which leads to a reduction in the clarity of the received image. The set of operations and methods used to reduce defects and enhance the visual quality of the image is called image processing. In general, the information received from image signals must be in a way that is understandable for systems. Therefore, methods must be found to convert the signal into data that is comprehensible for the system. In general, signals are analog and digital, and in either case, they must go through stages to be converted into the desired information. After these conversions, the features extracted from the image are considered as vectors. If the vectors extracted from the images have large dimensions, dimensionality reduction must be performed on them so that the data separation and classification can be done better. The Ghazal Ouzan basin is one of the basins that has undergone many geomorphological changes in recent centuries. The continuation of tectonic activities (formation of compressional ridges), mass movements, and the influx of a large amount of slope materials into waterways, as well as the occurrence of intermittent droughts, land-use changes, and the occupation of the river bed along its long course, are among these changes. The results of the studies show that the current morphology of different parts of the Ghazal Ouzan river and its main branches is more than anything else the result of non-river factors such as stream piracy and mass movements like landslides and lateral collapses of waterways. In general, rivers in mountainous areas like the Qizil Ouzan river in the studied area always adapt themselves to the changes in the channel slope and slope processes, and that is why we encounter various forms of waterways in different parts of these rivers. Tectonic activities, glaciers, mass movements, and changes in lithology and structure, which directly affect the erodibility of the channel bed rock, are known as non-river factors influencing channel geometry. Along with these factors and based on the results of this research, the phenomenon of stream piracy should also be added to the above cases. Additionally, using GIS software, the meander length and its changes over different time periods were obtained and compared with each other. It was observed that combined methods improve classification performance. In addition, using the CNN network alone did not provide satisfactory performance, but the features of this network along with SVM led to a good improvement in classification accuracy.

References

1. Akhter, S., Eibek, K. U., Islam, S., Islam, A. R. M. T., Chu, R., & Shuanghe, S. (2019). Predicting spatiotemporal changes of channel morphology in the reach of Teesta River, Bangladesh using GIS and ARIMA modeling. *Quaternary International*, *513*, 80-94.
2. Karmaker, T., & Dutta, S. (2016). Prediction of short-term morphological change in large braided river using 2D numerical model. *Journal of Hydraulic Engineering*, *142*(10), 04016039.
3. Rostami, A., Raeini-Sarjaz, M., Chabokpour, J., Hazi, M.A. and Kumar, S., (2022). Determination of rainfed wheat agriculture potential through assimilation of remote sensing data with SWAT model case study: ZarrinehRoud Basin, Iran Water Supply 22 (5) 5331–5354.
4. Deng, B., Xiong, K., Huang, Z., Jiang, C., Liu, J., Luo, W., & Xiang, Y. (2022). Monitoring and Predicting Channel Morphology of the Tongtian River, Headwater of the Yangtze River Using Landsat Images and Lightweight Neural Network. Remote Sensing, 14(13), 3107.
5. Refahi, H., Water erosion and its control, University of Tehran, 4th edition, 671 pages, 1378. (In Persian)
6. Nikora, V., Goring, D., McEwan, I. & Griffiths, G. (2001). Spatially averaged open-channel flow over rough bed. Journal of Hydraulic Engineering, 027(2), 023–.033.
7. Leopold, L.B., & Wolman, M.G. (1957). River channel patterns-braided, meandering and straight. U.S. 15. Geological Survey. Professional Paper 282 p.
8. Biedenharn D.S., Elliot, C.M., & Watson, C.C. (1997). The WES stream investigation and stream bank stabilization handbook. U.S. Army Engineering. 286 p.
9. Kessler, A.C.; Satish, C. & Melinda, K. (2013), "Assessment of River Bank Erosion in Southern Minnesota Rivers Post European Settlement, Geomorphology".
10. Rostami, A., Raeini-Sarjaz, M., Chabokpour, J., & Chadee, A. A. (2023). Soil moisture monitoring by downscaling of remote sensing products using LST/VI space derived from MODIS products. Water Supply, 23(2), 688-705.
11. Cook, R.U. & Doornkamp, J.C. (1991), Geomorphology in Environment Management, Second Edition, Clarendon Press, Oxford.
12. Pan, S. (2013). "Application of Remote Sensing and GIS in Studying Changing River Course in Bankura District, West Bengal", International Journal of Geometrics and Geosciences, Vol. 4, Issue 0, pp.063-049.
13. Surian, N. (1999), "Channel Changes Due to River Regulation: The Case of the Piave River, Italy", Earth Surface Processes and Landforms, Vol. 24, No. 12, pp. 1135-1151.
14. Rinaldi, M. (2003), "Recent Channel Adjustments in Alluvial Rivers of Tuscany, Central Italy", Earth Surface Processes and Landforms, Vol. 28, No. 6, pp.618-587.
15. L. Q. Li, X. X. Lu & Z. Chen (2007), "River Channel Change during the Last 51Years in the Middle Yangtze
16. River: An Example of the Jianli Reach", Geomorphology, Vol. 85, No. 4-3, pp.196-185
17. Kummu, M.; Lub, X. X.; Rasphonec, A.; Sarkkulad, J. and Koponen J. (2008), "Riverbank Changes along the Mekong River: Remote Sensing Detection in the Vientiane-Nong Khai Area", Quaternary International, Vol. 186, No. 1, pp.18-1
18. Sarkar, A., Garg, R. D., & Sharma, N. (2012). "RS-GIS Based Assessment of River Dynamics of Brahmaputra River in India", Journal of Water Resource and Protection, Vol. 4, pp.72-63.

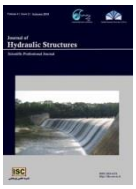
19. Annayat, W., & Sil, B. S. (2020). Assessing channel morphology and prediction of centerline channel migration of the Barak River using geospatial techniques. Bulletin of Engineering Geology and the Environment, 79(10), 5161-5183.
20. Azizian, A., Morshedi, F., & Arian, A. (2012). Utilization of image processing technique for obtaining surface material gradation curve of the riverbed. 9th River Engineering International Seminar, 24-22Jan., Shahid Chamran University, Ahvaz, Iran. (In Farsi).



© 2024 by the authors. Licensee SCU, Ahvaz, Iran. This article is an open access article distributed under the terms and conditions of the Creative Commons Attribution 4.0 International (CC BY 4.0 license) (http://creativecommons.org/licenses/by/4.0/).



Journal of Hydraulic Structures
J. Hydraul. Struct., 2024;10(2):11-19
DOI: 10.22055/jhs.2024.19038



OPEN ACCESS

Performance Evaluation of Artificial Intelligence Models in Estimating the Discharge Coefficient of Labyrinth Weirs with Semicircular Crests

Hamed Heydarzadeh [*1]
Sarvenaz Asef [1]
Jafar Chabokpour [1]
Reza Norouzi [1]

Abstract

In this study, the performance of ANN and SVM in estimation of the discharge coefficient of the labyrinth weirs with semicircular crests was investigated. For this purpose, 454 experimental data were used. Dimensionless parameters of HT/P, L/W, W/P, and a were introduced as inputs and CD parameters as outputs in the models. The performance of the ANN model with RMSE, R and, DC was 0.019, 0.971 and 0.971 respectively more acceptable and closer to the experimental data than the SVM model.

Keywords: Labyrinthine Weir, Artificial Neural Network, Support Vector Machines.

Received: 09 November 2023; Accepted: 16 April 2024

1. Introduction

The volume of flow through the weir is dependent on the length and shape of the weir, so far, a lot of research has been done on the effect of hydraulic and geometric parameters on discharge coefficient and discharge rate over weirs. One of the effective ways to increase the length of the weir at a given width is to use the weirs with nonlinear plan, such as triangular, trapezoidal plan, circular, parabolic and so on. As a result of the construction of this type of the weir will increase the volume of flow through them and lower free elevation will be required upstream than linear weirs. This is very important when it acts as a flood discharge structure and facilitates the flow of the flood [1, 2].

[*] E-mail: Hamedhv1373@gmail.com (**Corresponding Author**)
[1] Department of Civil Engineering, Faculty of Engineering, University of Maragheh, Maragheh, Iran.

CC BY

The first research on the labyrinth weir was conducted by [3] [3]. After the studies of Taylor (1968), Hay & Taylor, (1970) proposed a method for calculating the discharge and design of these weirs [4], and¬ followed another method for designing the labyrinth weirs. Juma et al., (2014) [5] analyzed the hydraulic properties of semicircular weirs using artificial neural networks (ANNs). They showed that the results of artificial neural networks were in good agreement with laboratory results. Goel, (2014) [6] used neural networks technique to predict the discharge and discharge coefficient of triangular weirs. This study showed that the results of ANN (MLP) performed better than the results and equations presented by Kumar et al., (2011) [7].

Roushangar et al., (2018) [8] investigated the discharge coefficient of labyrinth and arc weirs by using support vector regression. Their results showed that support vector regression method has high efficiency in determining the discharge coefficient of the labyrinth weirs. Karami et al., (2018) [9] examined rectangular labyrinthine weirs with models of vector machine [10, 11], artificial neural network and genetic algorithm. They examined the results of these models with laboratory data that provided better results than other models. (Gupta et al., (2014) [12] investigated the flow characteristics of the W-shaped weir in plan. The results showed that the efficiency of these weirs is better than conventional weirs. Using the laboratory data carried out in this study, equations were also presented for the discharge. These equations calculate the discharge value with 5% of fault fluctuations. The susceptibility of the weir to the water head was also investigated and the results showed that the weir is very sensitive in low and small apex angles.

According to the sources, it is observed that limited studies have been conducted with intelligent models to estimate the discharge coefficient of labyrinth weirs with semicircular crests. Therefore, in this study, using the laboratory data of [9], the performance of intelligent models of ANN and SVM in order to estimate the discharge coefficient of the labyrinth weir with a semicircular crest the study was conducted.

2. Methods

The one-dimensional flow equation on the labyrinth weirs is a function of total water charge (H_t), length of weir (L) and flow coefficient (C_D) without dimension and is obtained from relation 1 (Henderson, 1966).

$$Q = \frac{2}{3} CD\sqrt{2g}\, Lc\, H_t^{\frac{3}{2}} \quad (1)$$

Using dimensional analysis and considering geometrical, kinematic and dynamic parameters, the parameters affecting the flow coefficient in the labyrinth weirs include upstream water charge (Ht), weir nose length (A), effective crest length (Lc), total weir width (W), wall angle (a), weir height (P), weir thickness (tw) and the shape of the weir crest.

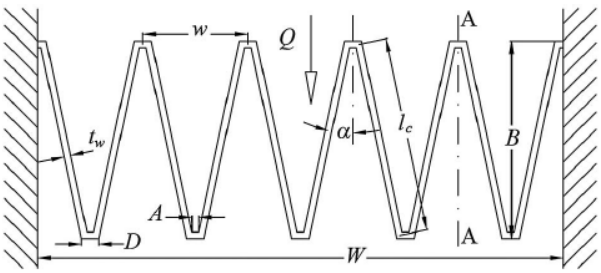


Figure 1. A view of the labyrinthine weir studied by Croston and Tullis (2013)

The data used in this study are the laboratory data of Kirkston and Tollis (2013). They have conducted studies on the labyrinth weirs with semicircular crests where the effective parameters are visible in Figure 1.

2.1. Artificial Neural Network (ANN)

Artificial neural networks (ANNs) consist of a number of neurons that are layered together in layers. Each artificial network consists of introductory, hidden and output layers that are the input network for data supply. The output layer contains the values predicted by the neural network and the hidden or intermediate layer is composed of processor nodes. The selection of type and number of network inputs has a great effect on the quality of the network performance and the hidden layers have the role of organizing the performance of a neural network. Different layers in the neural network as well as neurons in the layers can have different or similar stimulus functions. Neural networks are divided into different groups in terms of structure and communication between neurons.

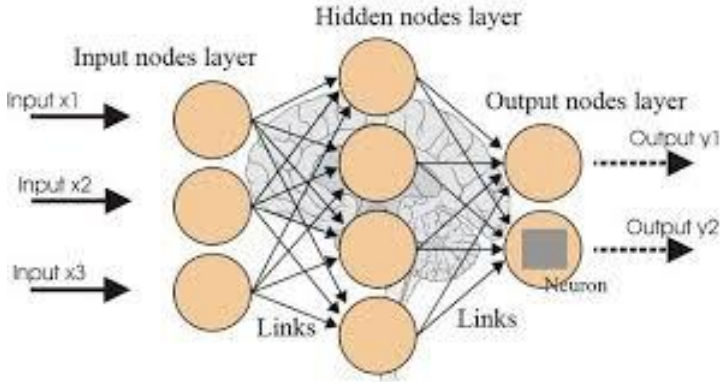


Figure 2. A general view of artificial neural network (Heykin ،1999)

2.2. Support Vector Machine (SVM)

Support vector machines act like other AI methods based on data mining algorithms. The first application of this method in water problems was proposed by (Dibike et al., 2001; Guo et al., 2008) [13, 14] to simulate runoff precipitation. Support vector machines are an efficient learning system based on constraint optimization theory that uses the principle of structural error minimization induction and leads to a general optimal solution. The way the SVM algorithm works is like most intelligent methods in training and testing, but unlike other artificial intelligence methods, instead of reducing computational errors, the operational risk of correct non-segmentation as the target function and achieves its optimal value. Figure 3 shows the structure of the backup vector machine.

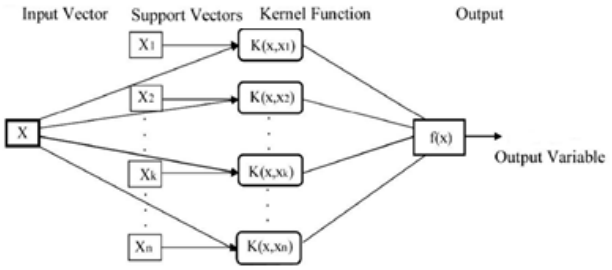


Figure 3. Structure of Support Vector Machine

In the SVM model, a function associated with dependent variable y is estimated as a function of several independent variables x. Similar to other regression problems, it is assumed that the relationship between independent and dependent variables with an algebraic function such as f(x) plus some perturbation (the allowable error ε) (relation1).

$$f(x) = W^T . \emptyset(x) + b \quad (2)$$

$$y = f(x) + noise \quad (3)$$

If W is the vector of coefficients and b constant of the attributes of the regression function and ∅ is the kernel function, then the goal is to find the functional form for f(x). This is achieved by calibration of the SVM model by a set of samples (calibration set). This process involves sequential optimization of the error function. Depending on the definition of this error function, two types of SVM model are defined:

In this study, due to its extensive application in regression studies, the regression model ε-SVM has been used to predict the discharge coefficient of a labyrinth weir with a semicircular crest. Support vector machines change the dimension of the problem through Cornell functions to solve nonlinear problems. The choice of kernel for SVM depends on the volume of training data and feature vector dimensions. In other words, according to these parameters [15], Cornley function should be selected that has the ability to train for the inputs of the problem. In this study, radial base kernel (RBF) has been used (relational 3):

$$K(x_i,x_j) = \exp\left(-\|x - x_i\|^2/\sigma^2\right) \quad (4)$$

In this research, intelligent models of artificial neural networks (ANNs) and support vector machines (SVM) models have been used to estimate the value of weir coefficient of a labyrinth with a semicircular crest (CD) using four dimensionless parameters H_t/P, L/W, W/P, and a. In the models used, four dimensionless parameters Ht/P, L/W, W/P, and a were introduced as inputs and the dimensionless parameter of C_D as output. In the models used, 75% of all available data were used for training and 25% for the test period.

2.3. Accuracy Assessment Criteria

Three statistical indices have been used to evaluate the ability and accuracy of performance of artificialneural network (ANN) and SVM models in estimating the discharge coefficient. Evaluation criteria for estimating the parameter of discharge coefficient, including correlation coefficient between observational and computational values, root mean square error (RMSE) Linear correlation between predicted and observed values (DC) are calculatedfrom 4, 5 and 6 respectively. A better model would be that R and DC have close to one and the root mean squares close to zero [16].

$$R=\frac{\sum_{i=1}^{n}(O_i-\bar{O})(P_i-\bar{P})}{\sqrt{\sum_{i=1}^{n}(O_i-\bar{O})^2\sum_{i=1}^{n}(P_i-\bar{P})^2}} \quad (5)$$

$$RMSE = \sqrt{\frac{\sum_{i=1}^{n}(P_i-O_i)^2}{n}} \quad (6)$$

$$DC = 1-\frac{\sum_{i=1}^{n}(P_i-O_i)^2}{\sum_{i=1}^{n}(P_i-\bar{P})^2} \quad (7)$$

In these relationships, the values obtained from the O_iP_i observational values (extracted from the laboratory), the values obtained from the predictive model method, the mean values obtained from the observational $\overline{OP}$value, the mean values of the predictive models' method and n is the amount of data.

3. Results and Discussion

Discharge coefficient of the labyrinth weir with a semicircular crest was performed through the results of ANN and SVM models. In this study, the laboratory data of Crookston and Tullis (2013) were used to evaluate and compare the results of the models.

Dimensionless parameters of H_T/P, L/W, W/P, and a as inputs and C_D parameters as outputs were introduced in the models used.

In Table 1, the statistical parameters of the data set for the training period and the test are shown.

Table 1. Parameter range for input and output data in the test and training course Parameters

	a	**L/W**	**W/P**	**Ht/P**	**C_D**
At least	6	1	2.008	0.023	0.199
Maximum	90	7.607	4.015	0.8	0.81
Average	22.36	3.92	2.21	0.34	0.524
Coefficient of Change	1.09	0.5	0.27	0.151	0.252
Deviation Criteria	24.42	1.98	0.612	0.23	0.132

To model the discharge coefficient, neural network has 4 neurons in the input layer (A, HT/P, L/W, W/P) and one neuron in the output layer (discharge coefficient). The high correlation coefficient between observed and estimated values in training and test data for the estimated parameters indicates the high capability of the designed neural network to estimate the discharge coefficient of labyrinth weirs with semicircular crests.

Table 2. Simulation results of a semicircular crested weir flow coefficient using neural network model

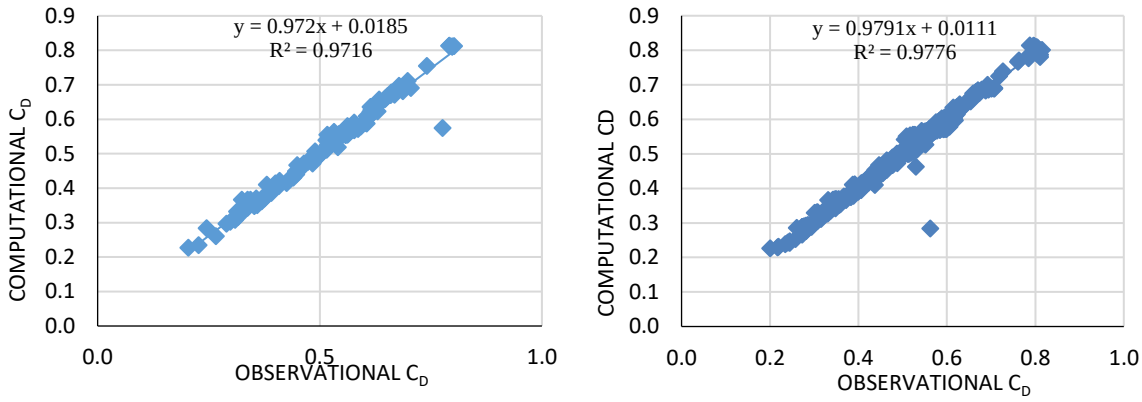
Parameter Name	Neural Network Models	Number of hidden layers	Number of neurons.
C_d	ANN	4	1-4

In order to evaluate the efficiency of the method used to estimate the discharge coefficient in labyrinth weirs with semicircular crests, Table 3 is presented.

Table 3. Accuracy of Estimation of Artificial Neural Network Model in Estimation of Discharge Coefficient

	Training			Test		
Model	RMSE	DC	R	RMSE	DC	R
ANN	0.023	0.978	0.988	0.019	0.971	0.985

In Figure 4, the scattering of observational-computational values of training stage and test of artificial neural network model are shown. According to Figure 4, it is observed that most of the points are located on or near the semi-structure line, which shows the acceptability of both models in estimating the value (C_D) but artificial neural network model. The results are very close to the observed values and therefore have a high accuracy in estimating the desired parameter (C_D) value.



A. Test **B. Training**

Figure 4. Scatter Graph of Observational-Computational Value of Training and Test of Artificial Neural Network Model

In the present study, the performance of SVM in estimation of discharge coefficient of a labyrinth weir with a semicircular crest was investigated. Considering that the selection of input models in intelligent systems can affect the accuracy of the results of the analysis, it was tried to use the input of the neural network model in the input layer (a, Ht/P, L/W, W/P) and a neuron is used in the output layer (discharge coefficient) to evaluate the yield (ANN) relative to the SVM. The performance of the support vector machine was evaluated using the RBF kernel function. According to Table 4, the results showed that the RBF kernel function with R, RMSE and DC is 0.978, 0.027 and 0.956, respectively. The syntax was such that the optimum values of ε and c were obtained for the fixed value γ, then the value was changed and the optimum value was calculated by calculating statistical parameters.

Table 4. Statistical parameters of SVM model with RBF kernel function

	Training			Test		
Kernel function type	RMSE	DC	R	RMSE	DC	R
RBF	0.031	0.942	0.971	0.027	0.956	0.978

In Figures 5 and 6, the scattering of the observational-computational values of the training stage and the support vector machine test is displayed. As can be seen in Table 4, the coefficient of explanation and determination coefficient are 0.957 and 0.956 respectively and the root mean squares are 0.027 in the test stage.

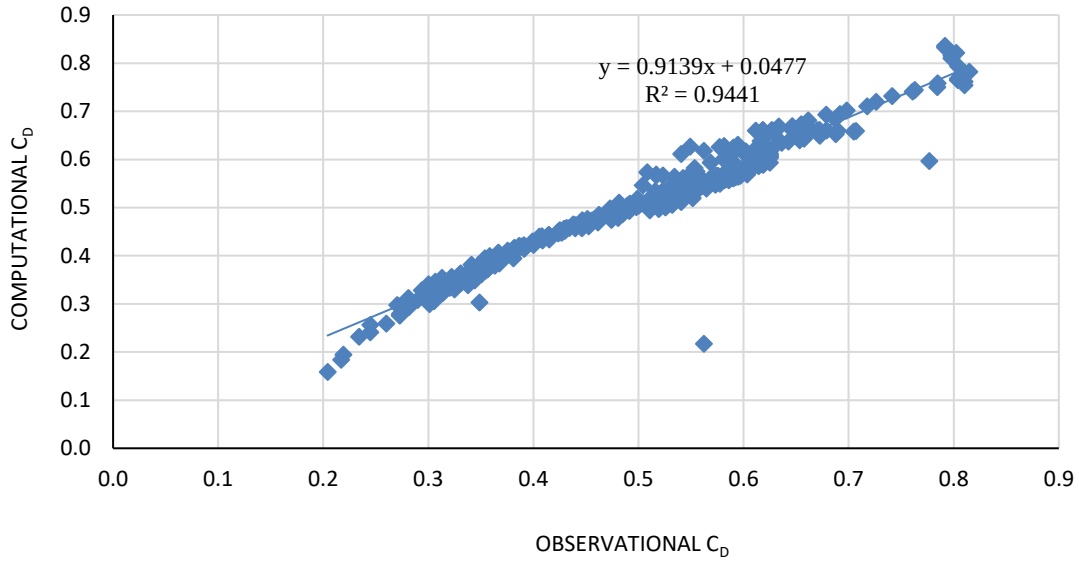


Figure 5. Scatter Graph of Observational Values - Computational SVM-RBF Training Stage

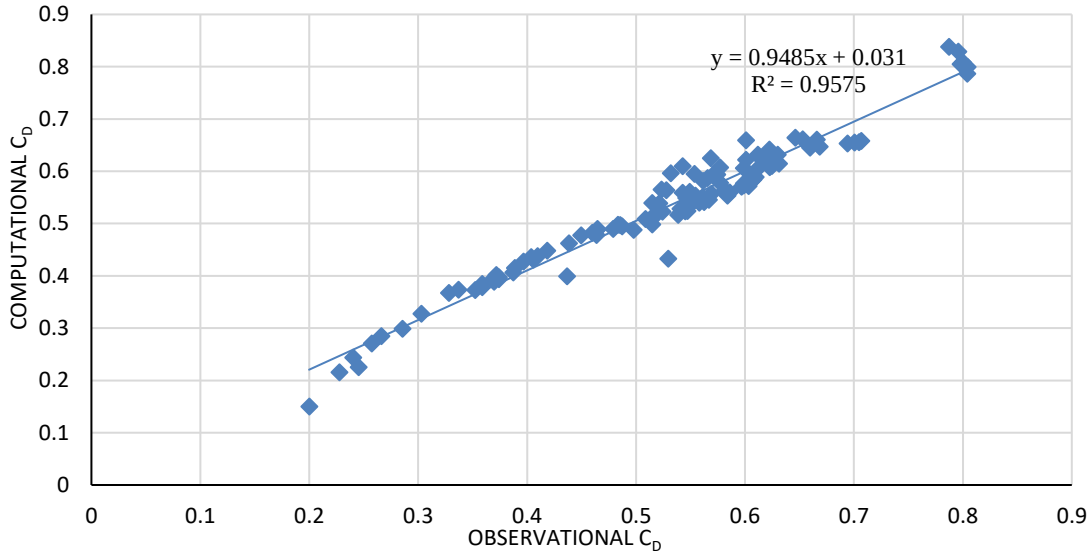


Figure 6. Scatter Graph of Observational- Computational Values of SVM-RBF Test

Statistical criteria show that ANN model has high accuracy of SVM method (Table 5).

Table 5. ANN and SVM model results for test period

Parameter / RMSE	DC		R			
	SVM	ANN	SVM	ANN	SVM	ANN
C_D	0.027	0.019	0.956	0.971	0.978	0.985

4. Conclusion

In this research, two models of artificial neural networks (ANNS) and support vector machines (SVMs) have been used to estimate the discharge coefficient of the labyrinth weir with a semicircular crest. Discharge coefficient data were obtained from the Crookston and Tullis (2013) laboratory study. Then, the estimated values (CDs) were compared with the mentioned models using the evaluation criteria. It should be noted that by random selection method of total data (454 numbers) as test and training data, with 25% and 75%, respectively, in a way that after repeating several random selections different from all available data, the data related to the conditions with the highest explicability coefficient (R) were performed. It has the lowest square mean square root (RMSE) called for the estimated process using the artificial neural network (ANN) model.

The results of this study showed that both intelligent models have better accuracy in estimating CD. However, the artificial neural network model compared to SVM machines with R, RMSE and DC was equal to 0.971, 0.019 and 0.971 for SVM and 0.957, 0.027 and 0.956 for SVM model, respectively. It is of high precision.

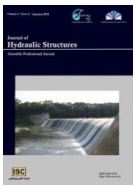
References

1. Crookston, B. and B.P. Tullis, Discharge efficiency of reservoir-application-specific labyrinth weirs. Journal of irrigation and drainage engineering, 2012. 138(6): p. 564-568.
2. Crookston, B. and B. Tullis, Hydraulic design and analysis of labyrinth weirs. I: Discharge relationships. Journal of Irrigation and Drainage Engineering, 2013. 139(5): p. 363-370.
3. Taylor, G., The performance of labyrinth weirs. 1968, University of Nottingham Nottingham, England.
4. Hay, N. and G. Taylor, Performance and design of labyrinth weirs. Journal of the Hydraulics Division, 1970. 96(11): p. 2337-2357.
5. Juma, I.A., H.H. Hussein, and M.F. Al-Sarraj, Analysis of hydraulic characteristics for hollow semi-circular weirs using artificial neural networks. Flow Measurement and Instrumentation, 2014. 38: p. 49-53.
6. Goel, A., Neural network technique for prediction of discharge coefficient and discharge for a weir. J. Indian Water Resour. Soc, 2014. 34(2): p. 25-31.
7. Kumar, S., Z. Ahmad, and T. Mansoor, A new approach to improve the discharging capacity of sharp-crested triangular plan form weirs. Flow measurement and instrumentation, 2011. 22(3): p. 175-180.
8. Roushangar, K., et al., Determining discharge coefficient of labyrinth and arced labyrinth weirs using support vector machine. Hydrology research, 2018. 49(3): p. 924-938.
9. Karami, H., et al., Predicting discharge coefficient of triangular labyrinth weir using extreme learning machine, artificial neural network and genetic programming. Neural Computing and Applications, 2018. 29: p. 983-989.
10. Haykin, S., Neural networks: a comprehensive foundation. 1998: Prentice Hall PTR.
11. Demuth, H.B. and M.H. Beale, Neural network toolbox user's guide. 1992: Mathworks, Incorporated.

12. Gupta, K., S. Kumar, and Z. Ahmad, Flow characteristics of sharp-crested W-planform weirs. International Journal of Advanced Technology & Engineering Research (IJATER), 2014. 4: p. 176-180.
13. Dibike, Y.B., et al., Model induction with support vector machines: introduction and applications. Journal of Computing in Civil Engineering, 2001. 15(3): p. 208-216.
14. Guo, B., et al., Customizing kernel functions for SVM-based hyperspectral image classification. IEEE Transactions on Image Processing, 2008. 17(4): p. 622-629.
15. Kavzoglu, T. and I. Colkesen, A kernel functions analysis for support vector machines for land cover classification. International Journal of Applied Earth Observation and Geoinformation, 2009. 11(5): p. 352-359.
16. Vapnik, V., The nature of statistical learning theory. 2013: Springer science & business media.

© 2024 by the authors. Licensee SCU, Ahvaz, Iran. This article is an open access article distributed under the terms and conditions of the Creative Commons Attribution 4.0 International (CC BY 4.0 license) (http://creativecommons.org/licenses/by/4.0/).

Journal of Hydraulic Structures
J. Hydraul. Struct., 2024;10(2):20-29
DOI: 10.22055/jhs.2024.19039



OPEN ACCESS

Laboratory investigation of the removal pattern of salinity from the base of coastal reservoirs during the first water impounding

Shaghayegh Pourbabak [1]
Hojjat Ahmadi [*1]
Amir Raouf [2]
Shuqing Yang [3]

Abstract

Coastal reservoirs, located near the shores of either seas or oceans, play a crucial role in storing fresh water for residents in coastal regions. Enclosed by concrete walls to prevent seawater intrusion, these reservoirs face challenges due to porous ground layers and direct connections to the sea. This laboratory study delves into the initial stages of optimizing coastal reservoirs, with a specific focus on desalination during the initial water intake process. The investigation highlights that salt removal primarily occurs in the ecotone bed during the initial bed scouring process. After bed leaching in this section and its extension to a specified depth, leaching initiates from beneath the main reservoir area, connecting to the ecotone scouring area. Examination of the shape and pattern of the washed area reveals that the depth of the scouring area surpasses its length along the bed. This study contributes valuable insights into the desalination potential of coastal reservoirs, particularly during the critical phase of water intake, offering a foundation for further research and development in sustainable water supply practices for coastal communities.

Keywords: Coastal Reservoirs, Leaching, Laboratory Model, Ecotone Zone.

Received: 09 November 2023; Accepted: 16 April 2024

1. Introduction

In recent years, rapid economic development has exacerbated the water scarcity problem, especially in coastal plains [1], where meeting the demand for freshwater can be challenging [2]. This situation becomes more complex with the irregular spatial and temporal distribution of freshwater resources in these areas. The flow rate (or flood) in coastal plains is usually high, but the river network has limited capacity to retain this freshwater resource [3].

[*] E-mail: hojjat.a@gmail.com (**Corresponding Author**)
[1] Department of Water Science, Faculty of Agriculture, Urmia University.
[2] Department of Earth Sciences, Utrecht University.
[3] Faculty of Engineering and Information Sciences, School of Civil, Mining and Environmental Engineering, Wollongong University, Wollongong, Australia.

CC BY

A Coastal Reservoir (CR) is a unique structure constructed at an estuary, bay, inlet, or sea (where a river joins the sea) to store a portion of excess water during floods [4]. The first coastal reservoir still in operation was built approximately 1185 years ago in China [5]. A more precise definition of coastal reservoirs could be as follows: a reservoir within a large aquatic zone stores a liquid that differs in physical, chemical, and biological characteristics from external water and is intended for a specific purpose. For example, storing fresh water in a sea reservoir implies a difference in salinity between the water inside the reservoir and the seawater [6] such as land ownership or submergence of forests [4].

For an inland reservoir, the most critical criteria are the selection of the dam site and the dam height, as these determine storage capacity, total cost, etc. Other factors such as spillways, shipping routes, and hydroelectric stations have less significance. The key considerations for CR design include the following: Firstly, the CR inlet should be ideally located to facilitate the sustainable and high-quality conveyance of water with minimal salinity in dry years. Secondly, in selecting the CR site, the overall construction cost and the confined volume of the body of water should consider the maximum flow rate and minimum cost. For an offshore CR on a flat seabed, a circular embankment with the minimum dike length is required, and the length of the dike should be determined at the minimum cost [6].

In coastal reservoirs, salt transfer processes vary throughout the different operational stages over the reservoir's lifespan. Generally, there are two major stages: in the initial stage after construction, desalination is predominant, and in the operational phase, seawater intrusion becomes a serious threat. Both desalination and the intrusion of seawater, if not properly addressed, can significantly impact the performance of coastal reservoirs [7].

Yang and Lin patented coastal reservoirs using soft dams to separate, prevent, and protect against external pollution. They concluded that the use of coastal reservoirs could significantly increase river runoff and water supply in these two areas, improving water quality. This is because the patented technology utilizes natural resources in an environmentally sustainable manner for ecosystem use [8]. Liu and colleagues examined the integrated functions of coastal reservoirs and found that water-pumping pipelines in upstream of dams or storage reservoirs could be installed simultaneously with downstream pipelines, which is much more convenient than internal reservoirs. Additionally, coastal reservoirs can be located away from environmentally sensitive areas, contributing to environmental protection. For a more rational use of water, coastal reservoirs may offer a cheaper and more sustainable option in future planning [9]. Hong and colleagues analyzed the efficiency of water quality improvement by constructing constructed wetlands (CW) to prevent pollution entry into the Hwaseong coastal reservoir. They correlated the input and output flow rates with required chemical oxygen demand (COD) and total nitrogen (TN) loads. The flow volume to CW during non-rainy days was less than the output flow, indicating that CW effectively reduces runoff volume [10].

Since the deployment of coastal reservoirs has recently gained more attention, existing works predominantly feature general recommendations and justifications for constructing these reservoirs. Consequently, details such as the salt displacement in these reservoirs from the sea and river sides have not been thoroughly investigated in past studies. Therefore, the current research focuses on laboratory experiments to examine the leaching pattern and movement of salts from the bottom and bed of the coastal reservoir after the initial water intake. The analysis will specifically address how the salts are displaced from the reservoir bottom towards the sea.

2. Materials and Methods

2.1. Laboratory model

To investigate salinity changes in the bed material of coastal reservoirs during initial water impoundment, we designed and constructed an experimental setup. The system consisted of a Plexiglas sandbox measuring 150 by 60 by 10 centimeters. This setup was partitioned into three sections: a 70-centimeter section for seawater, a 50-centimeter section for freshwater, and a 30-centimeter Ecotone reservoir serving as a barrier between saltwater and freshwater. To mimic a porous environment, we utilized standard glass beads with particle sizes ranging from 500 to 710 micrometers.

To maintain a constant discharge of freshwater and saltwater into the respective reservoirs, dedicated tanks were positioned 0.5 meters above the top of the model. Saltwater, prepared in the main ground tank to achieve the desired concentration, was pumped into the top tank. The installation of a spillway around the top tank enabled the maintenance of a constant head in the relevant tank. Similarly, freshwater was introduced into another top tank. Consequently, salt and freshwater were supplied to their designated sections within the experimental setup.

To explore the influence of water levels in individual sections of the Coastal Reservoir (CR) system on salinity variations in the base material, a series of experiments was devised. Various water levels were selected for each partition. Saltwater or freshwater was discharged from the corresponding top tank, and upon reaching a specific level, any excess water was discharged through an adjustable weir. Subsequently, the water levels in each section were stabilized at the desired levels, allowing water seepage to flow from higher-level partitions to lower ones. As a result, the seepage flow-induced changes in the salinity of the base materials over time. To mitigate seepage volume between the freshwater reservoir and seawater, and vice versa, two cutoff walls were installed beneath the boundaries of the Ecotone. The details of the constructed laboratory model are shown in Figure 1.

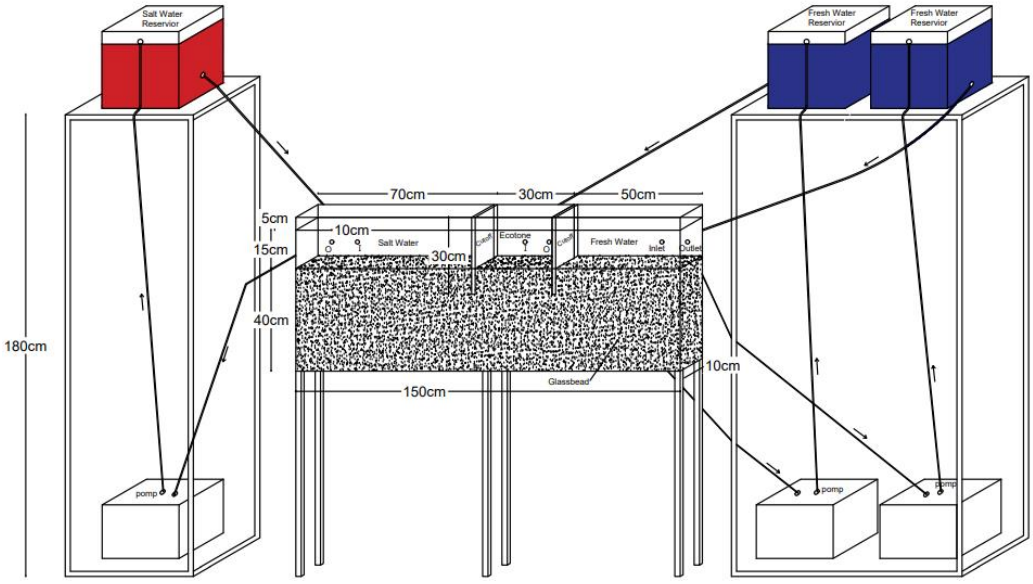


Figure 1. Geometry of the laboratory model

The glass beads were pre-washed with deionized water to eliminate any contamination thoroughly. The geotechnical parameters of the glass beads are presented in Table 1.

Table 1. physical properties of glass beads used as bedding material on the bottom of the reservoir

Physical Properties	
Hardness	6-7 Mohs
Grain Shape	round
Melting Point	730 ˚C
Specific Gravity	2.5 g/cm^3
Apparent Density	1.6 g/cm^3
Porosity	0.558
Void Ratio	35.8%
Density of Solid Grains	2.5
Saturated Humidity	0.22
Specific Gravity of Saturation	1.96
Specific Dry Weight	1.603
Specific Weight for Immersion	0.962
Dimensions	500-710 µm

After adding the required amount of glass beads into the sandboxes and homogenizing them, the environment under study was saturated with saltwater at a specific concentration. The salinity concentration used for the seawater reservoir was equivalent to the salinity of open seas, approximately 35 grams per liter. The freshwater reservoir and the ecotone reservoir were filled with tap water. Considering the salt concentration used for seawater, its density was 1.024 grams per liter. To maintain a constant water head in the air chambers, fixed overflow outlets were incorporated, and water with a constant flow rate was pumped into the lower reservoirs. This way, excess water was discharged through the overflows from the air chambers, and the water level remained constant. This technique was employed to establish a stable flow from the air tanks to different sections of the laboratory system. A yellow food dye was used to trace the seawater. Salinity measurements were taken throughout the experiment to ensure a constant salt concentration in the seawater reservoir, and changes in the density of the ecotone and coastal reservoir were recorded. A water head of 15 centimeters was considered in the coastal reservoir and ecotone reservoirs, and for the specified range of seawater, 14 centimeters were considered. Discharge valves installed at specific levels maintained a constant water head in these areas.

After adding the required amount of glass beads into the sandboxes and homogenizing them, the environment under study was saturated with saltwater at a specific concentration. The salinity concentration used for the seawater reservoir was equivalent to the salinity of open seas, approximately 35 grams per liter. The freshwater reservoir and the ecotone reservoir were filled with tap water. Considering the salt concentration used for seawater, its density was 1.024 grams per liter. To maintain a constant water head in the air chambers, fixed overflow outlets were incorporated, and water with a constant flow rate was pumped into the lower reservoirs. This way, excess water was discharged through the overflows from the air chambers, and the water level remained constant. This technique was employed to establish a stable flow from the air tanks to different sections of the laboratory system. A yellow food dye was used to trace the seawater. Salinity measurements were taken throughout the experiment to ensure a constant salt concentration in the seawater reservoir, and changes in the density of the ecotone and coastal reservoir were recorded. A water head of 15 centimeters was considered in the coastal reservoir and ecotone reservoirs, and for the specified range of seawater, 14 centimeters were considered. Discharge valves installed at specific levels maintained a constant water head in these areas.

2.2. Numerical Model

In this study, the SEEP/W and CTRAN/w a module of GeoStudio-2022 software was used for numerical simulation. SEEP/W is an advanced computational tool based on the finite element method, which is employed for modeling seepage and distribution of pore water pressure in porous media such as soil and rock. This software enables the modeling of both simple and complex problems through specialized formulations and complex algorithms. By utilizing numerical methods, SEEP/W can accurately simulate the flow of water among soil particles and analyze the physical process [11]. Based on the model properties and problem circumstances free convection solute effect, solute transfer advection-dispersion with water transfer Were selected to investigate the mass of solute transportation in the model. The method of selecting the model inputs was based on the physical properties of the glass beads selected in the laboratory model, as shown in Table 1.

The boundary conditions are determined based on laboratory conditions, and their details are provided in Table 2.

Table 2. Assumptions for the boundary conditions in the numerical model

Boundary Conditions	CR	Ecotone	Saltwater	
Category: Contaminant	0 kg/m³	0 kg/m³	35 kg/m³	Solute Concentration
Color	Green	Orange	Red	
Category: Hydraulic	0.55 m	0.55 m	0.54 m	Water Total Head
Color	Blue Navy	Sky Blue	Red	

Also, Figure 2-a shows the image of the model after applying the hydraulic head boundary condition, and Figure 2-b shows the model after applying the contaminant (salinity) condition.

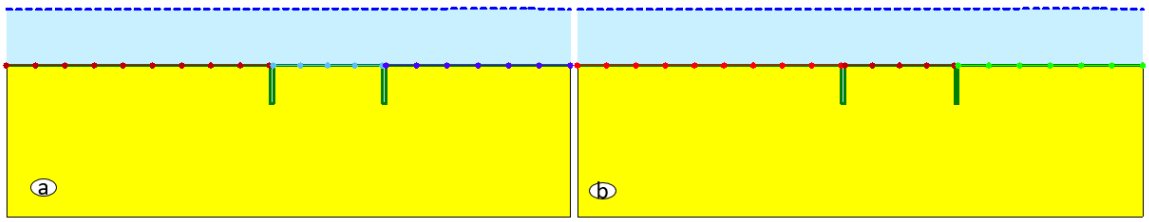


Figure 2. Apply the boundary condition: a (hydraulic BC), b (contaminant BC)

3. Results and Discussion

Freshwater and seawater are two distinct water bodies with different physical and chemical properties. However, in coastal reservoirs, with the creation of a height difference, freshwater can move from the porous bed towards the seawater. When freshwater is positioned at a higher elevation than the seawater in the sea, the movement of freshwater towards seawater occurs due to the energy difference, resulting in a gravity flow. In the current experiment, with a bed fully saturated with saltwater, the difference in water level between the freshwater reservoirs (ecotone and CR) and the seawater creates a hydraulic gradient. Since in both modeled areas for ecotone and the coastal reservoir, freshwater is positioned 1 cm higher than seawater ($h_{CR}=h_{eco}>h_{sw}$), the hydraulic pressure designed in ecotone and CR is greater than that of the seawater reservoir. The average gradient of the flow created from the freshwater reservoirs towards the seawater was calculated using Darcy's law. The gradient values for each of the reservoirs are presented in

Table 3. Accordingly, freshwater flow from the ecotone and the freshwater reservoir occurs as leakage from the bed. Due to the proximity of the ecotone area to seawater, initially, the flow occurs from this area towards seawater. As shown in Figure 3-a, bed leaching in the ecotone area has occurred due to this flow. Subsequently, the infiltrated freshwater flow from the bed of the freshwater reservoir joins the flow from the ecotone and reaches the washed area in the bed of these two sections, as shown in Figure 3-b.

Table 3. hydraulic parametric of Freshwater, Seawater, and Ecotone Reservoir

Water Level (cm)			Hydraulic Head (cm)			Hydraulic Gradient	
Coastal Reservoir	Ecotone	Seawater Reservoir	Coastal Reservoir	Ecotone	Seawater Reservoir	Seawater Reservoir/ Coastal Reservoir	Seawater Reservoir/ Ecotone
15	15	14	15	15	15.174	59	25.33

After completely leaching the ecotone bed from seawater, the downward movement of the infiltrated flow from the CR zone is stopped. After passing around the wall of the water barrier, it enters the seawater reservoir from the nearest distance, as shown in Figure 3-c. Meanwhile, the infiltrated flow from the bed of the freshwater reservoir continues to join the inflow from the ecotone, increasing the intensity of the leakage flow from freshwater to seawater. Due to the limited cross-sectional flow area behind the second water barrier (near the seawater reservoir), the leakage flow is diverted downwards and causes the expansion of the washed area, as shown in Figure 3-d. Eventually, after sufficient space for the passage of the leakage flow is created behind the second water barrier, the downward movement of the infiltrated freshwater from the freshwater reservoir and ecotone is stopped. With the passage of time, no significant change in the washed area of the bed is observed, as shown in Figure 3-e.

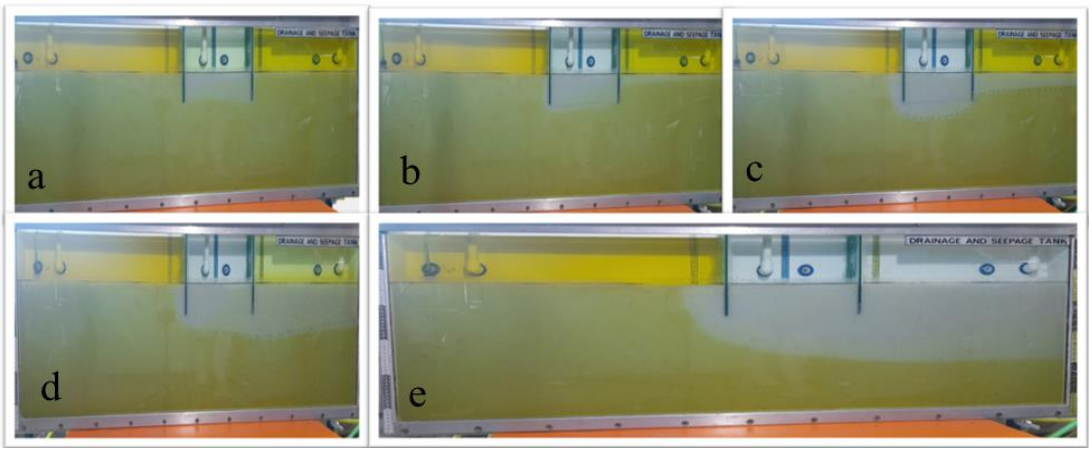


Figure 3. Different stages of movement of fresh water to salt water, respectively from a to e

In this way, the depth of the washed area is limited to 23 centimeters, which is about 1.5 times the height of the water inside the reservoir. It is evident that the depth of the washed area depends on various factors, including the height difference, water temperature, and water density, and it is recommended to investigate these factors as parametric parameters. Moreover,

the results presented in Figure 3 and the comparison of images of the washed area and its expansion show that the depth of the washed area under the freshwater reservoir and the ecotone reservoir is significantly greater than the washed area behind the second water barrier. The depth ratio of the washed area under the freshwater reservoir and the ecotone reservoir to the length of the washed area behind the second water barrier in the modeled system is 2.5.

3.1. Simulation Results in SEEP/W Model

To assess the accuracy and precision of the laboratory experiment, the experiment conditions were defined in the Geo-Studio2022 software, specifically in the Seep/w module of this software. According to the laboratory conditions and to calibrate the freshwater head for the region, a constant head of 15 cm and a seawater head at an elevation of 14 cm were set. The results of this modeling are presented in Figure 4.

Based on the vectors of saltwater (Green vectors that represent solute mass flux) and freshwater (black vectors that represent water flux) flow extracted from the software image, it can be concluded that the presence of two cut-off walls (forming the Ecotone area) and the 1cm difference in head between saltwater and freshwater prevent saltwater leakage into the Ecotone and CR reservoirs. The vectors of saltwater flow indicate that saltwater did not pass through the cut-off walls and even freshwater entered the saltwater area during the final hours of the experiment and ultimately ceased to advance at the boundary where the energy of saltwater and freshwater is equal.

Observations showed that the vectors of saltwater in the CR region changed direction over time from a predominantly vertical state to a relatively horizontal one, moving towards the saltwater area. Additionally, the mentioned vectors in the saltwater region indicated that the saltwater mass in the modeled area is circulating in the sea and the intrusion has ceased at the beginning of it.

The reason for not completely freshwater intrusion in the area intended for the sea near the first cut-off wall is the diffusion phenomenon and the low speed of the flow, which means that part of the layer always remains salty.

The designed model in the laboratory exhibits good agreement with the numerical model. As observed, the depth of the saltwater intrusion after the cessation of freshwater intrusion in the SEEP/W model was also 23 cm, similar to the laboratory model.

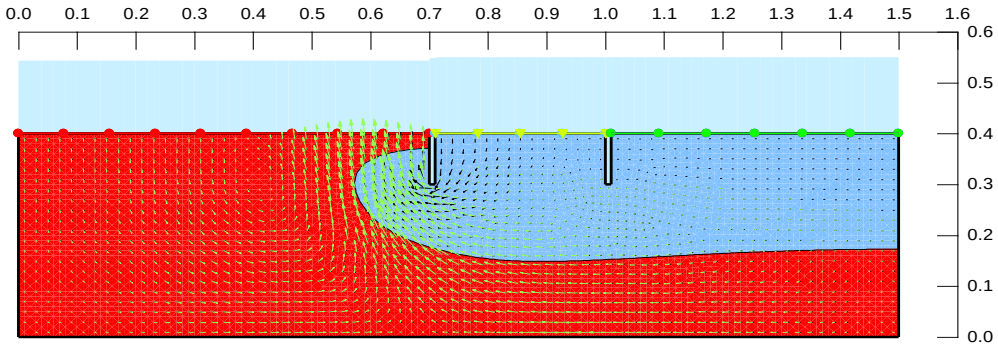


Figure 4. The progress of freshwater and solute mass flux vectors at the end of the experiment

In Figure 5 from a to e, the process of washing the saline bed by freshwater intrusion from the inlets of the CR and the ecotone zone is shown during the time. The relatively complete agreement of the numerical model with the laboratory model (figure 3) can be seen.

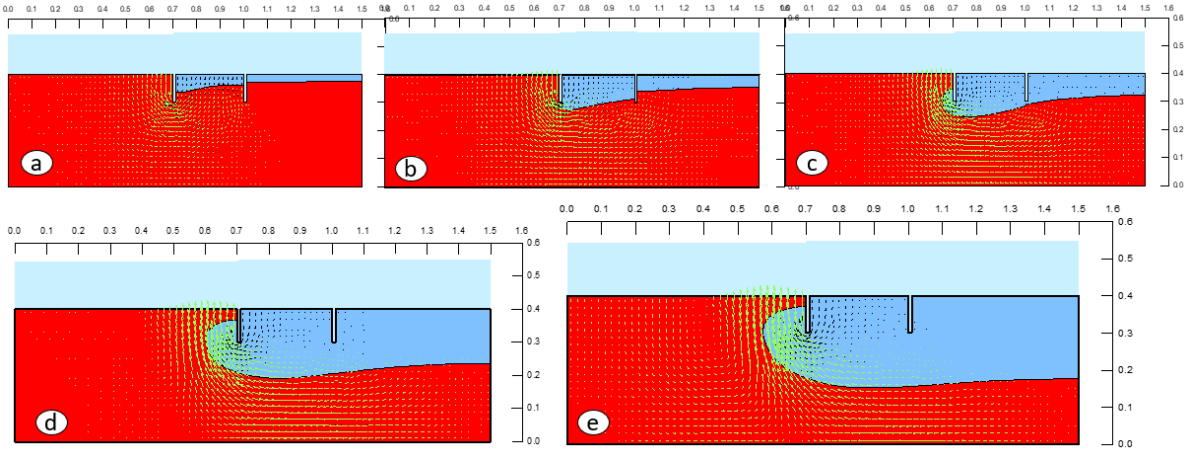


Figure 5. Different stages of movement of fresh water to salt water in GeoStudio, respectively from a to e

Also, according to Figure 6, the amount of mass flux in terms of time, which is extracted from the software based on meshing, can be seen in the first cut-off wall, which is designed on the saltwater side of the sea, the amount of mass flux of salt with time Dropped. This indicates the entry and intrusion of freshwater from the side of the coastal reservoir and the ecotone area.

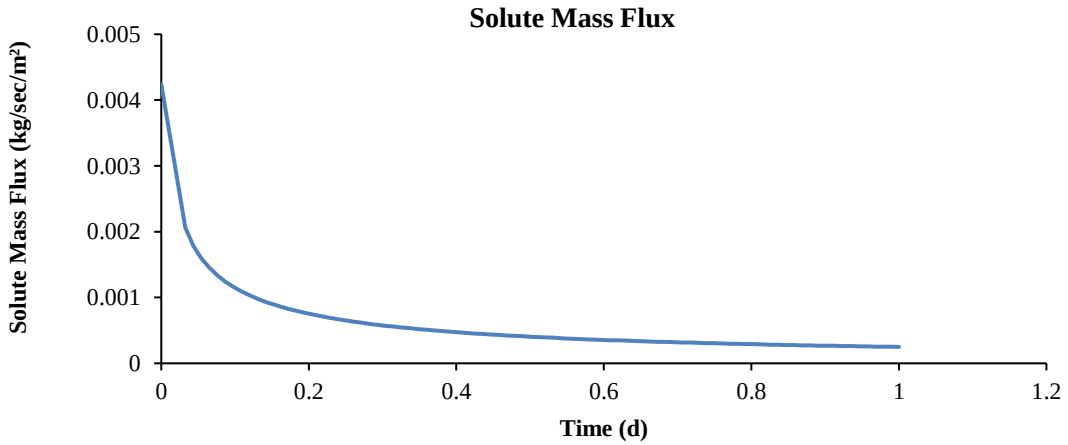


Figure 6. The amount of mass flux in terms of time at the boundary of the first cut-off wall

Based on the obtained results, the graph related to the second cut-off wall, which is designed on the side of the coastal reservoir, was also drawn, figure 7. In this graph, it was observed that the salt in the water was completely washed away. This result indicates the complete desalination of water in the coastal reservoir and ecotone zone. According to the complete agreement of the graphs obtained from the observations in the laboratory, it can be concluded that the designed cut-off walls have worked well and have been able to separate fresh water from salt water.

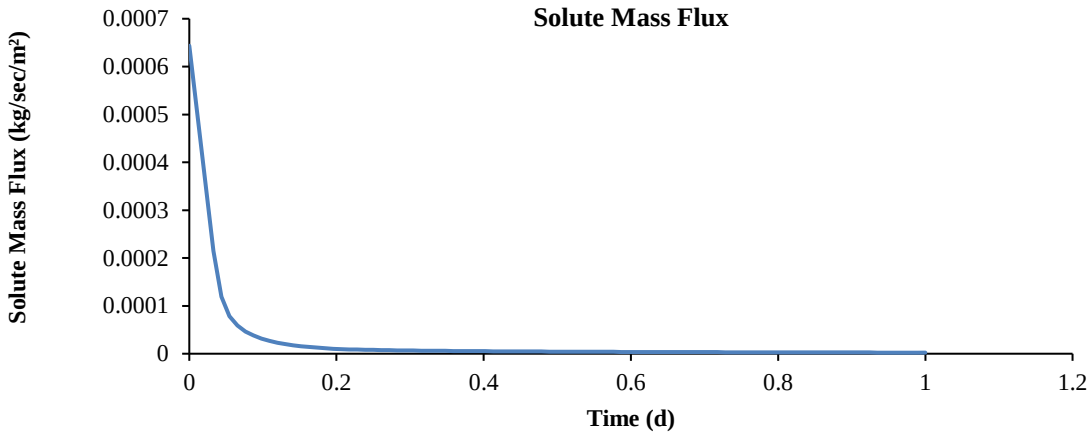


Figure 7. The amount of mass flux in terms of time at the border of the second cut-off wall

4. Conclusion

In the present study, the washing pattern of the bed of a coastal reservoir was investigated using a laboratory model during the initial water intake. In the examined model, the level of freshwater and the ecotone reservoir were set equal to and higher than the level of the seawater surface. The results of this investigation showed that due to the higher level of the freshwater surface in the respective reservoirs and, consequently, the movement of infiltrated water from the freshwater towards the seawater reservoir occurs. Notably, the bed washing of the salt crystals initially takes place from the ecotone and its bed, and then the washed area expands and develops under the seawater reservoir.

In this current investigation, the study also derived general equations for calculating energy loss under threshold conditions. The accuracy of these equations was rigorously assessed using various statistical indices, including Relative Error, Root Mean Square Error, and Kling Gupta Efficiency. The results affirm the high precision of the presented equation, endorsing its utility in predicting relative energy loss with confidence.

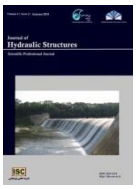
References

1. Herrera-León, Sebastián et al. 2018. “Optimization Approach to Designing Water Supply Systems in Non-Coastal Areas Suffering from Water Scarcity.” Water Resources Management 32(7): 2457–73.
2. Phan, Thuc D et al. 2018. “Assessment of the Vulnerability of a Coastal Freshwater System to Climatic and Non-Climatic Changes: A System Dynamics Approach.” Journal of Cleaner Production 183: 940–55. https://www.sciencedirect.com/science/article/pii/S0959652618304888.
3. Xiao-ping, Ge. 2012. “Layout Optimization of Freshwater-Storage Projects in Coastal Reclamation Areas.” Journal of Economics of Water Resources. https://api.semanticscholar.org/CorpusID:132646608.
4. Sitharam, T.G. 2017. “Efficacy of Coastal Reservoirs to Address India’s Water Shortage by Impounding Excess River Flood Waters near the Coast.” Journal of Sustainable Urbanization, Planning and Progress 2(2): 49–54.

5. YANG, SHU-QING. 2019. “Historical Review of Existing Coastal Reservoirs and Its Applications.” 38th IAHR World Congress - “Water: Connecting the World” 38: 3957–73.
6. Sitharam, T. G. et al. 2020. Sustainable Water Resource Development Using Coastal Reservoirs Sustainable Water Resource Development Using Coastal Reservoirs.
7. Jin, Guangqiu et al. 2019. “Desalinization and Salinization: A Review of Major Challenges for Coastal Reservoirs.” Journal of Coastal Research 35(3): 664–72.
8. Yang, Shu-Qing, and Pengzhi Lin. 2012. “Coastal Reservoir by Soft-Dam and Its Possible Applications.” Recent Patents on Engineering 5(1): 45–56.
9. Liu, Jianli, Shuqing Yang, and Changbo Jiang. 2013. “Coastal Reservoirs Strategy for Water Resource Development—A Review of Future Trend.” Journal of Water Resource and Protection 05(03): 336–42.
10. Hong, Jungsun, Marla C. Maniquiz-Redillas, Jong-Hwa Ham, and Lee-Hyung Kim. 2016. “Analysis of Water Quality Improvement Efficiency Using Constructed Wetland in a Coastal Reservoir.” Journal of Wetlands Research 18(3): 292–300.
11. Arshad, I. and Babar, M., 2014. Comparison of SEEP/W simulations with field observations for seepage analysis through an earthen dam (case study: Hub DamPakistan). International Journal of Research, 1(7): 57-70

© 2024 by the authors. Licensee SCU, Ahvaz, Iran. This article is an open access article distributed under the terms and conditions of the Creative Commons Attribution 4.0 International (CC BY 4.0 license) (http://creativecommons.org/licenses/by/4.0/).

Journal of Hydraulic Structures
J. Hydraul. Struct., 2024;10(2):30-45
DOI: 10.22055/jhs.2024.19040



OPEN ACCESS

Modeling of discharge Coefficient of nonlinear weirs with QNET and SVM methods

Mahdi Majedi Asl [*1]
Tohid Omidpour Alavian [1]
Yousef Seyfari [1]
Mehdi Kouhdaragh [2]

Abstract

In this study, we investigate the discharge coefficient prediction of arched labyrinth weirs with a cycle angle of 6 degrees, employing 243 data series. Labyrinth weirs, aside from their economic advantages, exhibit superior flow-passing capabilities compared to linear weirs. Notably, increasing the length of the crest within a specified width enhances discharge efficiency with less upstream height. Machine learning algorithms, namely QNET and SVM, play a pivotal role due to their proficiency in uncovering intricate relationships between independent and dependent parameters, leading to significant time and cost savings. Our results using QNET and SVM indicate that the combination of (Cd, $\frac{H_T}{p}$, θ, $\frac{L_C}{W}$) yields optimal accuracy, with QNET achieving (R^2=0.9850), (RMSE=0.0259), and (DC=0.9892) in the training phase, and (R^2=0.9824), (RMSE=0.0292), and (DC=0.9788) in the test phase. For SVM, the training phase results are (R^2=0.9889), (RMSE=0.0189), and (DC=0.9870), and in the test phase (R^2=0.9881), (RMSE=0.0199), and (DC=0.9853). Sensitivity analysis shows the significant role of the total water load ratio parameter ($\frac{H_T}{p}$) in determining the discharge coefficient of arched labyrinth weirs. This research contributes to the understanding of non-linear arched weir discharge predictions and highlights the efficacy of QNET and SVM algorithms in this domain.

Keywords: Sensitivity Analysis, Non-Linear Weirs, Evaluation Indicators, Discharge Coefficient.

Received: 09 November 2023; Accepted: 16 April 2024

[*] E-mail: mehdi.majedi@gmail.com (**Corresponding Author**)
[1] Department of Civil Engineering, Faculty of Engineering, University of Maragheh, Maragheh, Iran.
[2] Department of Civil Engineering, Engineering Faculty, Malekan Branch, Malekan Islamic Azad University, Malekan, Iran.

CC BY

1. Introduction

One of the important topics during the development of civilization is the management and transfer of human water. Various hydraulic structures have been designed and built to meet the needs. One of the common structures in many dams and water transfer channels are weirs, which are used for the purpose of draining, measuring and controlling the water level. Given the potential for maximum rainfall and the constant need for dam safety, most of the existing weirs are small and correction. The volume of flow passing through the weir depends on the length and shape of the weir crest. Numerous studies have been conducted on the impact of hydraulic and geometrical parameters on the flow discharge coefficient and the amount of flow passing through the weirs. An effective approach to increase the length of a flow weir within a specific width is the use of weirs with a non-linear plan, such as triangular, trapezoidal, circular, parabolic, etc., commonly referred to as multi-faceted, labyrinth or zigzag weirs These multi-faceted weirs are typically constructed in a single cycle or through multiple cycles. The emergence of labyrinth weirs in recent years has enhanced weir performanceby replacing linear weirs with non-linear labyrinth weirs. One of the main characteristics of labyrinth weirs is their capacity to increase the overall length within a channel with limited width. Arched labyrinth weirs show their highest level of efficiency in the damn reservoirs. According to the hydraulic performance and geometric diversity, arched labyrinth weirs are built as a water head control structure, energy consumption, flow aeration and flow measurement in the direction of channel, river, lake, and reservoirs. A labyrinth weir is a folded linear weir in plan. Increasing the crest length in a limited width of the channel is possible and can be designed for labyrinth weirs. A labyrinth weir can pass more flow at relatively low heads compared to linear weirs with the same channel width. A labyrinth weir has a crest length that extends beyond the width of the channel, which is a developed characteristic compared to linear weirs located in the same channel. In other words, for the given discharge, the head for the labyrinth weir is less than the linear weir. This condition is widely used when the maximum height of the flow is limited. The aeration efficiency of the labyrinth weirs is better than the linear weirs of the same length and this increasement in efficiency is effective in reducing the higher discharges. Figure 1 illustrates the plan of different labyrinth weirs.

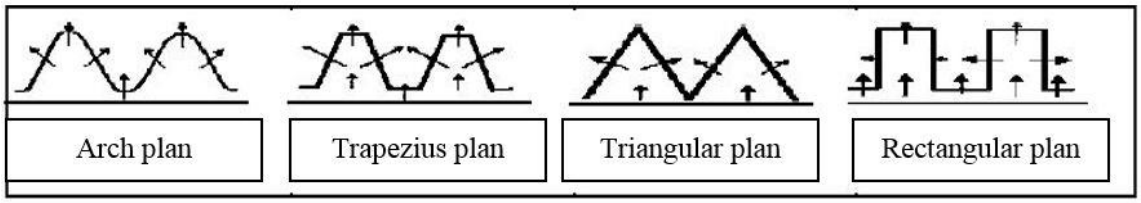


Figure 1: Plan of different types of labyrinth weirs

The hydraulics of labyrinth weirs was investigated for the first time by Gentilini in 1940 [1]. Kozak and Swab in 1961 examined eleven labyrinth weirs with different trapezoidal plans. They came to the conclusion that the volume of flow passing through the labyrinth weirs for a specific head in the upstream is significantly more than the linear weirs. Also, they came to the conclusion that for an equivalent length, the number of small cycles is more efficient than large cycles [2]. Tison and Fransen (1963) researched labyrinth weirs [3]. Taylor (1968) also studied the performance of triangular, trapezoidal and rectangular weirs with sharp edges and different number of cycles [4]. Also, Hay and Taylor (1970) were the first people who conducted the most comprehensive study on triangular and trapezoidal labyrinth weirs (with a sharp edge crest

shape) and achieved practical results in this field. They used the ratio of labyrinth weirs flow to linear weirs flow to show the performance of labyrinth weirs. In the design curves presented by them, the hydrostatic height of the flow was included as an effective load on the weir [5]. Darvas (1971) presented the results of his research based on the physical models of Verona and Avon dams, this researcher also presented a curve handle for the design of trapezoidal weirs with a quarter circle crest and an experimental relationship [6]. Indlekofer and Rouve (1975) studied the flow interference zone at the vertices of sharp edge triangular weirs and defined a length for the flow interference zones [7]. Cassidy et al. (1985) showed that for high heads, the discharge coefficient of labyrinth weirs is significantly lower than other weirs [8]. Tacail et al. (1990) showed that in similar widths, two-cycle labyrinth weirs perform better than three-cycle labyrinth weirs [9]. Tullis et al. (1995) worked trapezoidal labyrinth weirs with 4 cycles and 5 different crest shapes and they found that the capacity of trapezoidal labyrinth weir is a function of total hydraulic load, medical crest length and coefficient the water is passable. The water passage coefficient is a function of the height of the weir, the total hydraulic load, the thickness of the weir wall, the shape of the crest, the shape of the top, and the angle of the lateral walls of the weir. By examining the effect of these parameters on the performance of labyrinth weirs, they presented new diagrams and found that the throughput efficiency of labyrinth weirs increases three to four times compared to linear weirs for the same upstream load [10]. Wormleaton and Soufiani (1998) stated that the aeration coefficient of triangular labyrinth weirs compared to linear weirs depends on the apex angle and the length of the weirs crest [11]. Wormleaton and Tsang (2000) conducted their studies on the aeration of labyrinth weirs and concluded that the rectangular labyrinth weirs have a higher efficiency for flow aeration compared to the triangular shape and compared to the linear weirs. These researchers also announced that with the increase in discharge, the superiority of the rectangular shape over the triangular shape increases, which is due to the increase in the interference of the falling layers of the flow in the triangular weirs [12]. Ghodsian (2007) conducted laboratory studies on a triangular labyrinth weir with different crest shapes and first extracted the relevant parameters in a dimensionless way by dimensional analysis, and then with the laboratory data, a regular and consistent relationship for the discharge coefficient and introduced Head-Debbie [13]. According to the findings of the experimental research conducted by Zerihun and Fenton (2007) and Kabiri and Samani et al. found [14] and [15]. Carollo et al. (2012) worked on a dimensionless head-discharge relationship for triangular labyrinth weirs with a change in the flow direction of the vertices of the triangles [16]. Crookston et al. (2013) analyzed the analysis and optimal design of labyrinth weirs for flow aeration, estimation of the head-discharge relation, stabilization of the water blade on the weirs, and by cutting parts of the wall and nose of the weirs, as well as by creating appendages. Crookston et al. (2013) analyzed the analysis and optimal design of labyrinth weirs for aeration flow, estimation of the head-discharge relationship, stabilization on the weir blade, and by cutting parts of the wall and nose of the weir, as well as by creating appendages. On the walls and nose of weirs, they improve the main factors [17]. The research results of Dabling (2014) showed that with the increase of the $(\frac{H_o}{P})$ ratio in modified and unmodified weirs, the absorption ratio increases [18]. The results of the experimental research carried out by Seo et al. (2016) showed that the flow rate through a labyrinth weir is about 70% higher than the flow rate through a direct sharp edge weirs under free flow conditions. They stated that with the increase of the degree of absorption of the weirs, the permeability efficiency of the weirs decreases, and its value is proportional to the ratio $(\frac{h_d}{h^*})$ [19]. Christiansen (2015) while investigating the inflow field to labyrinth weirs, investigated the effect of the number of

cycles on the performance of this type of weirs and concluded that with the increase in the number of cycles, the water passage coefficient decreases [20]. In recent years, following experimental and laboratory studies, a lot of research has been done to improve and advance experimental methods for calculating the discharge coefficient, choosing the optimal geometry and efficiency of labyrinth weirs, among which we can soft computing methods that are data oriented. Cimen (2008), Kakai Lafdani et al. (2012) used the SVM model to predict the monthly volume of suspended sediment in the Dorij River located in Ilam province [21] and [22]. Govan et al. (2009) and Azmatullah et al. (2010) and Goyal et al. (2011) using the method (SVM, GEP and ANN and artificial neural network) scouring around hydraulic structures and the scouring depth of the bridge base in a The laboratory model predicted and showed that the above methods provide more accurate predictions than experimental methods [23], [24] and [25]. Azhdari Moghadam et al. (2009) optimized the geometry of the triangular labyrinth weirs using neural fuzzy model and genetic algorithm (case study of Hyrum Dam in the state of Utah, USA) and compared the results of this method with the available values from The weight of concrete used in the current situation shows a 12.35 percent reduction in weirs costs, which indicates the better results of this method [26]. Abbaspour and Arvanaghi (2011) used GEP model to estimate flow rate on triangular-rectangular composite weirs and investigated and compared the effect of geometric and hydraulic parameters on flow rate. The results showed that there is a good match between the observed and predicted values of the genetic programming model [27]. The use of artificial intelligence models such as GEP, SVM, ANFIS, etc. have found a lot of use in the simulation of complex hydraulic, hydrological and water resources phenomena in recent years, Farrokhy et al [28] (2009). The use of soft computing methods such as support vector machine can be considered as an alternative method for empirical equations and models, and in recent decades, they have brought about a huge evolution in engineering problems. These methods have shown good ability in modeling and predicting complex phenomena and optimizing engineering problems. The main reason for using smart models is the cost estimation and time-consuming normal methods compared to smart models. Karami et al. (2016) used artificial intelligence algorithms to accurately predict the water flow coefficient of labyrinth weirs [29]. Roushangar et al. (2016) predicted the flow rate coefficient for lateral weirs by using intelligent learnable algorithms [30]. Parsaie, Haghiabi et al. (2017) used neural network and adaptive neural fuzzy inference system to estimate the permeability coefficient of oblique lateral weirs. They used the SVM algorithm to model the discharge coefficient of a sharp edge weirs with a W-shaped plan [31]. Majedi and Fuladi Panah (2017) have recommended the use of SVM algorithm for use in simulations where the laboratory variable is a function of several independent variables [32]. Majedi et al. (2018) investigated the use of evolutionary systems in determining the discharge coefficient of triangular labyrinth weirs and stated that the support vector machine method has a very good performance in predicting the discharge coefficient of sharp edge labyrinth weirs and can He used this method in similar cases [33]. Roushangar et al. (2018) determined the discharge coefficient of labyrinth weirs and labyrinth arch by the support vector regression method and by comparing the experimental and predicted data, they found the SVM model as the appropriate model for determining the discharge coefficient. Labyrinth weirs recommended [34]. Mehri et al. (2018) used the SVM model to estimate the flow coefficient of piano key weirs in irrigation and drainage networks. The result of their research confirmed the appropriate flexibility of the SVM model compared to nonlinear regression and the high accuracy of the SVM model [35]. In the research conducted by Parsaie et al. (2019), the use of intelligent mathematical models GEP, GMDH and MARS modeled the discharge coefficient of non-linear weirs [36]. Kumar et al. (2020) simulated the flow coefficient of piano key weirs in a

laboratory and machine learning algorithm, the result of their research indicated the very appropriate accuracy of machine learning algorithms [37]. Fuladi Panah et al. (2020) investigated the use of intelligent algorithms for modeling the discharge-Eschol relationship in the conditions of congestive and linear weirs [38]. Majedi et al. (2021) conducted a study using data mining methods to improve the prediction of the discharge coefficient in the weirs of piano keys and labyrinth [39]. Roushangar et al. (2021) in laboratory studies as well as modeling based on artificial intelligence investigated the discharge coefficient of converging peak weirs [40]. Omidpour Alavian et al modeled and evaluated the discharge coefficient of arched labyrinth weirs [41]. Omidpour Alavian et al. compared the hydraulic efficiency of labyrinth weirs with quarter-circle and semi-circle crest shapes [42]. Majedi et al investigated the hydraulic efficiency of labyrinth weirs with quarter-circle and semi-circle crest shape [43]. Majedi et al. compared the hydraulic efficiency of labyrinth weirs with artificial intelligence methods [44]. Labyrinth weirs are among the weirs that have been researched from various hydraulic and geometrical aspects. The review of previous sources and researches shows that there is less study and research regarding the comparison of laboratory results and the prediction of the flow rate coefficient of the arched labyrinth weir using QNET and SVM smart algorithms combined with the application of the effect Various hydraulic and geometrical parameters have been determined, which is the novel and innovative aspect of the current research.

In this regard, with the help of laboratory results data and using QNET and SVM machine learning algorithms, the effect of geometric and hydraulic parameters including total water load ratio ($\frac{H_T}{p}$), magnification factor ($\frac{L_C}{W}$), cycle wall angle (α), the angle of the arc cycle (θ) has been investigated on the discharge coefficient of the arched concourse overflow. The purpose of this research is to compare the discharge coefficient of the arched labyrinth weir (Cd) obtained in Crookston's (2010) research with those derived from machine learning analyses, QNET and SVM, applied to the arched labyrinth weirs.

2. Materials and Methods

The aim of this research is to compare laboratory data results with those obtained from machine learning algorithms, namely QNET and SVM, for determining the flow rate coefficient in arched labyrinth weirs. Additionally, the study aims to accurately evaluate machine learning algorithms using statistical parameters and compare their outcomes with the laboratory data results. In this article utilizes the research data of Brian Mark Crookston's work conducted in 2010 at the Utah Water Research Laboratory. An illustration of the rectangular channel and the test facility of the tank is shown in Figure 2. Crookston's research employed two facilities for physical modeling: a rectangular flume designed for channelization applications, and a large head box intended for reservoir applications, as depicted in Figure 2.

2.1. Rectangular channel Installations

The rectangular laboratory channel with specifications (1.2 m wide, 14.6 m long and 1 m deep) consists of a steel frame and acrylic glass for the walls and floor. The slope of the channel is adjusted by four large mechanical jacks. For this study, the longitudinal slope of the channel bed, S_{bed} was set to zero. After installation, the platform was adjusted to the horizontal level (±0.4 mm). A 2.44-meter-long ramp, with a slope of 7 degrees, was installed upstream of the platform to ensure a smooth transition between the floor of the flume and the platform. Two supply lines deliver water to a steel head box that has a baffle structure to maintain smooth flows and uniform approach conditions to the channel.



Figure 2: Pictures of the channel and reservoir and laboratory facilities. (Crookston [2], 2010)

The one-dimensional equation of the flow on the labyrinth weirs is expressed as a function of the total water load (H_T) in meters, the length of the weir crest (L) in meters and the dimensionless weir flow coefficient (Cd), obtained from equation (1) in the work of Henderson [45] (1966). The effective parameters on the discharge coefficient in the weirs of the labyrinth can be expressed in the form of functional relationship, as given in equation (2).

$$Q = \frac{2}{3} Cd\sqrt{2g}\, L H_T^{\frac{3}{2}} \quad (1)$$

$$Cd = f\,(B, L, H_T, Hd, P, R, CR, Na, N) \quad (2)$$

In the equation (2), B is width of the channel where the weirs is installed; L is length of weirs crest; H_T is the head of the total flow upstream of the weirs, which is equal to ($\frac{h+v^2}{2g}$); Hd is head of the entire flow downstream of the weirs; P is weirs height; R is the radius of curvature of semicircular cycles; CR is the parameter representing the shape of the weir's crest, which can be edged, smooth, quarter circle with small to large rays, semicircular and pointed; Na represents the shape of the flow blade in the weirs of the labyrinth, which can be free fall, mixed fall, aerated, incomplete or complete aeration, and N is the number of cycles. In this research parameters are (Cd, $\frac{H_T}{p}$, α, Θ, $\frac{L_C}{W}$) and the number of data is 243. to the investigation of the changes in the discharge coefficient of the labyrinth weir has been done using QNET and SVM methods.

Table 1. Different input combinations related to QNET and SVM models

Effective Parameters	Combination
$\frac{H_T}{p}$	Combination 1
$Cd, \frac{H_T}{p}, \Theta, \frac{L_C}{W}$	Combination 2
$Cd, \frac{H_T}{p}, \frac{L_C}{W}$	Combination3
$Cd, \Theta, \frac{H_T}{p}$	Combination 4
$Cd, \frac{L_C}{W}$	Combination 5
$Cd, \Theta, \frac{L_C}{W}$	Combination 6
Cd, Θ	Combination 7

2.2. QNET

Currently, there is significant attention given to neural network modeling systems and their effectiveness in addressing data modeling problems. The QNET 2000 implements a neural network algorithm and features powerful software for creating and training backpropagation neural networks, effectively addressing various everyday problems. The above software is a post-error propagation neural modeling system, which is designed to increase the power of personal computers. The problems that can be solved with this software are unlimited. This software provides an advanced network design structure for generating complex networks, which uses the optimal training algorithm after error propagation. The advantages of this neural network include high speed, multiple training methods, a software help section for all models, fast and straightforward network design, easy data commonality and set of automatic tests for analysis. Additional model and training, complete cross-analysis of the learning process using network graphs and its powerful self-magnification structure, advanced network analysis tools, the ability to automatically save the network model during training, learning speed control side to automate network training, algorithms Numerous trainings, verification method with complete structure, the ability of integration of neural network models to everyday work space and example problems were pointed out. All these characteristics have made QNET 2000 the most powerful and convenient neural network software to use.

2.3. SVM

The Support Vector Machine (SVM) is an algorithm used for classification or pattern recognition, initially introduced by Vapnik in 1995. In recent years, SVM has been used as a new method in solving water engineering problems and hydraulic structures. The clear example supporting this statement is the current popularity of SVM compared to the past preference of neural network. Presently, most researchers tend to use SVM in their research work. In fact, the main reason is the usability of this method in solving various hydraulic problems. The theoretical foundation of the SVM classifier rests on the principle of linear classification. This involves dividing the data into two classes using a straight line (hyperplane in higher dimensions). SVM seek to find a hyperplane with the maximum margin, maximizing the distance between the closest data points of each class, as this leads to the most confident separation of the classes. In this scenario, we encounter solving a type of constrained optimization problem that can be solved by the Quadratic Programming method. Assuming linear separability of classes, hyperplanes with the maximum margin are obtained that separate the classes. When the data is not linearly separable, it is mapped to a higher-dimensional space to enable linear separation in this new space [46].

2.4. Performance evaluation indicators

In this research, the efficiency of the models is evaluated based on the following criteria:

1- The root mean square of errors (RMSE) is calculated using Equation 3.
2- Coefficient of determination (DC), or linear correlation between the observed and predicted values, indicates the strength of the correlation. A value closer to one suggests a better correlation of the data. The DC is calculated using the Equation 4.
3- The values for the square of the correlation coefficient (R^2), which is calculated using the Equations 5.

$$RMSE = \sqrt{\sum_{i=1}^{N} \frac{(Cdo-Cdp)^2}{N}} \quad (3)$$

$$DC = 1 - \frac{\sum_{i=1}^{N}(Cd_i^o - Cd_i^p)^2}{\sum_{i=1}^{N}(Cd_i^o - \overrightarrow{CDp})^2} \quad (4)$$

$$R^2 = \left(\frac{\sum_{i=1}^{N}(Cd_i^o - \overline{Cd^o})(Cd_i^p - \overline{Cd^p})}{\sqrt{\sum_{i=1}^{N}\left(Cd_i^o - \overline{Cd^o}\right)^2 \sum_{i=1}^{N}(Cd_i^p - \overline{Cd^p})^2}}\right)^2 \quad (5)$$

In the above equations, the parameters Cdp, Cdo and N are the predicted discharge coefficient, the observations of weirs, and the number of data, respectively. The above statistical criteria are calculated for the training and test stages.

3. Results and Discussion

As mentioned earlier, the purpose of this research is to compare the flow coefficient obtained from laboratory data with the predicted flow coefficient of QNET and SVM algorithms. The flow passing over the labyrinth weirs has a three-dimensional and complex structure; thus, it is not possible to solve it explicitly. Therefore, to calculate of the discharge coefficient relies on the general equation of weirs according to Equation 2.

3.1. Results of the QNET method

In this research, in order to achieve better and more accurate results, training and test data were evaluated using different percentages (60-40, 70-30, 80-20) and with node transfer functions in seven different combinations. Finally, the best combination according to the optimal levels of the evaluation indices was determined that the pattern (40-60) and with the hyperbolic secant transfer function (sech(x)) and one intermediate layers for most of the investigated parameters. In all the models of the current research, 60% of the data was used for training the network, while the remaining 40% were used for testing. The results for the combination are given in table (2) and the desired combination is number 2. This combination with inputs ($\frac{H_T}{p}$, Θ, $\frac{L_C}{W}$) has the lowest error (RMSE=0.0259) and the highest correlation coefficient (R^2=0.9850) and coefficient of determination (DC=0.9892) in the training phase. Also, this combination has showed the lowest error (RMSE=0.0292) and the highest correlation coefficient (R^2=0.9824) and explanation coefficient (DC=0.9788) in the test phase. Thus, it is selected as the best model for predicting the discharge coefficient of arched non-linear weirs.

Table 2. Evaluation criteria of different input combinations to determine the discharge coefficient for the QNET model

Train			Test			
R^2	RMSE	DC	R^2	RMSE	DC	Name of the combinations
0.8902	0.0366	0.89005	0.9345	0.03555	0.9033	$\frac{H_T}{p}$
0.9850	0.0259	0.9892	0.9824	0.0292	0.9788	$\frac{H_T}{p}, \Theta, \frac{L_C}{W}$
0.8907	0.0366	0.8907	0.9352	0.0355	0.9034	$\frac{H_T}{p}, \frac{L_C}{W}$
0.7811	0.0189	0.8809	0.9241	0.0191	0.8938	$\frac{H_T}{p}, \Theta$
0.000	0.164308	0.0002	0.0001	0.1667	-0.000735	$\frac{L_C}{W}$
0.2178	0.1598	0.21782	0.01121	0.1607	-0.1385	$\frac{L_C}{W}, \Theta$
0.0263	0.1787	0.0269	0.1825	0.1753	0.0787	Θ

Figure 3 illustrates the graphs depicting the distribution of experimental and predicted data for the best combination (second combination) during both the training and test phases. The values of R^2 indicate a linear relationship with a very favorable accuracy between the two values of the experimental and predicted data. The values of R^2 for the distribution diagram of the training phase are 0.9850 and in the test phase it is equal to 0.9824. The results in both stages of training and testing in the maximum and minimum points of the predicted points are almost more estimated than the experimental points.

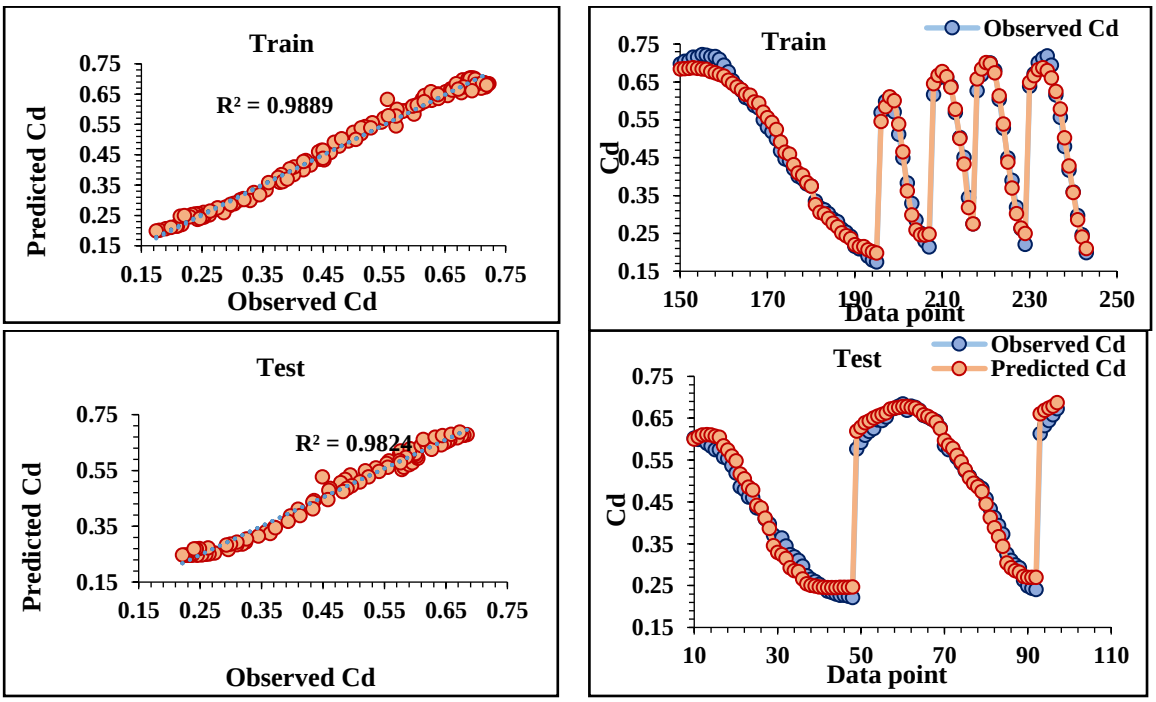


Figure 3. Data Distribution of experimental and predicted data during the training and test phases

Table (3) shows the statistical parameters of the sensitivity analysis related to the arched labyrinth weir. According to the relevant table, by removing the ($\frac{H_T}{p}$, Θ, $\frac{L_C}{W}$) parameters, RMSE and R^2 parameters have been calculated for both training and test phases. Notably, when ($\frac{H_T}{p}$) was removed, the resulting values indicated poorer performance compared to the removal of other parameters. This observation suggests that the most important parameter in determining the discharge coefficient of the arched labyrinth weirs is the total water load ratio parameter ($\frac{H_T}{p}$).

Table 3. Sensitivity analysis related to the QNET method

Train			Test			Remove the parameter	Combination
R^2	*RMSE*	*DC*	R^2	*RMSE*	DC		
0.9850	0.0259	0.9892	0.9824	0.0292	0.9788	-	$\frac{H_T}{P}$, Θ , $\frac{L_C}{W}$
0.8907	0.0366	0.8907	0.9352	0.0355	0.9034	Θ	$\frac{H_T}{P}$, $\frac{L_C}{W}$
0.7811	0.0189	0.8809	0.9241	0.0191	0.8938	$\frac{L_C}{W}$	$\frac{H_T}{P}$, Θ
0.2178	0.1598	0.21782	0.01121	0.1607	-0.1385	$\frac{H_T}{P}$	$\frac{L_C}{W}$, Θ

3.2. Results of the SVM method

In this research, in order to achieve better and more accurate results, training and test data with different percentages (40-60, 30-70, 20-80) and with appropriate gamma value and with RBF radial function in seven combinations was evaluated. Finally, the best combination for the optimal levels of the evaluation indices was determined that the 40-60 pattern with a gamma value of 10 leading to the best results for most of the investigated parameters. Currently, 60% of the data were used for training the model, while the remaining 40% were used for testing.

The results for all combinations are presented in Table (4) and the most desirable combination is the combination number 2. This combination with inputs ($\frac{H_T}{P}$, Θ, $\frac{L_C}{W}$) has the lowest error (RMSE=0.0199) and the highest correlation coefficient (R^2=0.9881) and coefficient of determination (DC=0.9853) in the test phase. As a result, it is chosen as the best model for predicting the discharge coefficient of arched labyrinth weirs.

Table 4. Evaluation criteria of different input combinations to determine the discharge coefficient for the SVM model

Train			Test			
R^2	RMSE	DC	R^2	RMSE	DC	Name of the combination
0.9512	0.03651	0.9518	0.9534	0.0356	0.9533	$\frac{H_T}{p}$
0.9889	0.0189	0.9870	0.9881	0.0199	0.9853	$\frac{H_T}{p}$, Θ , $\frac{L_C}{W}$
0.9512	0.0367	0.9512	0.9534	0.0357	0.9529	$\frac{H_T}{p}$, $\frac{L_C}{W}$
0.9888	0.0184	0.9512	0.9882	0.0199	0.9853	$\frac{H_T}{p}$, Θ
0.0000	0.1644	0.0238	0.000	0.1667	-0.027	$\frac{L_C}{W}$
0.0571	0.0256	0.0758	0.0668	0.1607	0.0446	$\frac{L_C}{W}$, Θ
0.0527	0.1688	-0.0292	0.0502	0.1653	-0.010	Θ

Figure 4 shows the graphs related to the distribution of experimental and predicted data for the best combination (second combination) in the training and test phase. The values (R^2) show a linear relationship with a very favorable accuracy between the two values of the experimental and predicted data. The values of (R^2) for the distribution diagram in the training phase are (0.9881) and in the test phase it is equal to (0.9889). The relevant results in both stages of training and test have estimated the predicted points at the maximum points almost more than the experimental points and at the minimum points almost less.

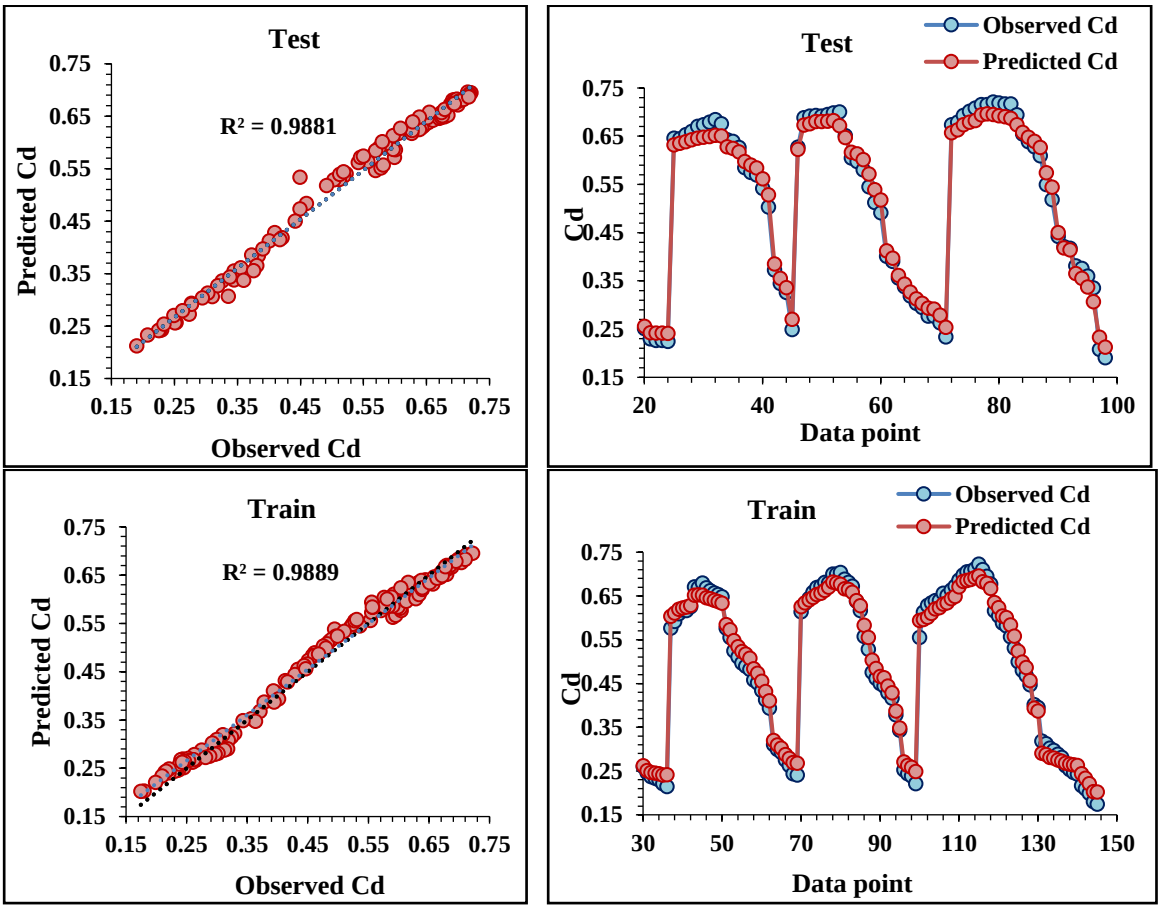


Figure 4. Data Distribution of experimental and predicted data in the training and test phases

Table (5) shows the statistical parameters of the sensitivity analysis of arched labyrinth weir. According to the presented table, by removing the ($\frac{H_T}{p}$, Θ, $\frac{L_C}{W}$) parameters, RMSE and R2 parameters have been calculated for both training and test phases. Notably, when ($\frac{H_T}{p}$) was removed, the resulting values indicated poorer performance compared to removal of other parameters. This observation suggests that the most important parameter in determining the discharge coefficient of the arched labyrinth weir is the total water load ratio parameter ($\frac{H_T}{p}$).

Table 5. Sensitivity analysis of the SVM model

Train			Test			Remove the parameter	Combination
R^2	RMSE	DC	R^2	RMSE	DC		
0.9889	0.0189	0.9870	0.9881	0.0199	0.9853	-	$\frac{H_T}{P}$, Θ , $\frac{L_C}{W}$
0.9512	0.0367	0.9512	0.9534	0.0357	0.9529	Θ	$\frac{H_T}{P}$, $\frac{L_C}{W}$
0.9888	0.0184	0.9512	0.9882	0.0199	0.9853	$\frac{L_C}{W}$	$\frac{H_T}{P}$, Θ
0.0571	0.0256	0.0758	0.0668	0.1607	0.0446	$\frac{H_T}{P}$	$\frac{L_C}{W}$, Θ

4. Comparing the results of two investigated models (QNET-SVM)

Figure 5 illustrates a bar chart of experimental and predicted data for the arched labyrinth weir with cycle wall angle of α = 6° related to the best combination, which includes the parameters ($\frac{H_T}{p}$, Θ, $\frac{L_C}{W}$) for both QNET and SVM models in the test phase. Figure 5 shows that the SVM model exhibit a superior performance compared to the QNET model.

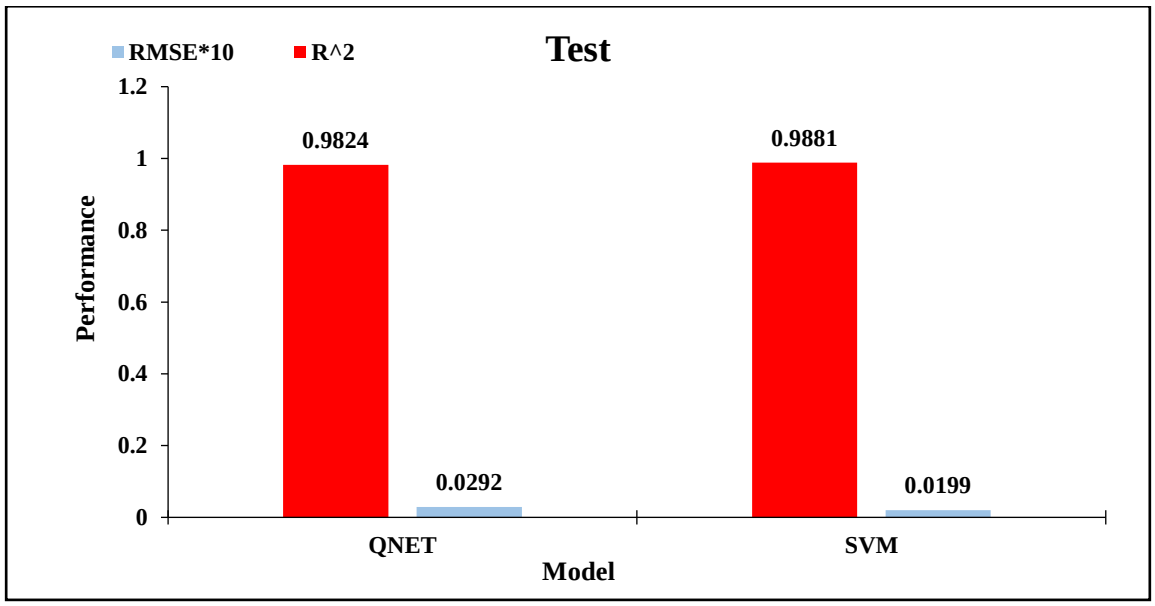


Figure 5. Comparing the results of QNET and SVM models in the test phase

5. Conclusion

In this research, the QNET and SVM algorithms were employed using the laboratory data of Crookston's research (2010) to predict the discharge coefficient of the labyrinth weir. The study is focused on the evaluating the performance of QNET and SVM algorithms in predicting the discharge coefficient of arched labyrinth weirswith a cycle angle of 6 degrees, utilizing 243 data series. The results of the sensitivity analysis showed that the total water load ratio ($\frac{H_T}{p}$) is an effective parameter in determining the discharge coefficient (Cd) of the arched labyrinth weird. According to the results of this study, the second combination with parameters (Cd, $\frac{H_T}{p}$, Θ, $\frac{L_C}{W}$) outperforms the other combinations.

References

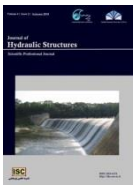
1. Gentilini, B., (1949). Stramazzi con cresta a pianta obliqua e a zig-zag. Memorie e Studi dell instituto di Idraulica e Construzioni Idrauliche Del Regil Politecnico di Milano, 48, in Italian.
2. Crookston B.M. 2010. Labyrinth weirs. Ph.D. thesis, Utah State Univ., Logan, UT.
3. Tison, G., and Fransen, T., (1963). Essais sur Deversoirs de forme Polygonal en Plan. Revue C., Brussels, Belgium, Vol. 3, 1963, pp. 38-51.
4. Taylor G. 1968. The performance of Labyrinth weirs, thesis presented to university of Nottingham, England.
5. Hay, S., Taylor, G., (1970). Performance of Labyrinth Weirs. ASCE J. of Hydraulic Engg. 96(11):2337-57.
6. Darvas, L.A., (1971). Performance and Design of Labyrinth Weirs. J. Hydr. Engg. ASCE. 97(8):1246-1251.
7. Indlekofer, H., Rouve, G., (1975). Discharge over Polygonal Weirs. J. Hydr. Div., 101(3), 385-401.
8. Cassidy, J.J., Christopher, F., Gardner, A., Robert, T., Peacock, M., (1985). Boardman Labyrinth-Crest.
9. Tacail, F.G., Even, B., Babb, A., (1990). Case Study of a Labyrinth Weir. Canadian Journal of Civil Engineering, 17, 1-7.
10. Tullis, B.P., Amanian, N., Waldron, N., (1995). Approach to Improve the Discharging Capacity of Design of Labyrinth Weirs. ASCE J. of Hyraulic Sharp-Crested Triangular Plan form Weirs.J. Flow Engg.121 (3):247-55.
11. Wormleaton, P.R., Soufiani, E., (1998). Aeration of Included Angle and Sill Slope on Air Entrainment of Triangular Planform Labyrinth Weirs. J. Hydraul. Eng. 2005.
12. Wormleaton, P.R., Tsang, C.C., (2000). Aeration Performance of Rectangular Planform Labyrinth Weirs. J. Environ. Eng. 2000.126:456-465.
13. Ghodsian, M., (2007). Stage-Discharge Relationship for a triangular Labyrinth Weir.Proc. Inst. Eng. Water Manage. 162(3), 173-178.
14. Zerihun, Y.T. and Fenton, J.D. (2007). A Boussinesq-type model for flow over trapezoidal profile weirs. Journal of Hydraulic Research, 45(4), 519-528.
15. Kabiri-Samani, A.R., Ansari, A., and Borghei, S.M. (2010). Hydraulic behaviour of flow over an oblique weirs. J. [1] Hydraulic Research. 48(5), 669-673.
16. Carollo, F.G., Ferro, V., Pampalone, V., (2012). Experimental Investigation of the Outflow Process over a Triangular Labyrinth-Weirs. J. Irrig. Drian Eng., 10.106/(ASCE) IR. 1943-4774.0000366, 138:73-79.
17. Crookstone, B.M., Tullis, B.P., (2013). Hydraulic Design and Analysis of Labyrinth Weirs. I: Discharge Relationships. J. Irrig. Drain. Eng., 139:363-370.
18. Dabling, M.R. (2014). Nonlinear weirs hydraulics. M.Sc. Thesis. Utah State University, Logan, UT.
19. Seo, I.W., Do, K.Y., Park, Y.S. and Song, C.G. (2016). Weirsdischarges by modification of weirs shapes and weirssurroundings. Environmental Earth Science, 75(6):496-509.
20. Christensen, N.A., Tullis, B.P., (2012). Arced Labyrinth Weirs Flow Characteristics. 4th International Junior Reasercher and Enginner Workshap on Hydraulic Structures. IJREWHS' 12. B. Tullis and R. Janssen (Eds.) Utah State University, Logan, USA.
21. Cimen M, 2008. Estimation of Daily suspended sediments using Support Vector Machine, Hydrological sciences Jurnal: 53 (3), 656-666.

22. Kakai Lafdani, A. Pour Nemat Rudsari, A. Kadri, K. Moghadamnia, A. (2011). Forecasting the volume of suspended sediments using GMDH and SVM models based on principal component analysis, 9th International Seminar on River Engineering, Ahvaz, and University Martyr of Chamran.
23. Guven, A., Azamathulla, H. Md., and Zakaria, N.N., (2009) , Linear genetic programming for prediction of circular pile scour, Ocean Engineering, Vol. 36, pp. 985-991.
24. Azamathulla, H. Md., Ghani, A.A., Nor Azazi, Z. and Aytac G., (2010), Genetic Programming to Predict Bridge Pier Scour, J. OF Hydraulic Engineering, Technical Note, ASCE.
25. Goyal, M.K., Ojha, C.S.P., 2011. Estimation of scour downstream of a ski-jump bucket using support vector and M5 model tree. Water Resour. Manage. 25, 2177–2195.
26. Azhdari Moghadam, M. and Jafari Nadushan, A. (2013).Computational hydrodynamics. Scientific-research journal of Imran Modares.
27. Abbaspour, A. and Arvanaghi, H. (2011). Forecasting the flow on the triangular-rectangular compound weirsusing planning.
28. Farrokhy, A., Givachy, A, And Azhdary moghaddam. (2009). Estimating Determining the Discharge Coefficient of lateral weirs with neural network and adaptive neural-inference system. 6th National Labyrinth of Civil Engineering, Semnan University, Iran. (In Farsi).
29. Karami H., Karimi S., Bonakdari H., Shamshirband Sh. 2016 Predicting discharge coefficient of triangular labyrinth weirs using extreme learning machine, artificial neural network and genetic programming. Neural Comput & Applic, 29(11), 983- 989.
30. Roushangar, K., R. Khoshkanar, and J. Shiri. 2016. Predicting Trapezoidal and Rectangular Side Weirs Discharge Coefficient Using Machine Learning Methods. ISH Journal of Hydraulic Engineering, 22: 1-8.
31. Parsaie, A. and Haghiabi, A.H. (2017). Support Vector Machine to predict the discharge coefficient of Sharp crested w-planform weirs. AUT Journal of Civil Engineering, 1(2): 195-204.
32. Majedi Asl, M., Fuladi-Panah, M. (2017). The use of evolutionary systems in determining the discharge coefficient of triangular labyrinth weirs. Journal of Water and Soil Sciences. Journal of Agricultural Sciences and Techniques and Natural Resources, 1.14: 279-290.
33. Majedi Asl, M. and Fuladipanah M. (2018). Application of the Evolutionary Methods in Determining the Discharge Coefficient of Triangular Labyrinth Weirs. Journal of Water and Soil Science (Science and Technology of Agriculture and Natural Resources), 22(4), 279-290 (In Farsi)
34. Roushangar, K., Alami M. T., Shiri J. and Majedi Asl, M. (2018). Determining discharge coefficient of labyrinth and arced labyrinth weirs using support vector machine. Hydrology Research, 49(3): 924-938.
35. Mehri, Y., Esmaeili, S., Soltani, J., Saneie, S. and Rostami, M. (2018). Evaluation of SVM and nonlinear regression models for predicting the discharge coefficient of side piano key weirs in irrigation and drainage networks. Iranian Journal of Irrigation and Drainage, 12(70): 994-1003(in Persian).
36. Parsaie, A., Haghiabi, A.H. and Shamsi Z. (2019). Intelligent mathematical modeling of discharge coefficient of nonlinear weirs with triangular plan. AUT Journal of Civil Engineering, 3(2): 149-156.
37. Kumar, M., Sihag, P., Tiwari, N.K. and Ranjan S. (2020). Experimental study and modelling discharge coefficient of trapezoidal and rectangular piano key weirs. Applied Water Science, 10, 43-52.

38. Fouladipanah, M., M. Majedi Asl and A. Haghgooyi (2020). Application of Intelligent Algorithm to Model Head-Discharge Relationship for Submerged Labyrinth and Linear Weirs. Hydraulic Journal, No. 15, Volume 2, pp. 149-164.
39. Majedi-Asl, M., Foladipanah, M., Arun, V., & Tripathi, R. P. (2021). Using data mining methods to improve discharge coefficient prediction in Piano Key and Labyrinth weirs. Water Supply.
40. Roushangar, K., Majedi-Asl, M. and Shahnazi, S. (2021). Hydraulic Performance of PK Weirs Based on Experimental Study and Kernel-based Modeling. Water Resources.
41. Omidpour Alavian, T., and Majedi-Asl, M, Sohrabi, F, Shamsi, V. and Ayami, M. (2022c). Modeling and evaluation of the discharge coefficient of an arched Labyrinth with the Qnet met model method, the first modern national conference in civil and environmental engineering. Ramsar, Iran.
42. Omidpour Alavian, T., Majedi-Asl, M, Soltani, M, Mohammadi, E. and Shamsi, V. (2022b). Comparison of the hydraulic efficiency of Labyrinth Weirs with quarter-circle and semi-circular crest shape using met model method (ANN), 8th.International Labyrinth on Civil Engineering, Architecture and Urban Development / 07-09 March. 2023, Tehran, Iran.
43. Majedi Asl, M., Omidpour Alavian, T and Kouhdaragh, M. (2023). Comparison of The Hydraulic Efficiency of labyrinth Weirs with a Quarter and Semi-Circular Crest Shape Using Neural Networks (QNET, SVM, GEP, ANN). Iranian Journal of Irrigation and Drainage No.4, Vol. 17, Oct.-Nov. 2023, p. 787-804.
44. Majedi Asl, M., Omidpour Alavian,, Kouhdaragh, M and Shams, V. (2023).Comparison of Hydraulic Efficiency of Arched Non-linear Weirs in Plan Using GEP and SVM Neural Networks. Journal of Water and Soil Science Vol. 27, No. 3, Fall 2023, Isfahan University of Technology, Isfahan, Iran.
45. Henderson, FM (1966) open channel flow. Macmillan, New York, USA.
46. V.N. Vapnik, The nature of statistical learning theory, Springer, New York, 1995.

© 2024 by the authors. Licensee SCU, Ahvaz, Iran. This article is an open access article distributed under the terms and conditions of the Creative Commons Attribution 4.0 International (CC BY 4.0 license) (http://creativecommons.org/licenses/by/4.0/).

Journal of Hydraulic Structures
J. Hydraul. Struct., 2024;10(2):46-54
DOI: 10.22055/JHS.2024.19041



OPEN ACCESS

Investigating and predicting hydraulic jump energy loss with threshold (Experimental and regression analysis)

Hamidreza Abbaszadeh [*1]
Parisa Ebadzadeh [2]
Rasoul Daneshfaraz [2]
Reza Norouzi [2]

Abstract

The present investigation delves into the intricate dynamics surrounding the incorporation of thresholds and their consequential impact on parameters associated with hydraulic jumps—a phenomenon critical to the efficient functioning of the gates. In the pursuit of a comprehensive understanding, the study employed experimental models of thresholds crafted from polyethylene. These models underwent meticulous examination, encompassing variations in dimensions, widths, and positions relative to the gate. The positions explored included beneath the gate, tangent to the gate upstream, and downstream, each contributing unique insights into the behavior of water flow and energy dissipation. An intriguing outcome emerged as thresholds were introduced at different locations. The energy dissipation for a given gate opening exhibited a discernible increase, shedding light on the intricate relationship between threshold placement and hydraulic performance. Notably, as the initial depth relative to the secondary depth increased, a consequential decrease in the $\Delta E_{AB}/y_A$ was observed, signaling a convergence between the initial and secondary depths. Further illuminating the findings, a comparative analysis of energy loss was conducted across all three threshold positions—beneath the gate, tangent to the gate upstream, and downstream. This scrutiny uncovered a distinct pattern, indicating a heightened energy dissipation in scenarios where the threshold was submerged, setting it apart from conditions where the threshold was positioned otherwise. In essence, the investigation not only accentuates the intricate interplay between sluice gates, thresholds, and hydraulic parameters but also underscores the importance of considering the placement of thresholds in optimizing the energy dissipation efficiency of these hydraulic structures.

Keywords: Gate, Hydraulic Jump, Threshold, Regression Equation.

Received: 09 November 2023; Accepted: 16 April 2024

[*] E-mail: ha.abbaszadeh@tabrizu.ac.ir (**Corresponding Author**)
[1] Department of Civil Engineering, Faculty of Civil Engineering, University of Tabriz, Tabriz, Iran.
[2] Department of Civil Engineering, Faculty of Engineering, University of Maragheh, Maragheh, Iran.

CC BY

1. Introduction

The gates represent hydraulic structures where water movement occurs beneath the gate. Among the common types is the vertical lift gate, adjusting its opening vertically in the flow path for precise control of upstream water level, discharge regulation, and estimation of the gate discharge coefficient. The influx of water velocity into channels induces oscillatory waves, causing erosion of the channel bed downstream. Consequently, designing stilling basins becomes crucial to prevent excessive energy dissipation while maintaining downstream water depth above the secondary depth to mitigate jumps. Understanding flow behavior in diverse threshold positions enhances hydraulic performance and water distribution efficiency in irrigation networks. The use of a combined gate-threshold structure reduces upstream water depth, diminishing the force on the gate and increasing the flow coefficient. Hydraulic jump is a fundamental phenomenon in the field of open-channel hydraulics that necessitates precise management and control. Various factors, including water flow velocity, irregularities, and geometric changes in the channel, can have a significant impact on the occurrence of this phenomenon. Considering these factors in the design and management of open channels can enhance the performance of irrigation systems and prevent sudden issues associated with the hydraulic jump phenomenon.

The understanding of hydraulic and geometric parameters associated with gates has been the subject of numerous analytical and laboratory studies, as documented in a range of scholarly works [1-11]. Among these investigations, Abdelmonem et al. [12] made notable contributions by focusing on energy dissipation downstream of flap gates, particularly in the presence of a submerged threshold. Their findings revealed a remarkable 20% increase in hydraulic jump efficiency under these conditions, emphasizing the potential benefits of incorporating submerged thresholds in hydraulic structures equipped with flap gates.

In a related study, Habibzadeh et al. [13] delved into the hydraulic jump characteristics downstream of flap gates. Their scrutiny unveiled a correlation between an increases in the Froude number and escalated surface wave oscillations. This observation highlights the sensitivity of hydraulic jump dynamics to flow parameters, with implications for the overall efficiency and stability of hydraulic systems featuring flap gates.

Another significant contribution comes from Abbaszadeh et al. [14], who investigated hydraulic jump characteristics with a threshold. Their study underscored the role of the threshold in enhancing energy dissipation, providing valuable insights into the design considerations for hydraulic structures. The incorporation of thresholds in such systems can contribute to optimizing energy dissipation processes and improving overall hydraulic performance.

Furthermore, Abbaszadeh et al. [15] conducted experimental research to explore the impact of a threshold on flow characteristics. Their findings revealed a reduction in hydrodynamic force exerted on the gate, suggesting that the presence of a threshold not only influences energy dissipation but also has implications for the structural forces experienced by the hydraulic components.

In summary, these studies collectively contribute to advancing our understanding of flap gates and their interactions with hydraulic jumps. The insights gained from these investigations have implications for the design and optimization of hydraulic structures, with the potential to enhance energy dissipation efficiency and overall system performance.

As part of efforts to improve the hydraulic performance and increase the efficiency of water distribution in irrigation networks and channels, a comprehensive study was undertaken. The study focused on exploring the use of a gate-threshold structure in various locations, with the aim of determining the most effective placement to enhance the distribution of water in irrigation

networks and channels. The gate-threshold structure was tested in three different locations, namely below the gate, tangent to the gate upstream, and tangent to the gate downstream. The effectiveness of the structure was examined in each location, and data was collected to determine its impact on the hydraulic performance and efficiency of the overall system. The study aimed to provide valuable insights into the optimal location for the gate-threshold structure to be placed in order to achieve the best results for water distribution in irrigation networks and channels. The findings of the study will be useful in improving the efficiency of irrigation systems and ensuring that resources are utilized optimally.

2. Materials and Methods

Experiments in this study were conducted in a laboratory flume featuring a rectangular cross-section (length: 5 meters, width: 0.3 meters, height: 0.5 meters) constructed with transparent Plexiglas walls and floor, facilitating precise observation of flow details. The channel bed slope was adjustable, set at zero for experimentation. Two pumps with a nominal power of 450 liters per minute provided inflow to the flume. Rotameters installed on the flume measured the inflow discharge. To mitigate turbulence from the inlet, several parallel calmers were employed at the beginning of the flume. A point depth gauge mounted on a movable rail measured water depth in the flume. Depths were measured at four points across the width of the cross-section, with their average considered the final depth. Experiments were conducted in two conditions: without a threshold and with a threshold at various gate openings. Thresholds made of polyethylene, with a thickness of 5 centimeters, height of 3 centimeters, and width (B) ranging from 2.5 to 30 centimeters, were positioned beneath the gate, tangent to the gate upstream, and tangent to the gate downstream. Figures (1) and (2) illustrate the flume and thresholds, respectively.

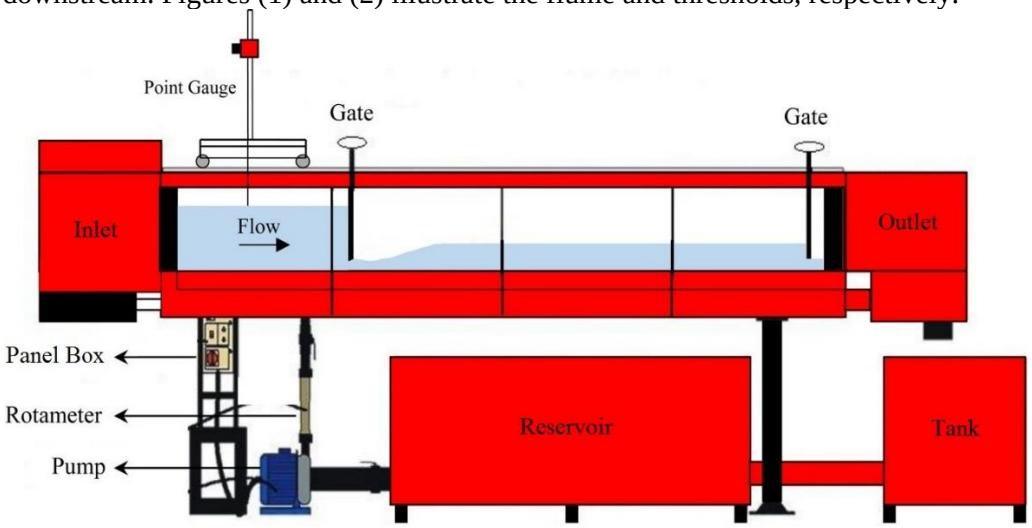


Figure 1. Schematic view of the flume

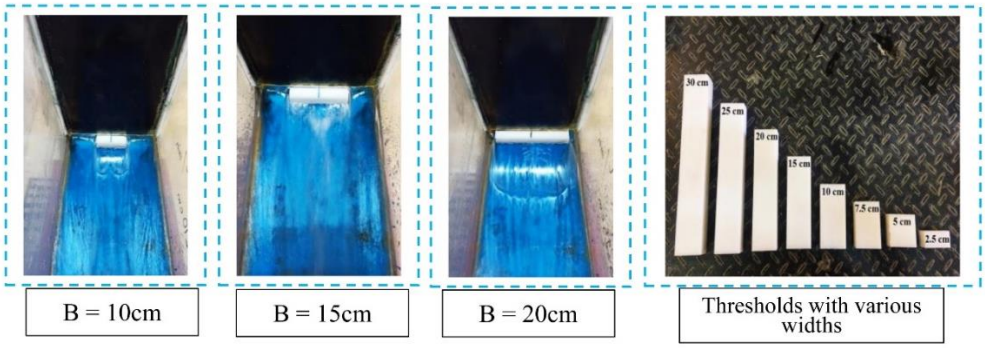


Figure 2. The view (x-y section) of the threshold with different placement relative to the gate

3. Results and Discussion

The relationship between the energy loss relative to initial depth ($\Delta E_{AB}/y_A$) and the ratio of initial depth to hydraulic jump secondary depth (y_A/y_B) is a crucial aspect in understanding the hydraulic behavior of flow through openings. As depicted in Figure (3a and b), the total openings of 4 and 5 centimeters provide insights into the dynamics of energy dissipation. The variation in $\Delta E_{AB}/y_A$ with changing y_A/y_B ratios reveals intriguing patterns.

An intriguing observation is the consistent decrease in the $\Delta E_{AB}/y_A$ value with an increase in the y_A/y_B ratio. This trend suggests a convergence of initial and secondary depths, culminating in the formation of a weak hydraulic jump with minimal energy loss. The interplay between these parameters highlights the intricate balance governing the efficiency of energy dissipation in hydraulic systems.

Furthermore, the influence of the y_A value on the Froude number and subsequent energy loss is noteworthy. An increase in y_A corresponds to a decrease in the Froude number, contributing to an overall reduction in energy loss. This relationship underscores the importance of threshold width in modulating the hydraulic characteristics of the flow. The findings in Figure (3) illuminate the trade-off between threshold width and energy dissipation efficiency.

Interestingly, the highest energy loss is pinpointed at the y_A/y_B=0.1 ratio, as indicated in Figure (3). This particular ratio signifies a critical point where, at a constant discharge, an increase in threshold width leads to a reduction in secondary depth, consequently amplifying energy loss. This observation provides valuable insights for optimizing hydraulic structures, emphasizing the significance of maintaining a delicate balance between opening dimensions and energy dissipation efficiency.

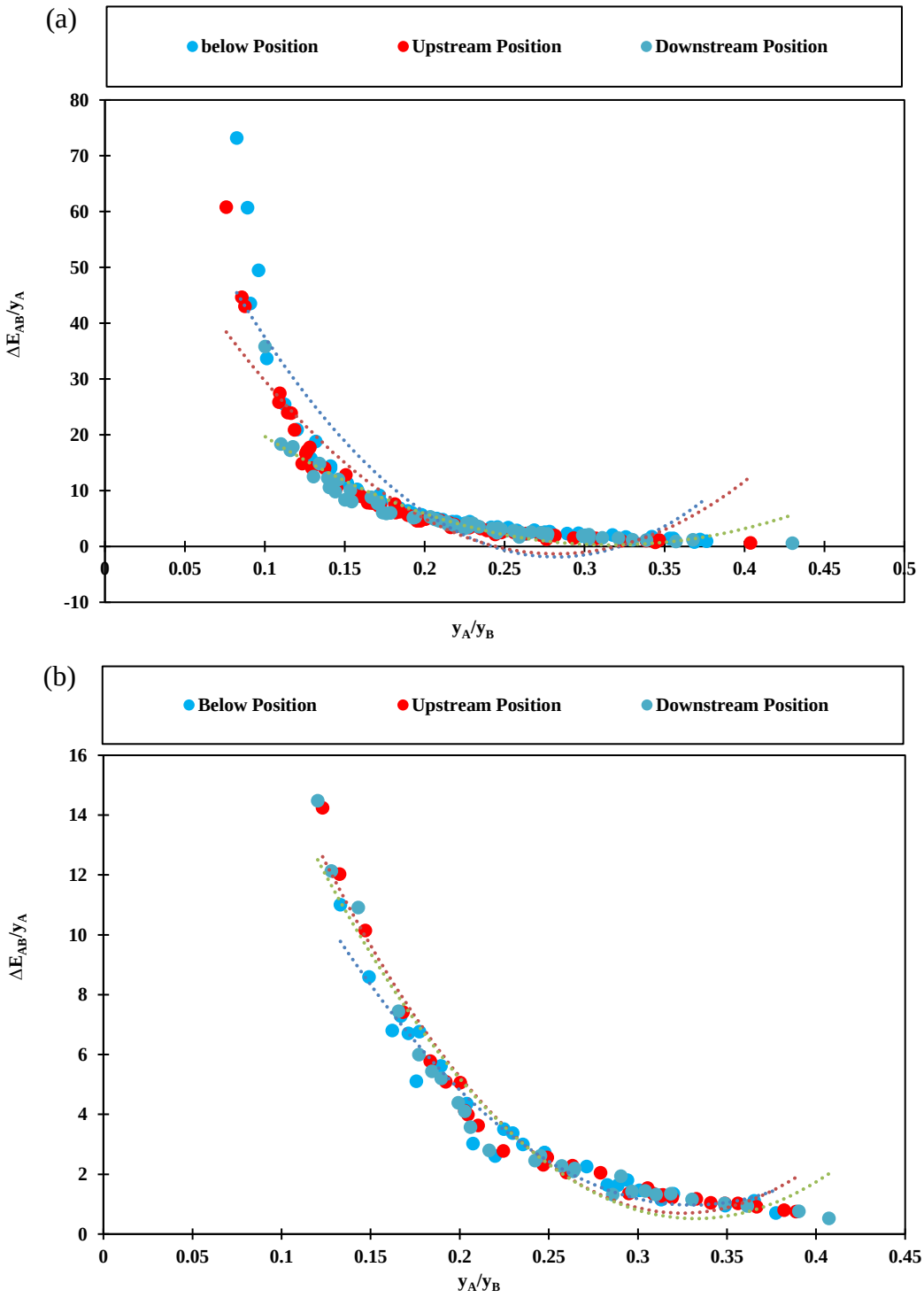


Figure 3. The value of $\Delta E_{AB}/y_A$ and y_A/y_B for various locations of the threshold placement a) 4 cm opening, b) 5 cm opening

To predict energy loss relative to specific energy at the upstream and downstream in the presence of a threshold, Equations (1) and (2) have been proposed.

In conclusion, the introduction of Equations (1) and (2) enhances our ability to model and understand energy dissipation in hydraulic jump scenarios. These equations provide a practical and accurate framework for predicting energy losses relative to specific energy, thereby contributing to the optimization and design of hydraulic structures for improved performance in the presence of thresholds.

$$\frac{\Delta E_{AB}}{E_A} = -3.067 Fr_A^{-0.778} + 1.692\left(\frac{y_B}{y_A}\right)^{-1.073} + 0.004\left(\frac{B}{y_A}\right)^{-9.083} + 1.161\left(\frac{B}{y_B}\right)^{0.001} \quad (1)$$

$$\frac{\Delta E_{AB}}{E_B} = 0.486 Fr_A^{1.180} - 0.175\left(\frac{y_B}{y_A}\right)^{1.228} + 0.012\left(\frac{B}{y_A}\right)^{-6.197} - 0.537\left(\frac{B}{y_B}\right)^{0.008} \quad (2)$$

The statistical indexes of percentage relative error (RE%), root mean square error (RMSE), and Kling Gupta efficiency (KGE) were used to evaluate the equations.

$$RE\% = \frac{X_{Obs} - X_{cal}}{X_{Obs}} \times 100 \quad (3)$$

$$RMSE = \sqrt{\frac{\sum_{i=1}^{n}(X_{Obs} - X_{Cal})_i^2}{n}} \quad (4)$$

$$KGE = 1 - \sqrt{(R-1)^2 + (\beta-1)^2 + (\gamma-1)^2}$$

$$\beta = \frac{\overline{X_{Cal}}}{\overline{X_{Obs}}}, \gamma = \frac{CV_{Cal}}{CV_{Obs}} = \frac{\sigma_{Cal}/\overline{X_{Cal}}}{\sigma_{Cal}/\overline{X_{Obs}}}$$

$$R = \frac{[\sum_{i=1}^{n}(X_{Obs\,i} - \overline{X_{Obs}}) \times (X_{Cal\,i} - \overline{X_{Cal}})]}{\sum_{i=1}^{n}(X_{Obs\,i} - \overline{X_{Obs}}) \sum_{i=1}^{n}(X_{Cal\,i} - \overline{X_{Cal}})}$$

$0.7 < KGE < 1$ "Very good"
$0.6 < KGE < 0.7$ "Good"
$0.5 < KGE \leq 0.6$ "Satisfactory"
$0.4 < KGE \leq 0.5$ "Acceptable"
$KGE \leq 0.4$ "Unsatisfactory" (5)

Equations (3) and (4), both approaching zero, are indicative of a high level of accuracy in the solutions. This is consistent with the common practice where smaller differences between observational (Obs) and computational (Cal) results signify a closer match and, consequently, a more accurate representation of the observed phenomena [16].

Equation (5) involves several parameters: R (coefficient of correlation), β (average of calculated values to observed values), and γ (standard deviation of calculated values to observed values). The correlation coefficient provides a measure of the linear relationship between the two datasets. A value close to 1 indicates a strong positive correlation, reinforcing the reliability of the computational results.

The ratios β and γ offer insights into the central tendency and variability of the data, respectively. A β ratio close to 1 suggests that the average of the calculated values aligns well with the average of the observed data. Similarly, a γ ratio close to 1 implies that the standard deviation of the calculated values is in good agreement with the standard deviation of the observed values [5].

The KGE (Kling-Gupta Efficiency) statistical index, mentioned in relation to Equation (5) and categorized into levels such as very good, good, satisfactory, acceptable, and unsatisfactory, serves as an overarching measure of the accuracy of the solutions [17]. A higher KGE index

suggests a more accurate representation of the observed data by the computational model.

In conclusion, these equations collectively provide a comprehensive framework for evaluating the accuracy of computational results relative to observational data. The emphasis on correlation, central tendency, variability, and the KGE index underscores the multifaceted nature of accuracy assessment, enabling a nuanced understanding of the reliability of the computational solutions.

Figure (4) presents a comprehensive comparison between experimental results and computational simulations, shedding light on the accuracy and reliability of the models in predicting energy dissipation relative to both upstream and downstream conditions. The juxtaposition of experimental and computational data allows for a nuanced evaluation of the predictive performance.

The statistical evaluation of the computational models against the experimental data is instrumental in assessing their fidelity. For Equation (1), the statistical indices reveal a maximum relative error of 8.53%, an average relative error of 0.78%, and a root mean square error of 0.004. Notably, the KGE for relation (1) falls within the "very good". These metrics collectively affirm the robustness of the computational model in accurately capturing the energy dissipation dynamics relative to upstream and downstream parameters.

Similarly, for Equation (2), the statistical indices exhibit a maximum relative error of 12.15%, an average relative error of 0.87%, and a root mean square error of 0.009. The KGE for Equation (2) also falls into the "very good" category. These results underscore the efficacy of the computational approach in providing reliable predictions, with a minor increase in error compared to Equation (1). The overall "very good" categorization indicates a high level of agreement between the computational simulations and experimental observations.

In summary, the comparative analysis in Figure (4) and the associated statistical indices validate the accuracy of both Equation (1) and Equation (2) in predicting energy dissipation. The "very good" categorization of the KGE index further enhances the credibility of the computational models, offering confidence in their application for understanding and predicting energy dissipation phenomena in hydraulic systems.

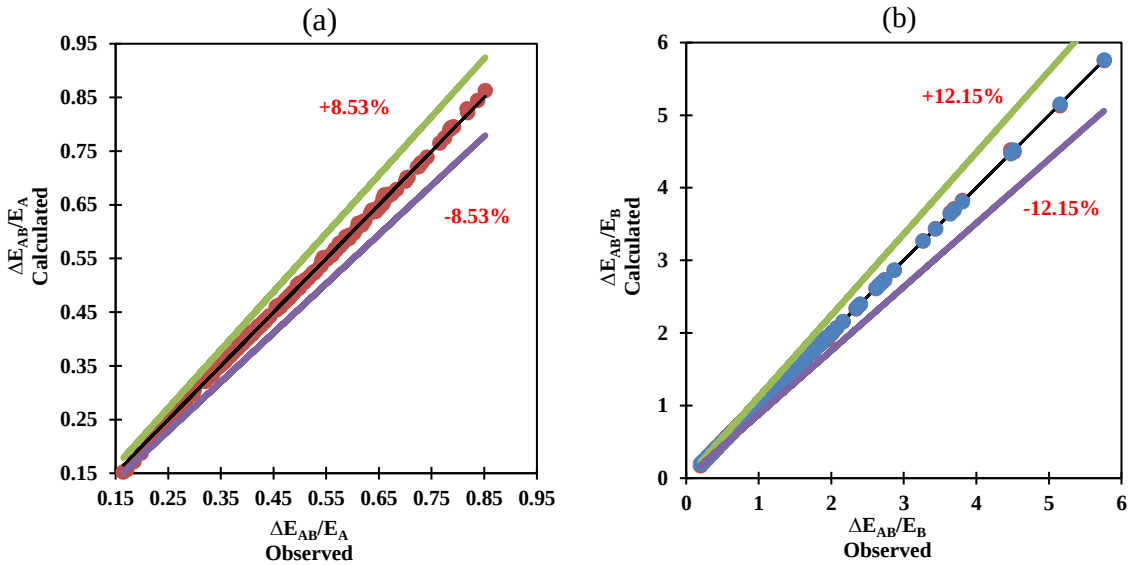


Figure 4. The values of calculated energy loss against observed data

4. Conclusion

This study examined the hydraulic jumps at varying gate openings, considering both threshold and non-threshold conditions, and accounting for various widths and positions relative to the gate. The experimental investigation encompassed a discharge range spanning from 150 to 850 liters per minute. The findings highlight that, in the absence of a threshold, downstream hydraulic jumps exhibit a decrease in relative energy loss as the gate opening increases.

Within specific gate openings, the introduction of a threshold, positioned both below the gate and tangent to the gate upstream and downstream, correlates with heightened energy dissipation. A notable observation is the decrease in the $\Delta E_{AB}/y_A$ value with an increasing ratio of initial depth to secondary depth. This decrease signifies the convergence of initial and secondary depths, leading to the formation of a weak jump characterized by minimal energy loss. Comparative analysis across all three threshold conditions—below the gate and tangent to the gate upstream and downstream—reveals a higher energy dissipation in the sub-threshold condition compared to other threshold scenarios.

In this current investigation, the study also derived general equations for calculating energy loss under threshold conditions. The accuracy of these equations was rigorously assessed using various statistical indices, including Relative Error, Root Mean Square Error, and Kling Gupta Efficiency. The results affirm the high precision of the presented equation, endorsing its utility in predicting relative energy loss with confidence.

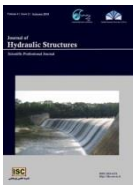
References

1. Alhamid AA, (1999). Coefficient of discharge for free flow sluice gates. Journal of King Saud University-Engineering Sciences, 11(1): 33-47.
2. Salmasi F, Abraham J, (2021). Prediction of discharge coefficients for sluice gates equipped with different geometric sills under the gate using multiple non-linear regression (MNLR). Journal of Hydrology, 597: 125728.
3. Ghorbani MA, Salmasi F, Saggi MK, Bhatia AS, Kahya E, Norouzi R, (2020). Deep learning under H2O framework: A novel approach for quantitative analysis of discharge coefficient in sluice gates. Journal of Hydroinformatics, 22(6): 1603-1619.
4. Daneshfaraz R, Norouzi R, Abbaszadeh H, Azamathulla HM, (2022). Theoretical and experimental analysis of applicability of sill with different widths on the gate discharge coefficients. Water Supply, 22(10): 7767-7781.
5. Daneshfaraz R, Norouzi R, Abbaszadeh H, Kuriqi A, Di Francesco S, (2022). Influence of sill on the hydraulic regime in sluice gates: an experimental and numerical analysis. Fluids, 7(7): 244.
6. Hassanzadeh Y, Abbaszadeh H, (2023). Investigating Discharge Coefficient of Slide Gate-Sill Combination Using Expert Soft Computing Models. Journal of Hydraulic Structures, 9(1): 63-80.
7. Daneshfaraz R, Abbaszadeh H, Gorbanvatan P, Abdi M, (2021). Application of sluice gate in different positions and its effect on hydraulic parameters in free-flow conditions. Journal of Hydraulic Structures, 7(3): 72-87.
8. Norouzi R, Ebadzadeh P, Sume V, Daneshfaraz R, (2023). Upstream vortices of a sluice gate: An experimental and numerical study. AQUA—Water Infrastructure, Ecosystems and Society, 72(10): 1906-1919.
9. Daneshfaraz R, Norouzi R, Ebadzadeh P, (2022). Experimental and numerical study of sluice gate flow pattern with non-suppressed sill and its effect on discharge coefficient in free-flow conditions. Journal of Hydraulic Structures, 8(1): 1-20

10. Daneshfaraz R, Norouzi R, Ebadzadeh P, Di Francesco S, Abraham JP, (2023). Experimental study of geometric shape and size of sill effects on the hydraulic performance of sluice gates. Water, 15(2): 314.
11. Daneshfaraz R, Noruzi R, Ebadzadeh P, (2022). Experimental Investigation of non-suppressed sill effect with different geometry on flow pattern and discharge coefficient of sluice. Journal of Hydraulics, 17(3): 47-63.
12. Abdelmonem YK, Shabayek S, Khairy AO, (2018). Energy dissipation downstream sluice gate using a pendulum sill. Alexandria engineering journal, 57(4): 3977-3983.
13. Habibzadeh, A., Rajaratnam, N., & Loewen, M. (2019, August). Characteristics of the flow field downstream of free and submerged hydraulic jumps. In *Proceedings of the Institution of Civil Engineers-Water Management* (Vol. 172, No. 4, pp. 180-194). Thomas Telford Ltd.
14. Abbaszadeh H, Daneshfaraz R, Norouzi, R, (2023). Experimental Investigation of Hydraulic Jump Parameters in Sill Application Mode with Various Synthesis. Journal of Hydraulic Structures, 9(1): 18-42.
15. Abbaszadeh H, Norouzi R, Sume V, Kuriqi A, Daneshfaraz R, Abraham J, (2023). Sill role effect on the flow characteristics (experimental and regression model analytical). Fluids, 8(8): 235.
16. Xin G, Zhang J, Fan L, Deng B, Bu W, (2023). Numerical Simulations and Wind Tunnel Experiments to Optimize the Parameters of the Second Sand Fence and Prevent Sand Accumulation on the Subgrade of a Desert Railway. Sustainability, 15(17): 12761.
17. Daneshfaraz R, Norouzi R, Ebadzadeh P, Kuriqi A, (2023). Influence of sill integration in labyrinth sluice gate hydraulic performance. Innovative Infrastructure Solutions, 8(4): 118.

© 2024 by the authors. Licensee SCU, Ahvaz, Iran. This article is an open access article distributed under the terms and conditions of the Creative Commons Attribution 4.0 International (CC BY 4.0 license) (http://creativecommons.org/licenses/by/4.0/).

Journal of Hydraulic Structures
J. Hydraul. Struct., 2024;10(2):55-61
DOI: 10.22055/JHS.2024.19042



OPEN ACCESS

Reducing the extent of vortices upstream of the sliding valve

Parisa Ebadzadeh [*1]
Hamidreza Abbaszadeh [2]
Rasoul Daneshfaraz [1]
Reza Norouzi [1]

Abstract

The purpose of this research is to provide a solution to eliminate the vortices formed upstream of the sliding valve. The effect of the threshold with the geometric shapes of semi-cylinder, cylinder, pyramid and rectangular cube in different widths of 5, 7, 10, 15 and 20 cm under the sliding valve was investigated experimentally. The results of this research showed that the entry of air into the fluid leads to the formation of the vortex phenomenon in the flow profile due to the water absorption of the slide valve from the surface layers. The conservation of angular momentum at the opening of the valve causes the combination of vertical and horizontal components of the velocity near the sliding valve. The results showed that placing the threshold under the horizontal sliding valve increases the horizontal velocity of the flow. Therefore, it turns the vortex with a larger diameter into end-line vortices. Due to the insignificant effect of threshold shape on vortices, its effect was ignored.

Keywords: Sliding Valve, Vortices, Threshold, Discharge Coefficient.

Received: 09 November 2023; Accepted: 16 April 2024

1. Introduction

Flow control and measurement in rivers and channels need more studies. Flow control structures include weirs and valves. The design and construction of these structures requires new and more practical methods. The control of water resources in the first stage is the cause of this issue. Sliding valves are one of the most important hydraulic structures that are used to control and measure the flow. The ease of installation and implementation has drawn the attention of researchers to this structure. Various hydraulic issues including discharge coefficient, energy dissipation, flow pattern have been studied by researchers. In the following, the research conducted on sliding valves has been discussed. The use of a threshold valve is one of the new structures to control the flow rate. The effect of this additional structure on energy consumption caused by hydraulic jump has been confirmed in several researches.

[*] E-mail: ebadzadeh.p@maragheh.ac.ir (**Corresponding Author**)
[1] Department of Civil Engineering, Faculty of Engineering, University of Maragheh, Maragheh, Iran.
[2] Department of Civil Engineering, Faculty of Civil Engineering, University of Tabriz, Tabriz, Iran.

Hydraulic parameters in the control structure of sliding valves in free and submerged conditions have been of interest to researchers Silva [1]. The deviation in the placement angle of the sliding valve and the use of inclined valves are among the factors affecting the discharge coefficient of this structure Shesha Prakash and Shivapure [2]. The increase in flow coefficient of inclined valves compared to vertical valves was one of the results of this research.

Daneshfaraz et al. [3] investigated the effect of the deviation angle of the sliding valve on the discharge coefficient by using the finite volume method. Increasing the angle of deviation of the sliding valve towards the upstream side increased the discharge coefficient. Investigating energy dissipation is one of the other topics on sliding valves (Abbaszadeh et al., [4]). The results showed that the use of threshold affects the characteristics of hydraulic jump.

Heidari et al [5] described the discharge coefficient without a threshold as the amount of opening of the valve and the depth of the upstream water. In this research, the parameters of height and shape of threshold were stated among the influencing factors on the discharge coefficient in the state with threshold. The effect of non-suppressed thresholds under the sliding valve on the discharge coefficient was investigated in a experimental study (Daneshfaraz et al., [6,7,8,9]). Several researches have been done on the hydraulics of sliding valves. This makes the study of this structure more important for engineers [10-16]

Vortices as a negative factor in the flow profile cause damage to the structure in a long period of time. A solution to reduce the formation of vortices has been presented in the research of Roth and Hager [17]. Their experiments were performed in a converging rectangular channel. In this research, 3 vertical anti-vortex plates with different geometries were installed upstream of the valve. As a result, the vortices were classified into 6 types. In this research, the shock waves generated at downstream were reduced by 50%. The research of Yousefian [18] is another research in this field. The opening of the sliding valve is an important parameter for the formation of vortices. In an experimental research, Norouzi et al investigated the strength of vortices. The results of this research showed that the use of the cylinder causes a decrease in the strength of the vortice Norouzi et al., [19].

The review of previous studies confirms the importance of basic design of hydraulic structures [20,21,22]. Also, there is a research gap in the field of the vortex behind the valve .It is felt to adopt a new method to increase the performance of this structure. The design of the threshold under the sliding valve as an anti-vortex element is the main goal of this research. The use of a sliding valve with a threshold has completely eliminated the eddies.

2. Materials and Methods

In the present study, a laboratory flume with a length of 5 meters, a height of 0.5 meters and a width of 0.3 meters was used. In order to create supercritical flow, a vertical valve with an opening of 4 cm was used, which was placed at a distance of 1.5 meters from the inlet tank. The flow entering the flume was pumped by two pumps with a capacity of 450 liters per minute. The current research was investigated with 4 different geometry models, which include semi-cylindrical, cylindrical, pyramidal and rectangular cube geometries. All four sills were prepared in widths of 5, 7.5, 10, 15 and 20 cm in order to study the effect of sill width on the vortices under the valve, Figure (1).

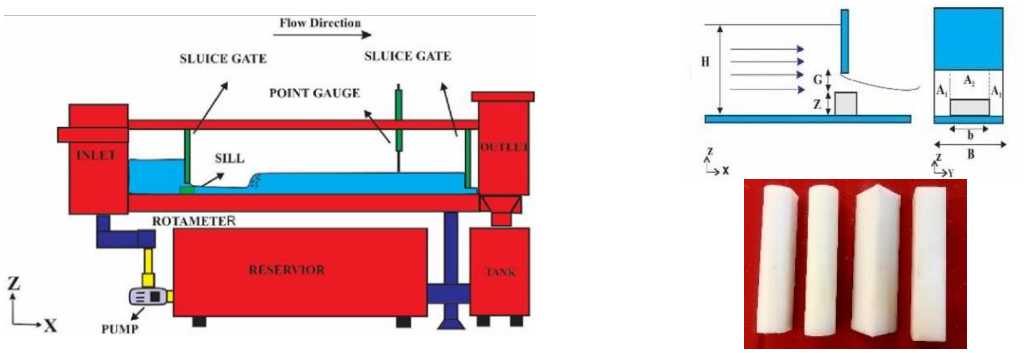


Figure 1. Schematic view of the flume and threshold used in this study

3. Results and Discussion

Changes in water depth upstream of the sliding valve were investigated using threshold and control. The figure 2 shows the percentage of upstream water depth of the sliding valve with the threshold and in the control state.

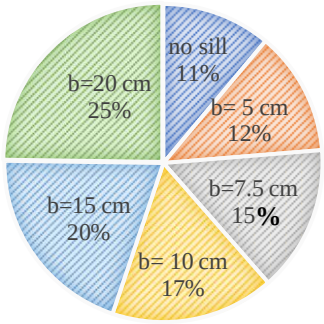


Figure 2. Upstream flow depths of sliding valve

In the present research, the changes of hydraulic parameters were investigated with the use of threshold. Therefore, in Figure (3), the effect of the threshold on different parameters has been investigated and the results have been compared with the control state.

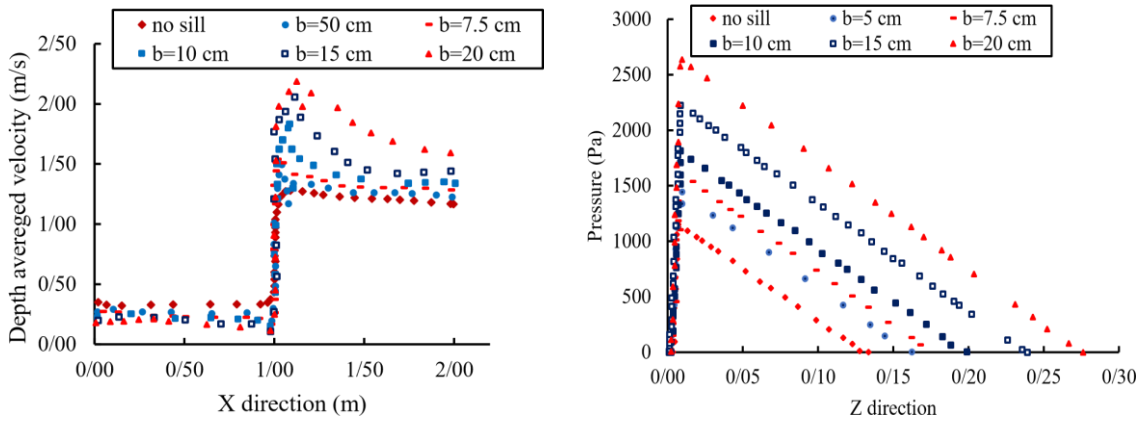
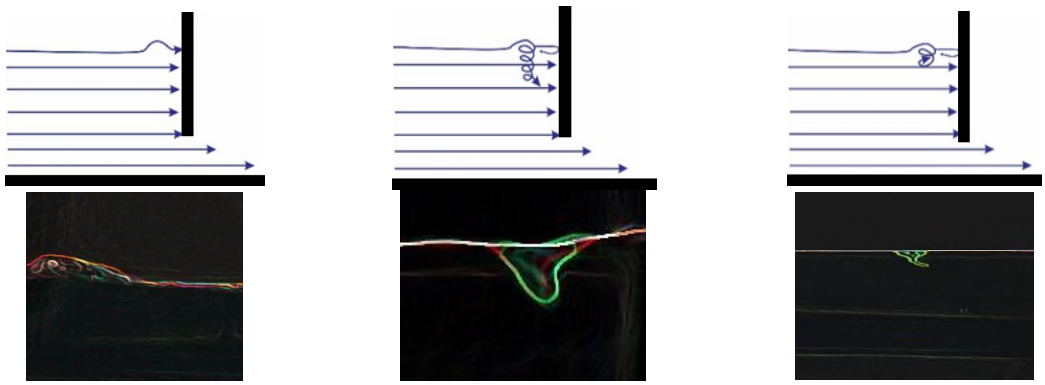


Figure 3. Velocity and pressure changes in sliding valve

3.1. Investigating the causes and methods of vortex formation

In this research, the extent of vortices was investigated. The results of this research were compared with previous studies. In the following, the formation of vortices is discussed. These are experimental figures. Their schematic state is also shown. The repeated period of vortex formation was observed throughout the experiments. Figure (4-a) shows the turbulence of the upstream flow before the formation of the vortex. vortex is formed when air enters the fluid (4-b) and finally, after the balance between the air inside the vortex and the fluid, it gradually disappears (4-c).



(a) **(b)** **(c)**

Figure 4. Stages of vortex formation

In order to investigate the effect of the threshold on the vortices, the threshold with different geometry and widths was installed under the sliding valve. Due to the very slight changes in the appearance of the vortices in the threshold with different geometries, the effect of the geometry of the threshold on the vortices was ignored. Therefore, the vortices created in this research were divided into 4 categories according to their appearance (Figure 5).

The first category is related to the sliding valve without a threshold. In this case, the turbulence in the flow surface after hitting the valve can be clearly seen. Due to the larger opening of the sliding valve, the flow rate is low and as a result, the suction of the sliding valve is significant. The presence of a flow with high suction causes a decrease in the pressure on the surface of the flow. The low flow speed in this case causes significant penetration of air into the flow. Therefore, the formation of vortices with larger diameters was observed in this case.

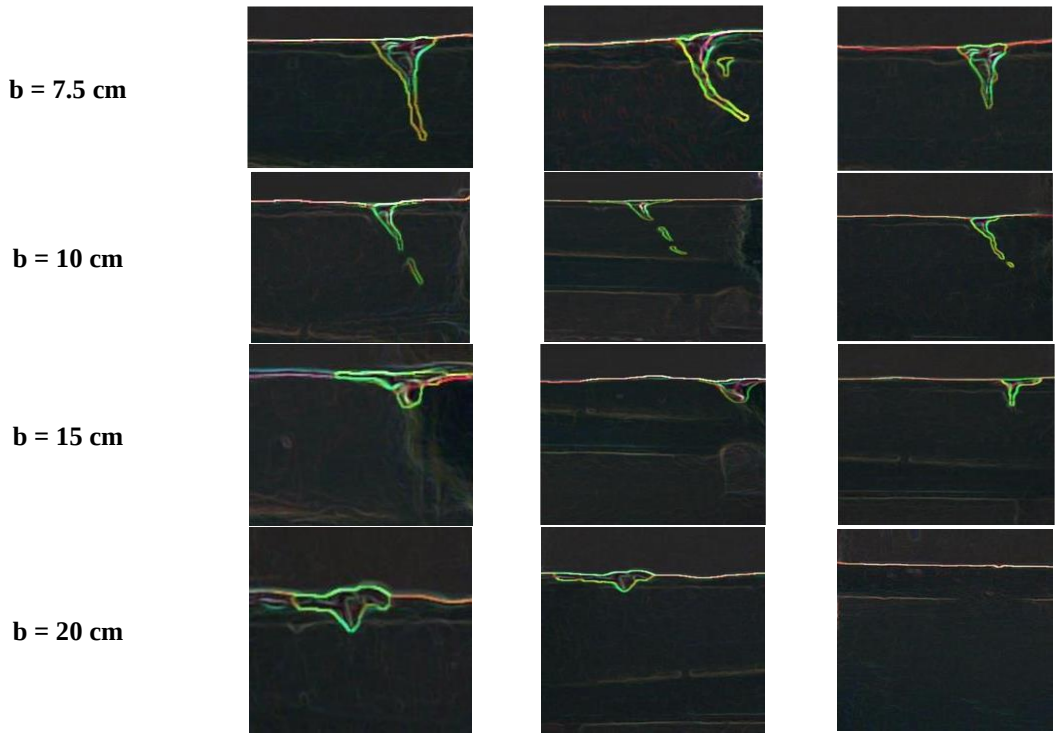


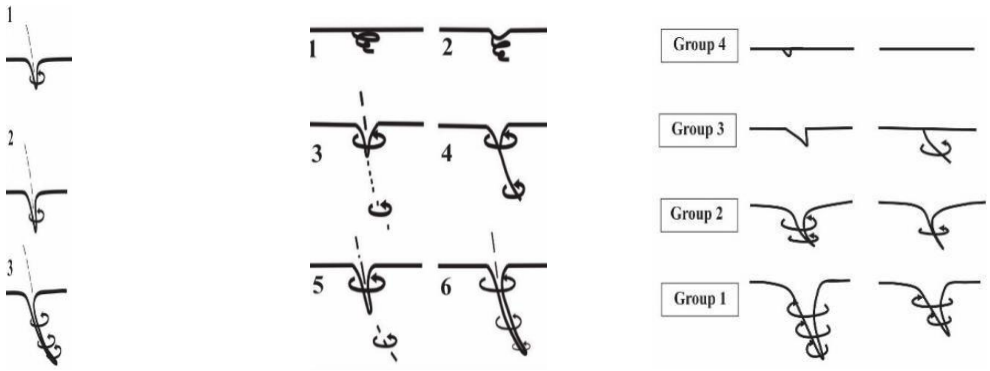
Figure 5. Classification of vortices in the present study

In the case of using a threshold with a width of 7.5 cm, vortices with a large diameter changed into vortices with a linear end. In this case, with the increase in the speed of the flow passing through the sliding valve, the horizontal speed prevailed over the flow and caused a large deviation of the end of the vortex towards the opening of the sliding valve.

In the second category, a threshold with a width of 10 cm was examined. The type of vortices formed upstream of the sliding valve was significantly changed with this threshold. Trailing vortices in the second category were gradually removed from the flow profile. Then, by placing a threshold with a width of 15 cm, the power of air penetration into the water decreased.

The use of threshold, with a larger width (b=20 cm), increasing the discharge, caused a significant increase in the water depth upstream of the sliding valve. As a result of the increase in pressure upstream of the slide valve, it led to the reduction of turbulence between water and air. Therefore, the formation of vortices decreased until the formation of vortices stopped at high flow rates. Designing new structures for hydraulic problems is of particular importance in solving engineering problems. The application of the additional structure of the sliding valve with the flange caused a reduction in the presence of vortices in the flow profile. The results showed that the use of this structure by changing the flow characteristics including depth, velocity and pressure has a positive effect on the flow profile. Because it caused the complete removal of the vortex phenomenon from the flow pattern.

In Yousefian's research, the opening of the sliding valve was the most important factor in the appearance of vortices. In Ross and Heger's research, the installation of anti-vortex plates decreased the extent of vortices. Previous studies have been done with the aim of reducing the strength of vortices. In this research, the strength of the vortices was reduced by using the threshold. Finally, with the increase in the inlet flow rate and the width of the threshold, no vortices were formed at high flow rates Figure 6.



Yousefian **Roth and Hager** **This study**

Figure 6. Comparing the extent of vortices in different researches

4. Conclusion

The present research was conducted in order to investigate the vortices formed upstream of the sliding valve along with the flow coefficient. For this purpose, the effect of the threshold in cylindrical, semi-cylindrical, pyramidal and rectangular cube geometries with widths of 5, 7.5, 10, 15 and 20 cm under the drawer was investigated experimentally. The results showed that the low water depth in the control state causes the valve to draw water from the surface layers of the flow. The opening of the sliding valve and the velocity of flow were introduced as the influencing factors on the formation of vortices. The decrease in the opening of the sliding valve by using the threshold caused an increase in the flow depth upstream of the sliding valve. Therefore, water extraction was done from the lower layers. Also, the decrease in the valve opening parameter increased the flow rate. The results showed that vortices with a larger diameter were removed from the flow profile and the strength of the vortices was reduced.

References

1. Silva, C. O., & Rijo, M. (2017). Flow rate measurements under sluice gates. Journal of Irrigation and Drainage Engineering, 143(6), 06017001.
2. Shivapur AV, Shesha Prakash MN, “Inclined sluice gate for flow measurement”, ISH Journal of Hydraulic Engineering, 2005, 11 (1), 46-56.
3. Daneshfaraz R, Abbaszadeh H, Gorbanvatan P, Abdi M, “Application of S luice gate in different positions and its effect on hydraulic parameters in free flow condition”, Hydraulic structures, 2021, 7 (3), 72-87. 10.22055/JHS.2022.39208.1196
4. Abbaszadeh H, Norouzi R, Sume V, Kuriqi A, Daneshfaraz R, Abraham J, “Sill role effect on the flow characteristics (Experimental and Regression Model Analytical)”, Fluids, 2023, 8 (8), 235. https://doi.org/10.3390/fluids8080235

5. Heidari M, Karami S, Adibrad M, "Investigation of free flow under the radial gate with the sill", Civil and Environmental Engineering, 2020, 50 (3) (100), 9-19. https://doi.org/10.22034/jcee.2020.23384.1568.
6. Daneshfaraz R, Norouzi R, Abbaszadeh H, Azamathulla HM, (2022). Theoretical and experimental analysis of applicability of sill with different widths on the gate discharge coefficients. Water Supply, 22(10): 7767-7781.
7. Daneshfaraz R, Norouzi R, Abbaszadeh H, Kuriqi A, Di Francesco S, (2022). Influence of sill on the hydraulic regime in sluice gates: an experimental and numerical analysis. Fluids, 7(7): 244.
8. Daneshfaraz R, Norouzi R, Ebadzadeh P, (2022). Experimental and numerical study of sluice gate flow pattern with non-suppressed sill and its effect on discharge coefficient in free-flow conditions. Journal of Hydraulic Structures, 8(1): 1-20
9. Daneshfaraz R, Noruzi R, Ebadzadeh P, (2022). Experimental Investigation of non-suppressed sill effect with different geometry on flow pattern and discharge coefficient of sluice. Journal of Hydraulics, 17(3): 47-63.
10. Hassanzadeh Y, Abbaszadeh H, (2023). Investigating Discharge Coefficient of Slide Gate-Sill Combination Using Expert Soft Computing Models. Journal of Hydraulic Structures, 9(1): 63-80.
11. Daneshfaraz R, Abbaszadeh H, Gorbanvatan P, Abdi M, (2021). Application of sluice gate in different positions and its effect on hydraulic parameters in free-flow conditions. Journal of Hydraulic Structures, 7(3): 72-87.
12. Daneshfaraz R, Norouzi R, Ebadzadeh P, Di Francesco S, Abraham JP, (2023). Experimental study of geometric shape and size of sill effects on the hydraulic performance of sluice gates. Water, 15(2): 314.
13. Ferro, V. (2000). Simultaneous Flow over and under a gate. Irrigation and Drainage engineering, 190-193.
14. Kim, D. G. (2007). Numerical analysis of free flow past a sluice gate. KSCE Journal of Civil Engineering, 11, 127-132.
15. Daneshfaraz, R., Norouzi, R., Ebadzadeh, P., & Kuriqi, A. (2023). Influence of sill integration in labyrinth sluice gate hydraulic performance. Innovative Infrastructure Solutions, 8(4), 118.
16. Abbaszadeh H, Daneshfaraz R, Norouzi, R, (2023). Experimental Investigation of Hydraulic Jump Parameters in Sill Application Mode with Various Synthesis. Journal of Hydraulic Structures, 9(1): 18-42.
17. Roth, A., & Hager, W. H. (1999). Underflow of standard sluice gate. Experiments in fluids, 27(4), 339-350.
18. Yousefian, M. (2007). Flow through the sluice gate in rectangular channels with different widths. isfahan University of Technology .
19. Norouzi R, Ebadzadeh P, Sume V, Daneshfaraz R, (2023). Upstream vortices of a sluice gate: An experimental and numerical study. AQUA—Water Infrastructure, Ecosystems and Society, 72(10): 1906-1919.

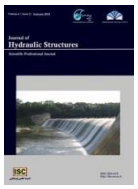
20. Daneshfaraz, R., Norouzi, R., Patrick Abraham, J., Ebadzadeh, P., Akhondi, B., & Abar, M. (2023). Determination of flow characteristics over sharp-crested triangular plan form weirs using numerical simulation. Water Science, 37(1), 211-224.
21. Ebadzadeh, P., Daneshfaraz, R., & Norouzi, R. (2024). Energy Dissipation of Supercritical Flow with Use of Different Geometric Shapes of Sills. Water and Soil Science.
22. Daneshfaraz, R., Norouzi, R., & Ebadzadeh, P. (2023). Evaluation Effect of Changing the Sill Geometries and Positions on Discharge Coefficient of Vertical Sluice Gate. Journal of Civil and Environmental Engineering, 53.3(112), 117-127. doi: 10.22034/jcee.2022.52525.2167



© 2024 by the authors. Licensee SCU, Ahvaz, Iran. This article is an open access article distributed under the terms and conditions of the Creative Commons Attribution 4.0 International (CC BY 4.0 license) (http://creativecommons.org/licenses/by/4.0/).



Journal of Hydraulic Structures
J. Hydraul. Struct., 2024; 10(1): 62-71
DOI: 10.22055/jhs.2024.19073



OPEN ACCESS

Determining Thermal Stratification of Zayandeh Roud Dam Reservoirs Using Two-Dimensional CE-QUAL-W2 Model

Negar Varshabi [1]
Ramtin Moeini [*1]

Abstract

Dam reservoirs, serving as critical repositories of water resources, play an important role for satisfying water demands. However, the pollution of various sources poses significant challenges to the preservation of water quality of these reservoirs. Here, effective management of these resources is necessary. For this purpose, the modeling and simulation of dam reservoirs should be done investigating the impact of pollution. This study focuses on the Zayandeh Roud Dam reservoir in Isfahan province, using historical data from 2016 to 2021. Here, the CEQUAL-W2 model is used for simulation and determining the temperature of water stored in reservoir and release from the dam. Calibration and verification process of model are done for the periods 2016 to 2020 and 2021, respectively. The simulation results show that absolute mean error (AME) of the water temperature release the reservoir are 0.80 degrees Celsius for calibration and 1.16 degrees Celsius for validation process. The results highlighted the performance of advanced modeling approaches, the CEQUAL-W2 model, for the proper management of dam reservoirs.

Keywords: Qualitative Simulation, Thermal Layering, Zayandeh Roud Dam, CE-QUAL-W2 Model

Received: 09 November 2023; Accepted: 16 April 2024

1. Introduction

These days, dam reservoirs serve as fundamental repositories of surface water for satisfying different demand including agriculture, drinking water, industrial processes, and hydropower. Consequently, different challenges and concerns are arisen when this resource is polluted or restricted effective for management of water resources. In general, dam reservoirs, as vital components of surface water sources, are constructed and operated for different quantitative and qualitative goals.

[1] Department of Civil Engineering, Faculty of Civil Engineering and Transportation, University of Isfahan, Isfahan, Iran.
[*] Email: r.moeini@eng.ui.ac.ir **(Corresponding author)**

To achieve these objectives, qualitative simulations of reservoirs should be done to identify the key parameters influencing the simulation process. Various methods and models have been proposed for qualitative simulation of dam reservoirs, in which each of them unique advantages and disadvantages. Among these models, the CE-QUAL-W2 model is widespread used and attended by researchers due to its unique capabilities.

Reviewing the researches shown that numerous studies have been done in this field. For example, Ma et al. [1] investigated the thermal layering for the Koris Dam reservoir in Cyprus using the two-dimensional model CE-QUAL-W2. The reservoir has been thermally stratified throughout the year, and mixed occurs in early February to initiate the mixing in the reservoir.

Çalışkan and Elçi [2] proposed a selective withdrawal method to regulate the temperature of the water released from the dam reservoir. Here, effects of selective harvesting on the hydrodynamics of reservoir layering numerical modeling and sensitivity analysis were investigated. By Using the Environmental Fluid Dynamics Code (EFDC) hydrodynamic model, the effects of selective withdrawal from the four outlet located along the water intake structure of Tahtali Reservoir in Turkey on water temperature and analyzed the impacts of thermal stratification structure were investigated. Withdrawal of the water at the bottom outlet was found to be the most effective choice encouraging the mixing of the water column and finally reducing anoxia.

Afshar et al. [3] used the Particle Swarm Optimization algorithm to automatically calibrate temperature simulation models within the CE-QUAL-W2 model. This model was used to simulate temperature variations in the Karkheh Dam reservoir. Parameters such as solar radiation absorbed in surface layer (BETA), extinction coefficient for pure water (EXH2O), and wind sheltering coefficients (WSC) were selected as effective parameters in temperature calibration process.

Mohammadnejad et al. [4] simulated the trophic state of the Mahabad Dam reservoir using the CE-QUAL-W2 model. Subsequently, the model was calibrated and validated based on the temperature and quality parameters, including nitrate, phosphate, total phosphorus, and total nitrogen. Furthermore, the analysis of the results revealed that nutrient distribution and adverse conditions play a dominant role in the Mahabad Dam reservoir. These factors limit phosphorus availability within the reservoir. Additionally, the reservoir profile analysis indicates the presence of summer thermal stratification.

Aboutalebi et al. [5] used the two-dimensional CE-QUAL-W2 simulation model to simulate the concentration of pollution in the Karaj river-reservoir system. In this study, support vector regression (SVR) and artificial neural network (ANN) data-driven models were used to address the time-consuming issue associated with the CE-QUAL-W2 simulator model. Finally, the Support Vector Regression (SVR) and Artificial Neural Network (ANN) models were integrated using a genetic algorithm (GA) optimization method. The results indicated that the performance of the SVR model outperformed the artificial neural network model.

Ziaie et al. [6] used the two-dimensional model CE-QUAL-W2 to simulate temperature and quality parameters for the reservoir of the Zayandeh Roud Dam. In this research, the parameters and coefficients selected for model calibration included temperature and quality parameters such as total coliform, nitrate, dissolved oxygen. Furthermore, the water quality of the reservoir was assessed using the IRWQISC index. The results indicated that the reservoir's water quality is good and relatively high.

Arefinia et al. [7] used a statistical approach to investigate water pollution patterns in the reservoirs. In this research, temperature and nitrate parameters of the Amirkabir Dam reservoir were simulated using the CE-QUAL-W2 model. Subsequently, input data of the genetic programming (GP) methods, artificial neural networks, and support vector machines (SVM) were constructed for reservoir quality modeling using the CE-QUAL-W2 hydrodynamic simulator model.

Rasouli et al. [8] investigated the thermal layering and water quality of the Glaber Dam reservoir located in Zanjan. For this purpose, the two-dimensional CE-QUAL-W2 model was used to simulate hydrodynamics, dissolved oxygen, and total dissolved solids for the one-year period from 2014 to 2015. The simulation results showed summer thermal stratification. In addition, the water quality in different parts of the reservoir at different times was evaluated using Iran's water quality index.

Hanjaniamin et al. [9] used the CE-QUAL-W2 model to investigate the water quality of the Yamchi Dam reservoir located in Ardabil province. The CE-QUAL-W2 model was used for simulating and determining the concentration of dissolved oxygen for this purpose. The results showed that the Yamchi Dam reservoir is one of the eutrophic reservoirs, and practical solutions should be implemented to improve these conditions.

In general, the CE-QUAL-W2 model was used by considering quality parameters such as temperature, nitrate, dissolved oxygen, etc., to investigate water quality in dam reservoirs. Reviewing the researches shows the good performance of the CE-QUAL-W2 model in simulating quality parameters of dam reservoirs. In this research, Zayandeh Roud Dam reservoir is selected as a case study. Here, the CE-QUAL-W2 model is used to simulate the temperature for water stored in the dam reservoir as the desired qualitative parameter. A comparison of results shows the good performance of the model for determining the temperature and characterizing the thermal stratification of water stored in the dam reservoir.

2. Simulation Model

The CE-QUAL-W2 simulation model is a versatile and widely used tool in the domain of trophic modeling and thermal stratification assessment of dam reservoirs. This longitudinal-depth, hydrodynamic (unsteady), and water quality model is demonstrated success across various water bodies worldwide, ranging from steep rivers to big reservoirs. By using a two-dimensional approach and finite difference solution method, the CE-QUAL-W2 model is particularly well-suited for portraying qualitative parameters through vertical and longitudinal profiles, in which it is highly effective for relatively lengthy reservoirs and lakes.

The most important capabilities of the CE-QUAL-W2 model is hydrodynamic modeling of rivers and reservoirs, temperature simulation, water quality modeling, and nutrient analysis. The model requires a set of input files including tank geometry, meteorological data, water inflow discharge, water inflow temperature and water release from reservoir, shade coverage, wind protection, and a control file. Through meticulous calibration of quality parameters based on input data, the CE-QUAL-W2 model shows exceptional accuracy in dam reservoirs simulation. In this research, the performance of CE-QUAL-W2 simulation model is investigated, highlighting its applications, methodologies, and notable features in the context of managing dam reservoirs. The model's robust capabilities are valuable asset for researchers and insightful simulations for effective reservoir management.

3. Case Study

In recent decades, the instability of water resources is a significant challenge in the Zayandeh Roud watershed. Therefore, a comprehensive analysis and investigation of the challenges within this watershed are imperative. For this purpose, the Zayandeh Roud catchment basin and the dam constructed on the Zayandeh Roud River within this basin, is selected as a case study.

The volume of Zayandeh Roud Dam Lake, is 1470 MCM with the area of approximately 54 KM^2. In addition, the elevation is 2063 meter above the sea level in the eastern part of the Western Zagros mountain range. This reservoir was constructed in 1970 multiple purposes, including the generation of hydroelectric energy, mitigation of seasonal floods, regulation of agricultural water supply, and provision of water for industrial demands in Isfahan. Figure 1 illustrates the geographical location of the Zayandeh Roud Dam reservoir.

In this research, the data necessary for simulating the Zayandeh Roud Dam reservoir, from September 2016 to September 2021, were collected. For this purpose, meteorological information from the Chadegan synoptic station, encompassing air temperature, wind speed, dew point, and etc. were collected. In addition, the dataset for the Zayandeh Roud Dam reservoir incorporates water inflow and release values, along with the temperature of water inflow in to the reservoir. These parameters serve as crucial boundary conditions for our simulation model. The daily average air temperature, wind speed, water inflow and release values from reservoir, and water temperature of inflow values are presented in figures 2, 3 and 4.

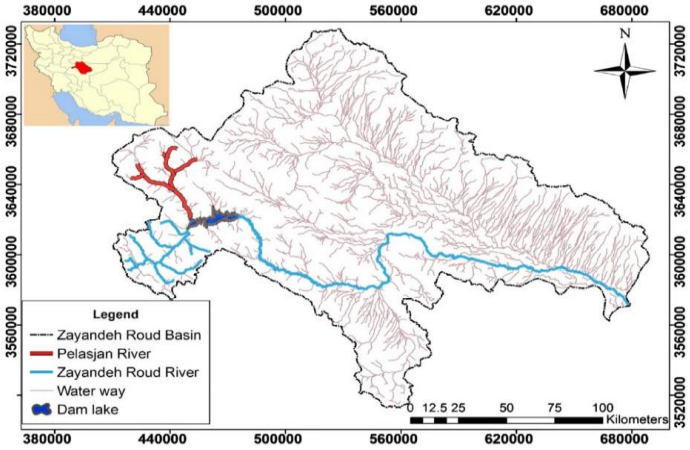


Figure 1. Location of the Zayandeh Roud Dam [6]

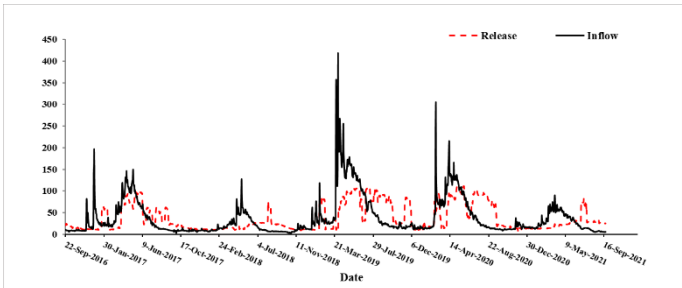


Figure 2. Water Inflow and release from reservoir values

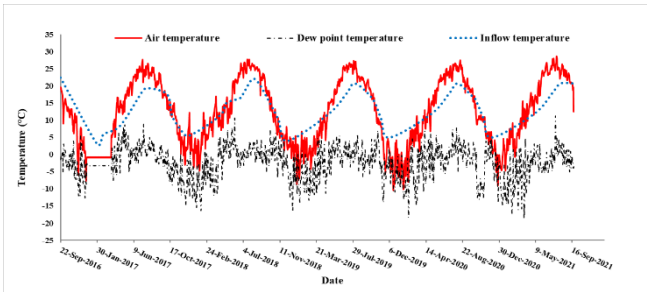


Figure 3. Inflow temperature, air temperature, and dew point temperature values

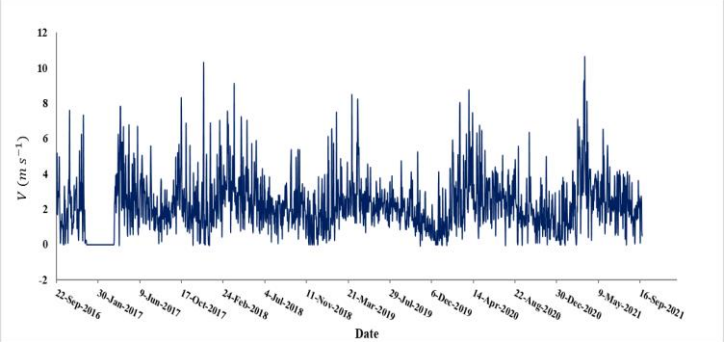


Figure 4. Wind speed values

4. Results and Discussion

In this research, the CE-QUAL-W2 model is used to determine the thermal layering of the Zayandeh Roud Dam reservoir during the water year period from 2016 to 2021. In this model, the initial step for simulating various natural parameters involves calibrating the model with regard to effective parameters. This calibration process aims to fine-tune the model for the specific conditions governing the study area. The final goal is to obtain the accurate coefficients within the model to yield optimal results when compared to observational data. The calibration of the CE-QUAL-W2 model can be done both manually and automatically, encompassing multiple stages such as tank geometry, water level, and water temperature. Each stage is systematically presented as follow. The geometry error of the dam reservoir and the water level error during the calibration stages are presented in table 1 and 2, respectively. Moreover, comparisons the model segmentation and vertical view of the Zayandeh Roud Dam reservoir are presented in Figure 5 and 6. The results of Tables 1 and 2 highlight the remarkable accuracy achieved by the model during the calibration process of the dam reservoir geometry.

Statistical parameters of absolute mean error (AME) and root mean square error (RMSE), presented in Eqs. (1) and (2), were calculated to compare the simulated and observed data

$$AME = \frac{|P - O|}{N} \quad (1)$$

$$RMSE = \sqrt{\frac{\sum(P-O)^2}{N}} \quad (2)$$

Where, P = predicted (simulated) data; O = observed data; and N = number of observations.

Table 1. Geometry Errors of the Zayandeh Roud Dam Reservoir for calibration and validation process

RMSE (MCM)	AME (MCM)
6.19	5.73

Table 2. Water Level Errors for Zayandeh Roud Dam Reservoir

Calibration process (Meters)		Validation process (Meters)	
RMSE	AME	RMSE	AME
0.28	0.24	0.21	0.15

By doing the calibration and validation process for the reservoir geometry, the results of both the reservoir geometry and water level are ready for the subsequent modeling process leading to water temperature of the dam reservoir. In the temperature calibration and validation process, the parameters affecting the temperature are initially identified using sensitivity analysis. Subsequently, by comparative analysis of simulated and observed temperatures, adjustments are made to the parameters, for optimal alignment between the model results and observed data.

In this research, calibration process is done from 2016 to 2020, and the validation process is done for 2021. The water validation is done for three monitoring stations including Segment 33, Segment 26 and Segment 22. The model's results are presented at these strategically chosen monitoring points and compered with observed data. Figures 7 to 12 show the obtained water temperature results, in comparison with observed data, during both the calibration and validation process. In addition, the RMSE and AME values for temperature for the specified points during simulation period are presented in table 3. The results show the unique performance of the model for accurate simulation of the stored water temperature of the Zayandeh Roud Dam reservoir.

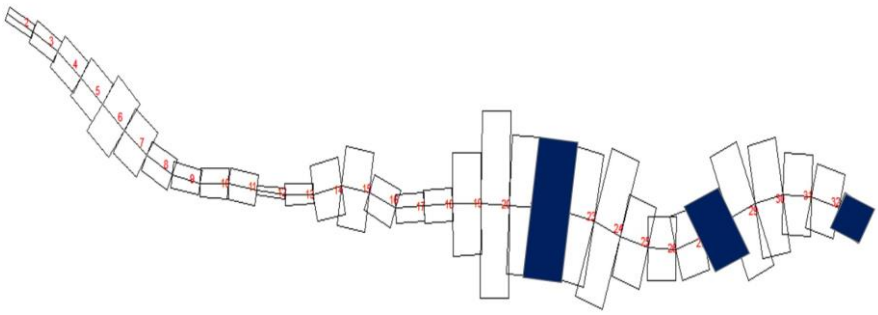


Figure 5. Zayandeh Roud Reservoir model segmentation and location of monitoring stations

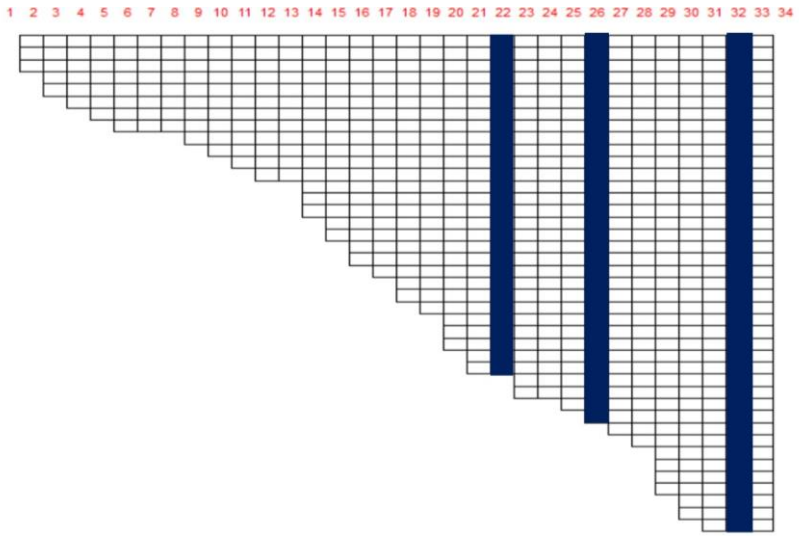


Figure 6. Vertical view of Zayandeh Roud Reservoir for monitoring stations (Dark shades monitoring station)

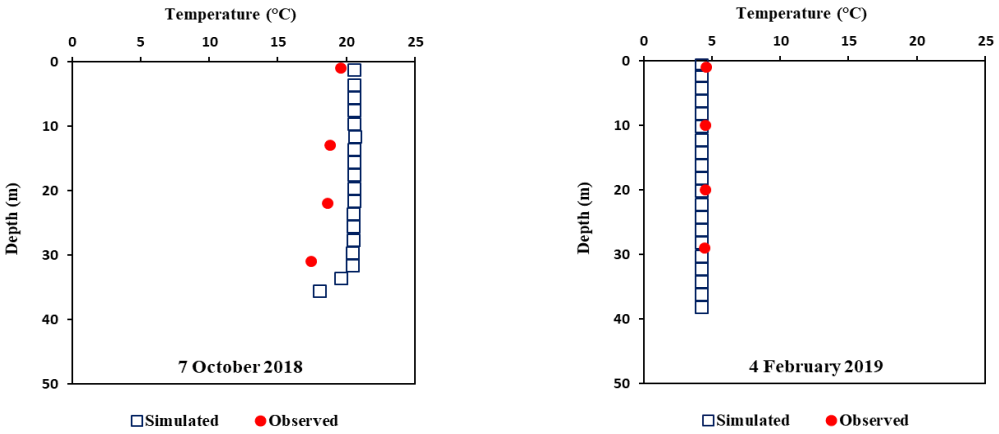


Figure 7. Results of water temperature calibration process (Segment 33)

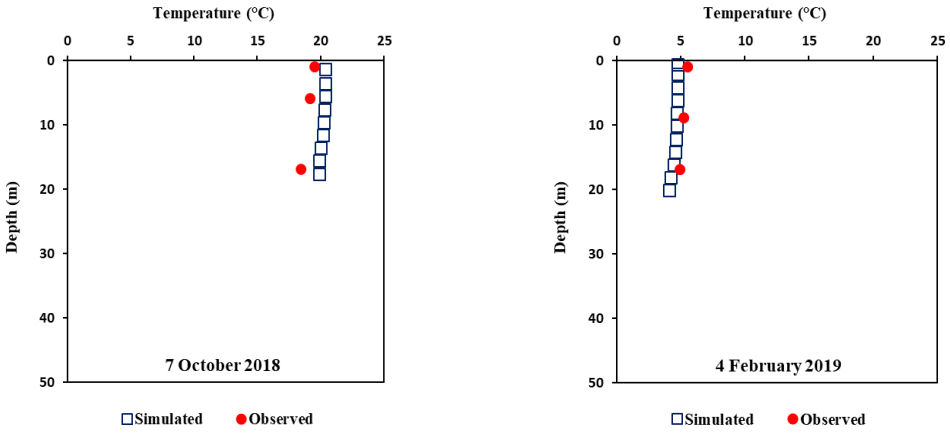


Figure 8. Results of water temperature calibration process (Segment 26)

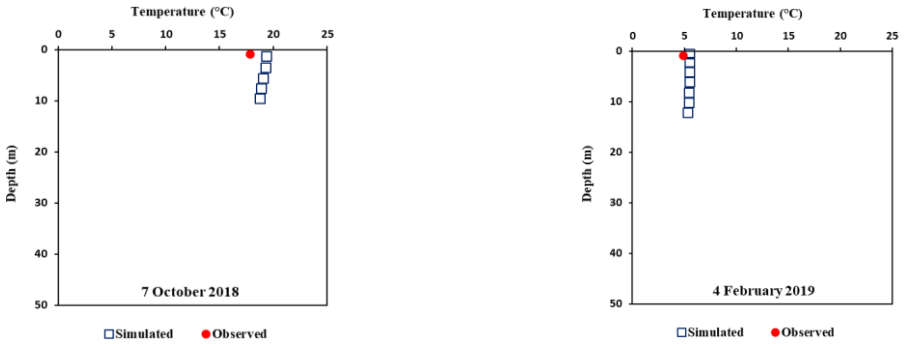


Figure 9. Results of water temperature calibration process (Segment 22)

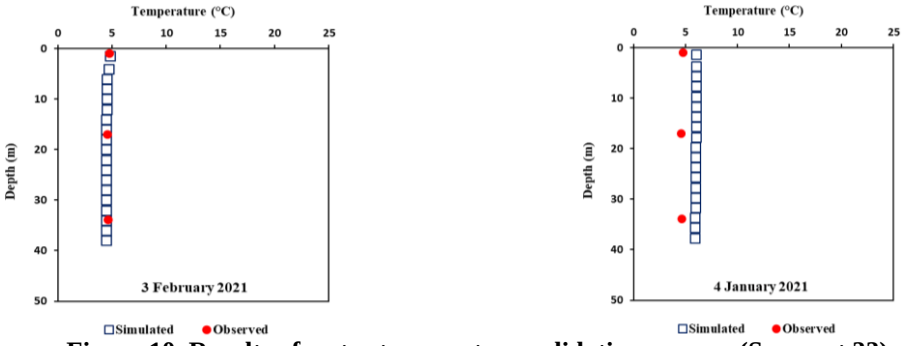


Figure 10. Results of water temperature validation process (Segment 33)

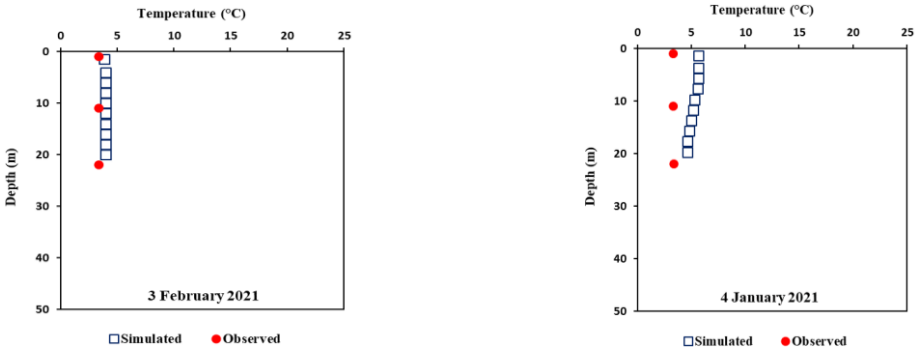


Figure 11. Results of water temperature validation process (Segment 26)

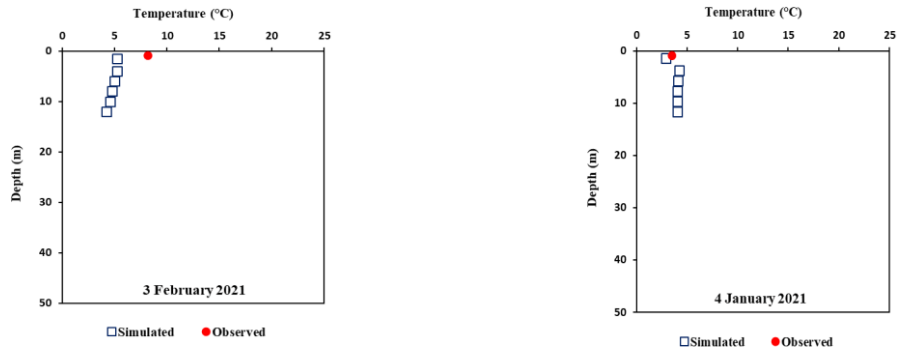


Figure 12. Results of water temperature validation process (Segment 22)

Table 3. RMSE and AME values of Water Temperature of the Zayandeh Roud Dam Reservoir for the Period 2016-2021

Date	location of monitoring stations	AME(℃)	$RMSE$ (℃)
05/March/2017	Segment 33	0.39	0.48
	Segment 26	0.58	0.60
	Segment 22	0.82	0.82
05/January/2018	Segment 33	0.63	0.66
	Segment 26	0.11	0.11
	Segment 22	1.15	1.15
04/April/2018	Segment 33	1.12	1.17
	Segment 26	1.38	1.45
	Segment 22	0.88	0.88
06/July/2018	Segment 33	0.56	0.56
	Segment 26	0.00	0.00
	Segment 22	0.76	0.76
07/October/2018	Segment 33	1.85	1.96
	Segment 26	1.12	1.15
	Segment 22	1.47	1.47
04/February/2019	Segment 33	0.34	0.34
	Segment 26	0.71	0.72
	Segment 22	0.56	0.56
06/October/2020	Segment 33	0.69	0.59
	Segment 26	0.83	1.01
	Segment 22	1.64	1.64
04/January/2021	Segment 33	1.28	1.28
	Segment 26	2.03	2.05
	Segment 22	0.43	0.43
03/February/2021	Segment 33	0.15	0.16
	Segment 26	0.55	0.55
	Segment 22	2.91	2.91

5. Conclusion

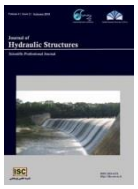
In this research, the CE-QUAL-W2 model was used to simulate and determine the temperature of water released and thermal validation of the Zayandeh Roud Dam reservoir during the period from 2016 to 2021. For this purpose, the data from 2016 to 2020 were used for calibration and the year 2019 for validation process. Here, at first the dam reservoir geometry calibration process was done leading to RMSE values of 6.19 million cubic meters for reservoir volume and 0.28 meters for water surface elevation. Then, the results of water temperature simulation were compared with observed data at three monitoring stations including Segment 33, Segment 26 and Segment 22. A compression of the results indicated the unique performance of the model in simulating reservoir water temperature. In other words, the average error of temperature of water released from the reservoir during the calibration and validation periods were 0.80 and 1.16 degrees of Celsius, respectively.

References

1. Ma, S., Kassinos, S. C., Fatta Kassinos, D., & Akylas, E. (2008). Effects of selective water withdrawal schemes on thermal stratification in Kouris Dam in Cyprus. Lakes & Reservoirs: Research & Management, 13(1), 51-61. Çalışkan, A., & Elçi, Ş. (2009). Effects of selective withdrawal on hydrodynamics of a stratified reservoir. *Water resources management, 23, 1257-1273.*
2. Çalışkan, A., & Elçi, Ş. (2009). Effects of selective withdrawal on hydrodynamics of a stratified reservoir. *Water resources management, 23, 1257-1273.*
3. Afshar, A., Kazemi, H., & Saadatpour, M. (2011). Particle swarm optimization for automatic calibration of large scale water quality model (CE-QUAL-W2): Application to Karkheh Reservoir, Iran. *Water resources management, 25,* 2613-2632.
4. Mohammadnejad, B., Parchami, N., & Bahmanesh, J. (2014). Simulation of Nutrient Loading in the Mahabad Dam Reservoir Using the CE-QUAL-W2 Two-Dimensional Model. *Journal of Civil and Environmental Engineering, 44(4), 107-115.*
5. Aboutalebi, M., Bozorg-Haddad, O., & Loáiciga, H. A. (2017). Multiobjective design of water-quality monitoring networks in river-reservoir systems. *Journal of environmental engineering, 143(1), 04016070.*
6. Ziaie, R., Mohammadnezhad, B., Taheriyoun, M., Karimi, A., & Amiri, S. (2019). Evaluation of thermal stratification and eutrophication in Zayandeh Roud Dam Reservoir using two-dimensional CE-QUAL-W2 Model. *Journal of Environmental Engineering, 145(6), 05019001.*
7. Arefinia, A., Bozorg-Haddad, O., Oliazadeh, A., & Loáiciga, H. A. (2020). Reservoir water quality simulation with data mining models. *Environmental Monitoring and Assessment, 192, 1-13.*
8. Rasouli, S., Bazargan, J., & Shoaei, S. M. (2020). Application of IRWQISC Index in the Water Quality Evaluation of Dam Reservoirs (Case Study: Golabar Dam Reservoir, Zanjan). *Iranian Journal of Irrigation & Drainage, 13(6), 1820-1831.*
9. Hanjaniamin, A. E., Tabrizi, M. S., & Babazadeh, H. (2023). Dissolved oxygen concentration and eutrophication evaluation in Yamchi dam reservoir, Ardabil, Iran. *Applied Water Science, 13(1), 1-12.*

© 2024 by the authors. Licensee SCU, Ahvaz, Iran. This article is an open access article distributed under the terms and conditions of the Creative Commons Attribution 4.0 International (CC BY 4.0 license) (http://creativecommons.org/licenses/by/4.0/).

Journal of Hydraulic Structures
J. Hydraul. Struct., 2024; 10(1): 72-81
DOI: 10.22055/jhs.2024.19074



OPEN ACCESS

Investigating sediment changes during dry and wet periods at both upstream and downstream stations of the Karkheh Dam

Somayeh Rezaeimanesh [1]
Sara Parvizi [1]
Ali Talebi [*1]

Abstract

Estimating sediment yield accurately in watershed areas is always a concern for planners. A noteworthy aspect in this regard is the variation in river behavior within watershed areas during dry and wet periods. The objective of this study is to investigate sediment variations during dry and wet periods at both upstream and downstream stations of the Karkheh Dam. To achieve this, flow and sediment statistics from the Afrineh-Kashkan station upstream of the dam and the Pay-Pol station downstream, spanning a 38-year period (1350-1398), were utilized. For this purpose, dry and wet periods were initially identified, and for each, sediment rating curve was plotted. To enhance the sediment rating curve relationship, corrective factors including FAO, QMLE and Smearing were employed. Performance evaluation of each was conducted using indicators such as RMSE, ME and P. The results of the sediment analysis at each station during dry and wet periods indicate that the specific sediment yield has decreased during dry periods and experienced a significant increase during wet periods. Moreover, the specific sediment yield at the downstream station (Pay-Pol) of the Karkheh Dam has also shown a considerable reduction, indicating the dam's impact on sediment regulation downstream.

Keywords: Dry, Wetness, Sediment Rating Curve, Flow Discharge, Sediment Load.

Received: 09 November 2023; Accepted: 16 April 2024

1. Introduction

Information on the precise mechanisms of erosion, sediment transport, and sedimentation processes in the country is significantly less than the existing needs, and in many cases, substantial discrepancies are observed between measurements and conducted estimates. Rivers are constantly confronted with erosion and sediment transport phenomena. Therefore, estimating sedimentation amounts is of paramount importance in soil conservation projects, watershed management, and the utilization of water resources [1]. Suspended sediment load is an indicator of total watershed sedimentation, and assessments of sediment production in watershed areas often rely on scattered,

[1] Department of Rangeland and Watershed Management, Faculty of Natural Resources , Yazd University, Yazd, Iran.
[*] Email: talebisf@yazd.ac.ir **(Corresponding Author)**

limited, and irregular sampling of riverbed suspended sediments [2]. In the absence of actual sediment measurements, hydrologists use sediment rating curves to determine suspended sediment concentration, and the most common method for estimating sediment load involves using data on suspended sediment concentration and flow rate data [3]. Determining the effects of dry or wet periods in a region is a fundamental requirement for environmental and economic planning, especially in resource management, particularly water resources. Sediment load in watersheds is influenced by various factors such as precipitation, topography, geology, vegetation cover, land use and soil erodibility characteristics. Therefore, all these factors must be taken into account for calculating sediment load [4].

The majority of sediment transported by most rivers constitutes suspended load. Accurate recognition of its quantity, especially during periods of dry and wet, is crucial. Ghaffari and colleagues investigated the impact of dry and wet periods on the specific sediment yield in the Karkheh watershed. The results indicated a notable decrease in sediment load during dry periods and a significant increase during wet periods at all study stations [5]. In a study, Nazari Samani and colleagues [6] investigated the general impact of land use changes and precipitation variations on sediment production in the Taleghan watershed. The results indicated a significant increase in suspended sediment load during wet periods and a meaningful decrease during dry periods [6]. Garbrecht examined the impact of climate change on erosion and sedimentation, finding that increased precipitation led to an elevation in suspended sediment load, while decreased precipitation resulted in a reduction in suspended sediment load in the watershed area in western Oklahoma [7].The United States Soil Conservation Service also concluded, through a study on the relationship between climate change and soil erosion, that soil erosion is expected to increase in the future due to the rise in runoff [8].

Talebi et. al [9] focused on determining the optimal sediment rating curve equation and its correlation with physical characteristics in the semi-arid regions of the Pol-Doab watershed. They concluded that the MVUE correction factor in the sediment rating curve at the intermediate range can be utilized for annual-scale sediment yield prediction. Additionally, the FAO correction factor provides a more accurate estimation of sediment yield at monthly, weekly, and daily scales [9]. Talebi et al [10] undertook the examination of the most suitable sediment rating curve equation for dry climates (southwest Iran) and humid climates (north Iran). The research results demonstrated the appropriateness of the intermediate range method for stations in dry and semi-arid regions, as well as stations in humid and semi-humid areas. Moreover, the best correction factor for both dry and semi-arid, and humid and semi-humid stations was found to be MVUE [10].

Finally, the purpose of this research is to investigate sediment changes during dry and wet periods at upstream and downstream stations of the Karkheh dam over a 38-year period. This is done to determine the dam's impact on the concentration of riverine sediments.

2. Materials and methods

2.1. Study area

The Karkheh Watershed, covering an area of approximately 50.768 square kilometers, is situated between 46 degrees 57 minutes to 49 degrees 10 minutes east longitude and 31 degrees 48 minutes to 34 degrees 58 minutes north latitude. This watershed consists of five sub-basins: Gamasiab, Qarasu, Symareh, Kashkan and Karkheh down. The average annual precipitation in the watershed is 492 millimeters. From a climatic perspective, the Karkheh Watershed belongs to the Mediterranean climate [5]. For conducting this study, hydro-meteorological stations within the watershed were considered, and stations located upstream of the Karkheh Dam (Afrineh-Kashkan)

and downstream of the dam (Pay-Pol) were chosen as the study stations. Their specifications are provided in Table 1, and Figure 1 depicts the geographical locations of the Karkheh watershed and the selected stations.

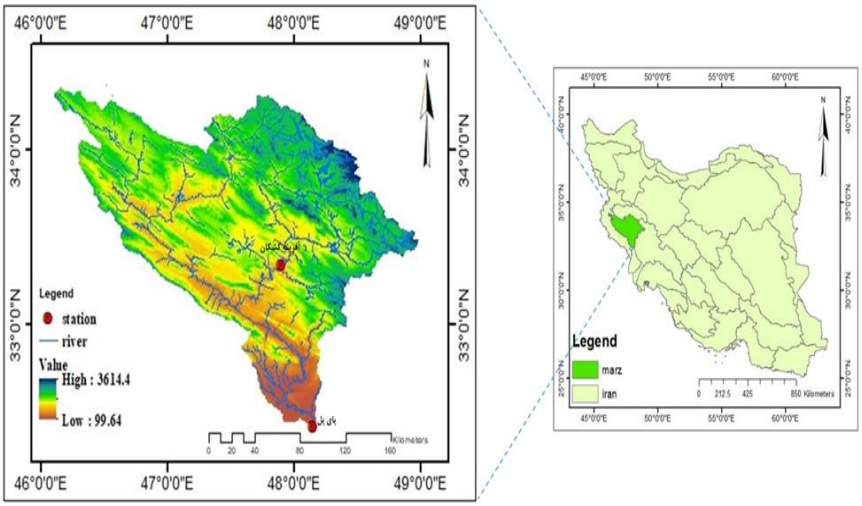


Figure 1. Geographical location of the study area

Table 1. Geographical characteristics of the studied stations

Station name	The area of the field) (Km^2	Geographical attributes		
		Longitude	latitude	Height (m)
Afrineh-Kashkan (upstream of the dam)	3670	47-53	33-20	820
Pay-Pol (downstream of the dam)	42620	48-09	32-25	90

2.2. Methodology

In this research, a 38-year statistical period (1350-1398) was utilized. Initially, using Dubai's existing statistics, dry and wet years were identified separately. Subsequently, based on Dubai's data and suspended sediment obtained from the upstream station (Afrineh-Kashkan station) and the downstream station (Pay-Pol station) in the Karkheh watershed, sediment rating curves were plotted for each period of dry and wetness on a logarithmic scale. Finally, an examination of sediment changes during dry and wet periods at the upstream and downstream stations of the Karkheh Dam was conducted.

2.3. Determining dryness and wetness

In the present study, Dubai's statistics and sediment data from Afrineh-Kashkan and Pai-Pal stations in the Karkheh River were utilized over a 38-year statistical period (1350-1398). Equation (1) was employed to identify wet and dry periods.

$$\frac{Qi - Qm}{S} \qquad (1)$$

In equation (1), Qi represents the average discharge in each year, Qm is the mean discharge, and S is the standard deviation of the total annual discharge. Years with an index value greater than 0.5 are considered wet years, and those with values less than 0.5 are considered dry years [11].

2.4. Sediment Rating curve

In many cases, experts use sediment rating curve models for predicting and estimating suspended sediment concentration in the absence of actual sediment data [12]. To construct the sediment rating curve, the approach of the U.S. Bureau of Reclamation (USBR) is employed. In this method, by simultaneously plotting flow discharge and the corresponding concentration of suspended sediment on a logarithmic coordinate graph and fitting the best line through the data, the exponential equation of the curve is obtained as follows.

$$Q_S=a\ Q_W^b \tag{2}$$

In equation (2), Qs represents sediment concentration in milligrams per liter, Qw is the discharge in cubic meters per second, and a and b are the constant coefficients of the equation.

In this regard, due to skewness, it has often failed to accurately represent sediment concentration at different flow rates [13]. Skewness has led to the residuals (the difference between observed and calculated values) not following a normal distribution, and its value becoming greater than zero [14]. The skewness of the sediment rating curve arises from two factors. The first factor is due to the transformation of the equation from a logarithmic to a natural form in the linear regression model, essentially related to the nature of the rating curve. The second factor results from extrapolation for estimating sediment in high flow discharges [13], which is associated with the quantity and quality of the data, leading to a significant error in sediment estimation. Various methods have been proposed to reduce skewness and increase accuracy in extrapolating the sediment rating curve.

In order to achieve unbiased estimates with minimum error, various researchers have proposed several statistical correction factors (FAO, Smearing, QMLE and β) that affect the sediment rating curve equation [2]. These factors are calculated as follows.

$$a=\frac{\overline{Q_s}}{\overline{Q_w}^b} \tag{3}$$

In equation (3), $\overline{Q}$s represents the observed average sediment concentration in milligrams per liter or ton per day, $\overline{Q}$w is the observed average flow discharge in cubic meters per second, a is the FAO correction factor, and b is the same coefficient as in the USBR equation [9].

$$CF_{Smearing}\frac{1}{n}\sum_{i=1}^{n}10^{\varepsilon i} \tag{4}$$

$$\varepsilon_i=\log(C_o)-\log(C_e) \tag{5}$$

In equation (4), n represents the number of observational samples, ε^i is the residual of the least squares regression model, CO is the observed sediment concentration in milligrams per liter or ton per day, and Ce is the estimated sediment concentration in milligrams per liter or ton per day [9].

$$CF_{QMLE} = e^{(2{,}561S^2)} \quad (6)$$

$$S^2 = \frac{\sum_{i=1}^{n}(\log C_o - \log C_e)}{(n-2)} \quad (7)$$

In equations (6) and (7), (e) is the exponential function equal to 2.718, \(S^2) is the standard error, (n) is the number of observational samples, (ε^i) is the residual of the least squares regression model, (CO) is the observed sediment concentration in milligrams per liter or ton per day, and (Ce) is the estimated sediment concentration in milligrams per liter or ton per day [9].

$$CF_{\beta} = 1 + \beta \quad (8)$$

$$\beta = \frac{\sum_{i=1}^{n}(\varepsilon_i)}{\sum_{i=1}^{n} \alpha Q_w{}^{b}} \quad (9)$$

In equations (8) and (9), ε^i represents the residual of the least squares regression model. (b) and (a) are the coefficients of the USBR equation, and (Qw) denotes the mean flow rate of observed samples in cubic meters per second [9].

After obtaining the sediment index equations using the provided correction factors, performance evaluation and determination of the optimal equation are carried out in this study using indicators such as Root Mean Square Error (RMSE), Maximum Error (ME), and Accuracy Index [15]. These indices are calculated as follows:

$$RMSE = \left[\frac{\sum_{i=1}^{n}(SSC_o - SSC_e)^2}{N}\right]^{1,2} \quad (10)$$

In equation (10), (SSCo) represents the observed sediment concentration in milligrams per liter or ton per day, (SSCe) is the estimated sediment concentration in milligrams per liter or ton per day, and (N) is the number of observed samples. A smaller value for this coefficient indicates less difference between observed and estimated data, resulting in higher predictive accuracy of the relationship [9].

$$ME = 1 - \left[\frac{\sum_{i=1}^{n}(SSC_o - SSC_e)^2}{\sum_{i=1}^{n}(SSC_o - SSC_m)^2}\right] \quad (11)$$

In equation (11), (SSCo) represents the observed sediment concentration in milligrams per liter or ton per day, (SSCe) is the estimated sediment concentration in milligrams per liter or ton per day, (SSCm) is the average observed sediment concentration in milligrams per liter or ton per day, and (ME) ranges from negative infinity to one, with higher values indicating greater accuracy in estimation [9].

$$P = \left[\sum_{i=1}^{n} \frac{SSCe}{SSCo}\right] \Big/ N \quad (12)$$

In equation (12), (SSCo) represents the observed sediment concentration in milligrams per liter or ton per day, (SSCe) is the estimated sediment concentration in milligrams per liter or ton per day, (SSCm) is the average observed sediment concentration in milligrams per liter or ton per day, and (ME) ranges from negative infinity to one, with higher values indicating greater accuracy in estimation [9].

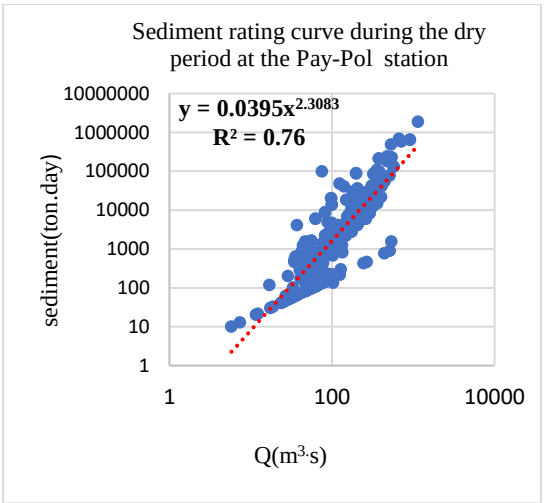
3. Results and Discussion

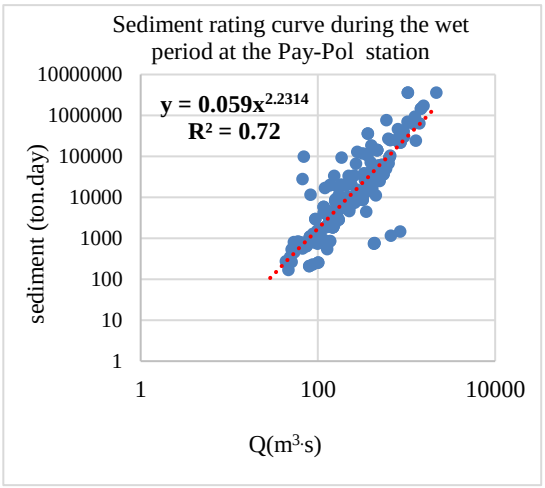
Based on the discharge data of the 38-year period of dry years, wet periods were determined separately. In the next step, based on the discharge and suspended sediment data collected at the upstream station (Afrineh-Kashkan) and the downstream station (Pay-Pol) located in the Karkheh watershed, for each of the statistical periods of dry and wet periods, separate the sediment Rating curve of the basin in a plane with coordinates Alogarithm was drawn. The equation of the initial sediment measurement of each station in the period of dry and dry can be seen in Table (2). Figure 2 shows the graphs of sediment Rating curves in the studied stations of Karkheh basin in dry and wet periods.

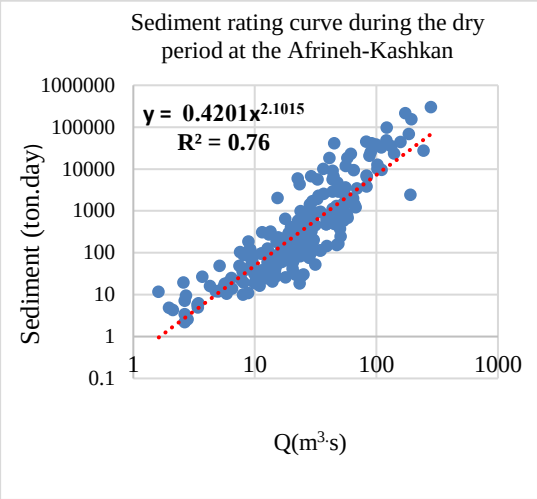
Table 2. Equations of primary sediment Rating of each station in dry and wet periods

Station name	dry periods		wet periods	
	Rating equation	R^2	Rating equation	R^2
Afrineh-Kashkan (upstream of the dam)	$Q_S=0.4201Q_W^{2.1015}$	0.76	$Q_S=0.202Q_W^{2.2886}$	0.78
Pay-Pol (downstream of the dam)	$Q_S=0.0395Q_W^{2.3083}$	0.76	$Q_S=0.059Q_W^{2.2314}$	0.72

After plotting the sediment rating curve for each station, factors such as FAO, QMLE, and Smearing were employed to enhance the curve's relationship. For evaluating the performance and determining optimal equations in both wet and dry periods, metrics including root mean square error (RMSE), maximum error (ME), and accuracy index (P) were utilized. The closer the value of P and ME is to 1 and the value of RMSE is to zero, the more accurate the model is [9]. To select the optimal equation for each station, the ranking of the evaluation index values has been used. In this way, the closest value of P and ME index to 1 and the closest value of RMSE index to zero at the station in question, which represents the smallest difference between estimated and observed sediment values, was assigned the rank of 1. The next values of the indicators in the desired station were also ranked accordingly. Then, the ranked values of the columns were compared and the optimal equation was selected based on the column with the lowest ranked values. Tables 3 and 4 show the results of the values of the evaluation indices of each of these equations and the results related to the ranking of the values of the evaluation indices.







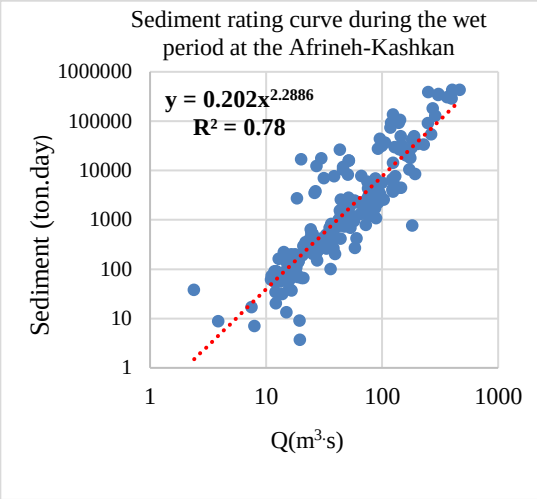


Figure 2. Graphs of sediment rating curves in the studied stations of Karkheh watershed in dry and wet periods.

Table 3. Evaluation indicators of the accuracy of the sediment Rating curve using the correction factors of Afrineh-Kashkan station

Index evaiution		No coefficients	FAO	QMLE	Smearing
dry periods	RMSE	13135.396	10835.02	12571.33	10756.64
	ME	0.07725	0.4825	0.154	0.260
	P	1.665	23.74	3.15	5.46
	Total rating	9	7	8	6
wet periods	RMSE	122378.8	634355.78	81757.55	88257.85
	ME	0.410	-14.83	0.737	0.693
	P	2.10	36.52	4.32	3.93
	Total rating	7	12	5	6

Table 4. Evaluation indicators of the accuracy of the sediment Rating curve using the correction factors of Pay-Pol station

Index evaiution		No coefficients	FAO	QMLE	Smearing
dry periods	RMSE	47311.86	69018.902	33931.26	40027.67
	ME	0.3611	-0.36	0.671	0.542
	P	2.56	23.22	5.529	4.134
	Total rating	7	12	5	6
wet periods	RMSE	887615.56	3695396.61	711471.84	766246.94
	ME	0.295	-11.212	0.547	0.4749
	P	2.5895	61.196	5.0913	4.3012
	Total rating	7	12	5	6

Given the results of Tables 3 and 4 during the dry period, the optimal equations for the Afrineh-Kashkan and Pay-Pol stations, respectively, are obtained using the smearing correction factor (Equation 13) and the QMLE correction factor (Equation 14). During the wet period, the equation obtained using the QMLE correction factor (Equations 15 and 16) was selected as the optimal equation for the Afrineh-Kashkan and Pay-Pol stations

$$Q_S=1.38Q_W^{2.1015} \quad (13)$$
$$Q_S=0.085Q_W^{2.3083} \quad (14)$$
$$Q_S=0.4141Q_W^{2.2886} \quad (15)$$
$$Q_S=0.116Q_W^{2.2314} \quad (16)$$

Continuing with the utilization of the obtained equations and substituting the daily discharge, the total sediment yield for each station is determined in tons per day. By dividing the average sediment load per unit area of the study basin for each station, the specific sediment yield is obtained in tons per year per square kilometer. The examination of the specific sediment yield at Afrineh-Kashkan station (upstream) and Pay-Pol station (downstream) during dry and wet periods indicates that the specific sediment yield has decreased in dry periods and experienced a significant increase in wet periods. Figure 3 illustrates the trends of sediment changes during both dry and wet periods for both Afrineh-Kashkan and Pay-Pol stations. As can be seen, in dry periods the rate of sediment is subtractive while in wet period, sediment is additive.

Additionally, the specific sediment yield at the downstream of the dam station (Pay-Pol station) has also shown a considerable decrease in both dry and wet periods. Figure 4 depicts the trends of sediment changes at Afrineh-Kashkan and Pay-Pol stations. Table 5 presents the average sediment load and specific sediment yield values for each station during dry periods.

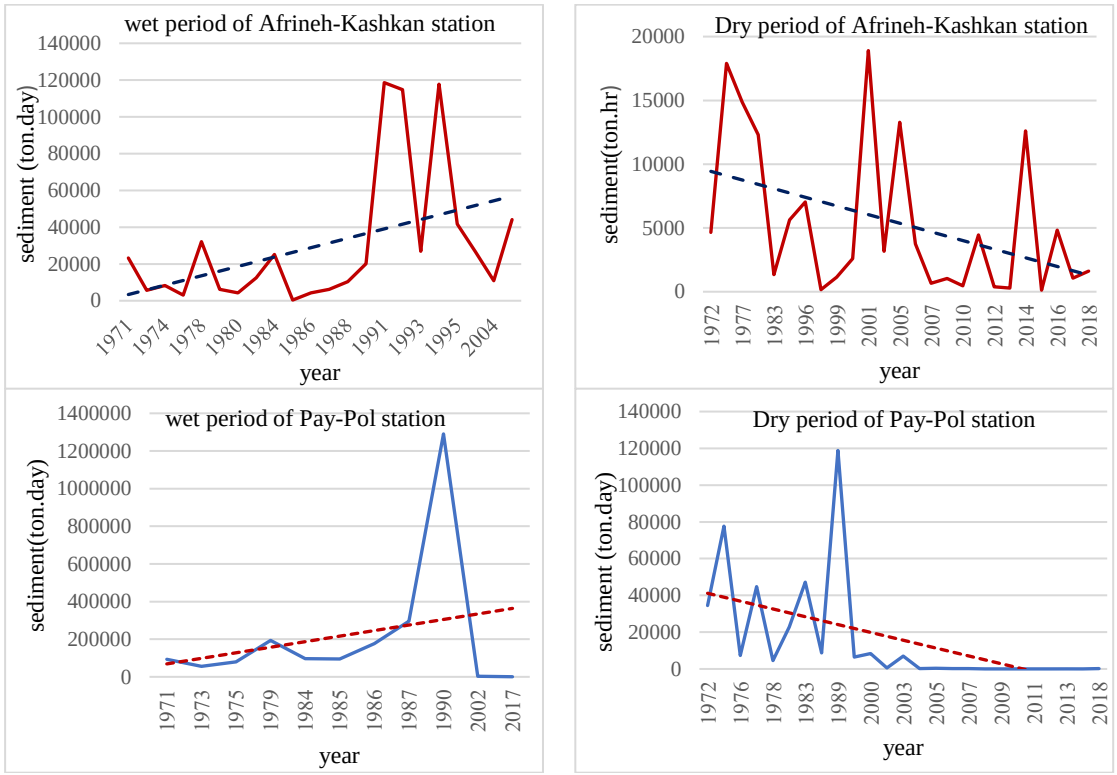
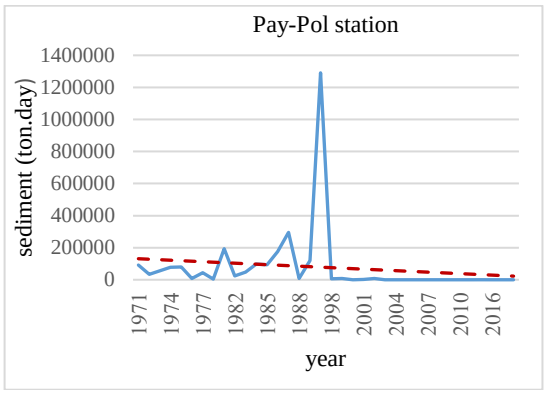


Figure 3. The trend of sediment changes during dry and wet periods at the Afrineh-Kashkan and Pay-Pol stations



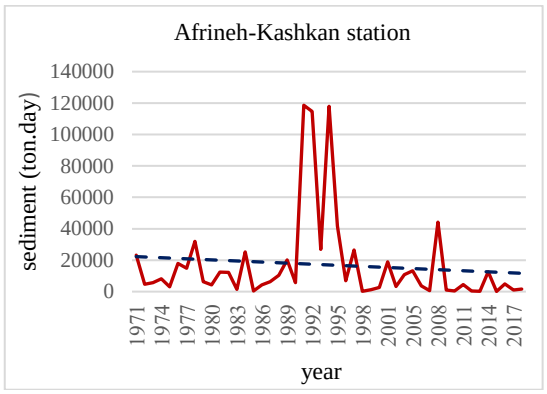


Figure 4. The trend of sediment changes at the Afrineh-Kashkan station (upstream) and the Pay-Pol station (downstream)

Table 5. Average Sediment Load and Specific Sediment Yield for Each Station During Dry and Wet Periods

Station name	Area (Km^2)	dry periods		wet periods	
		Average sediment load (ton.y)	Special sediment (ton.y.km^2)	Average sediment load(ton.y)	Special sediment (ton.y.km^2)
Afrineh-Kashkan (upstream of the dam)	3670	4838.169	1.31	24124.24	6.57
Pay-Pol (downstream of the dam)	42620	20382.01	0.47	11850.5	2.78

As can be seen in Table 5, the presence of a dam in both wet and dry periods, leads to the regulation and reduction of sedimentation.

4. Conclusion

The current study focuses on investigating sediment changes during dry and wet periods at the upstream and downstream stations of the Karkheh Dam, utilizing sediment rating curves. Using discharge and sediment data and employing the mentioned methods, optimal sediment rating curve equations were determined for dry and wet periods at both the upstream and downstream stations of the Karkheh Dam. The results indicate that during the dry period, the Afrineh-Kashkan station exhibited a Smearing correction factor, while the Pay-Pol station showed a QMLE correction factor. In the wet period, both the Afrineh-Kashkan and Pay-Pol stations displayed a QMLE correction factor, demonstrating greater accuracy compared to other coefficients.

The notable increase in specific sediment yield during the wet period can be attributed to the rise in precipitation during wetter periods and the subsequent increase in runoff. Additionally, the intensification of destructive floods enhances the capacity for erosion and sediment transport. The volume of sediment transported into rivers is higher during wet periods compared to dry periods. These results coincide with the results of Ghafari et al. [5], Garbrecht [7], American Soil Conservation Service [8], Nazari Samani et al. [6] in relation to the increase in the amount of sediment load, it corresponds to the increase in the amount of precipitation. Furthermore, the

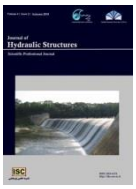
results indicate a significant decrease in specific sediment yield at the downstream of the dam station (Pay-Pol station) during both dry and wet periods. This highlights the role of the dam in mitigating sediment transport.

References

1. Sadeghi, S.H.R., Mizuyama, T., Miyata, S., Gomi, T., Kosugi, K., Fukushima, T., Mizugaki, S. & Onda, Y. (2008). Development, evaluation and interpretation of sediment rating curves for a Japanese small mountainous reforested watershed. Geoderma, 198-211.
2. Kao, Sh., Lee. T., & Milliman, J.D.(2005). Calculating highly fluctuated suspended sediment fluxes from mountainous rivers in Taiwan. Terrestrial Atmospheric and Oceanic Sciences, (16) 3, 653-675.
3. Horowitz, A. J. (2003). An evaluation of sediment rating curves for estimating suspended sediment concentrations for subsequent flux calculations. Hydrological Processes. 17(17), 3387–3409.
4. Thampson, S, A. (1999). Hydrology for water management, Balkema, Rotterdam.
5. Ghafari, G., & Mahdavi, M. (2013). The effect of periods of dry and dry on the amount of specific sediment (case study: Karkheh watershed). Iranian Journal of Watershed Management Science and Engineering, 8(27), 49. (In Persian)
6. Nazari Samani, A., Hervey, H., Panahi, M., & Jafari Shalmazari, M. (2012). The effect of land use change and precipitation on the sediments of Taleghan basin. Rangeland and watershed management journal. 165-157. (In Persian)
7. Garbrecht, J. (2010). Climate variations, soil conservation, and reservoir sedimentation, Federal Interagency Conference, In 2nd Joint Federal Interagency Conference, Las Vegas.
8. Benjamin, H. (2008). Draft National Water Program Strategy: Response to Climate Change Request for Comments, United States environmental protection agency, Washington, D. C.20460.
9. Talebi, A., Bahrami, A., Mardian, M., & Mahjoobi, J. (2015). Determination of optimized sediment rating equation and its relationship with physical characteristics of watershed in semi-arid regions. Desert, 20(2): 135-144.
10. Talebi, A., & Pourmohammadi, S. (2015). Investigating the most appropriate sediment measurement equation in dry (southwestern Iran) and humid (northern Iran) climates. Geographical Research, 31 (1) :118-128 (In Persian)
11. Mahmoudian Shushtari, M., & Ranginkaman, M. (2009). Investigation and comparison of different methods of preparation of sediment Rating curve based on water regime in Dez River (Tale Zang station), 8th International Seminar on River Engineering. Ahvaz, Iran. (In Persian)
12. Masfaei, J., Pourjam, A., & Tabatabai, M. (2016). Comparing the efficiency of sediment Rating model and neural network in river bed load estimation. Geography and Sustainability of Environment, 33-44. (In Persian)
13. Verwani, J., Najafinejad, A., & Mirmoini Kohrorudi, A. (2008). Modification of sediment Rating curve using minimum variance method, Journal of Agricultural Sciences and Natural Resources.

© 2024 by the authors. Licensee SCU, Ahvaz, Iran. This article is an open access article distributed under the terms and conditions of the Creative Commons Attribution 4.0 International (CC BY 4.0 license) (http://creativecommons.org/licenses/by/4.0/).

Journal of Hydraulic Structures
J. Hydraul. Struct., 2024; 10(1): 82-92
DOI: 10.22055/jhs.2024.19075



OPEN ACCESS

Laboratory investigation of the effect of hysteresis phenomenon of supercritical flow on the rough bed on the relative residual energy parameter

Ehsan Aminvash [*1]
Rasoul Daneshfaraz [1]
Sina Sadeghfam [2]
Seyed Bahman Mousavi [2]

Abstract

In the present study, the hysteretic behavior of supercritical flow that can occur in a channel near additional structures, such as changes in the bed of the channel, has been investigated experimentally and analytically. For this purpose, two diameters of the channel floor materials of 1.12 and 2 cm have been used. The critical depth ranges from 2.7 to 4.5 cm and the used flow rates range from 250 to 600 liters per minute. The flow rate increases in the primary flow and then decreases in the secondary flow into the laboratory flume. The possible flow regimes near the narrowed section are classified based on the relative depths and relative energy remaining in sections 1 and 2 as a function of the Froude number passing under the valve. The results show that by increasing the flow rate and then decreasing it, in some flow rates, two different behaviors can be seen from the flow in the same laboratory conditions. Also, the results showed that with the increase in the diameter of the bed material, the remaining relative energy values have increased a lot, so that in the primary flow, the amount of these depths indicates the subcritical regime, and in the secondary flow, with the formation of hysteresis phenomenon in some discharges, it indicates the regime Also, with the increase in the average diameter of the material, the hysteretic behavior of the flow becomes more intense.

Keywords: Hysteretic Behavior, Possible Flow Regimes, Rough Bed, Relative Depth, Relative Residual Energy.

Received: 09 November 2023; Accepted: 16 April 2024

[*] Email: Ehsan.aminvash1994@gmail.com **(Corresponding Author)**
[1] Department of Civil Engineering, Faculty of Engineering, University of Maragheh, Maragheh, Iran,
[2] Department of Soil Science, Faculty of Agriculture, University of Maragheh, Maragheh, Iran.

CC BY

1. Introduction

The main goal of this research is to investigate the paradoxical behavior of supercritical flow on a rough bed. The existence of such a contradictory behavior occurs due to the phenomenon of hysteresis, which there have been very limited studies to understand and it has not been investigated for the rough bed. The occurrence of hysteresis phenomenon when the flow meets the obstacle is generally expected. So, for the same input flow, two different behaviors are observed, which is dependent on the flow cycle. Flow cycle means increasing the flow rate to a certain value and then reducing it to the initial flow rate. This phenomenon is one of the important issues that occurs in practical work in nature, but unfortunately it is not considered in the design of hydraulic structures.

The first study related to the phenomenon of hysteresis in the group that investigates the protrusion of the canal floor, goes back to the research of Abecasis and Quintella [1]. The studies in this group mostly investigate the theoretical and experimental behavior of the hysteresis phenomenon on the floor protrusion with a fixed width. The most important research in this field is related to Asteria [2], Lawrence [3], Baines and Whitehead [4] and Defina and Susin [5]. Austria [2] has described the hysteretic behavior of the flow on the channel bottom protrusion using the catastrophe theory. The theory used by him is based on the use of classic flow equations such as special energy equations along with catastrophe theory equations. Lawrence [3] investigated the permanent flow passing over the embankment of the channel floor and its different behaviors. The results showed that there may be two stable states for the same input conditions, which leads to the formation of a hysteresis loop.

Baines and Whitehead [4] investigated the hysteretic behavior of the flow on the channel bottom protrusion theoretically and experimentally. The results of theoretical and experimental studies showed that in the same conditions of the input flow, two different states are created for the stability of the flow, which indicates the existence of a hysteretic loop. Dafina and Susin [5] initially theoretically presented relations to investigate this phenomenon on the bulge and then investigated it experimentally. They defined two weak and strong reactions in the conditions of the same inlet flow for the flow, that the weak reaction is when the flow regime is supercritical and the obstacle does not affect the change of the flow regime. On the other hand, strong reaction indicates a condition where the hydraulic jump causes the flow regime to change to subcritical.

The second group of studies is related to cross-sectional contraction in the flow path, and in this regard, we can refer to the research of Akers and Bukhov [6]. They investigated the hysteretic behavior in gradual contraction theoretically and in the field. The results showed that diagonal waves of supercritical flow can be influenced by other effects such as surface tension. Defina and Viero [7] investigated the different states created by the flow in the gradual constriction. The results of their numerical and laboratory investigations showed that the friction and slope of the channel floor have an effect on the stability of the flow and can create different hysteretic loops. Sadeghfam et al. [8] investigated the hysteretic behavior of supercritical flow in the face of local narrowing of the channel by using classical hydraulic equations and catastrophe theory. Their laboratory results showed that the use of relations related to catastrophe theory along with classical relations can describe hysteretic behavior.

The third group of studies is in the field of bridge foundations and in this field we can refer to Dafina and Susin's research [9]. In this research, they used several bridge piers with different diameters and investigated the behavior of the flow in front of the used piers. Also, they presented a theoretical relationship to predict the occurrence of hydraulic hysteresis. The results showed that two different weak and strong reactions are created in the same input conditions when the flow meets the bridge foundations with narrowness. Daneshfaraz et al [10-11] also investigated the hysteretic behavior of the flow in sudden and gradual narrowings in are research.

The review of previous research shows that despite the theoretical and experimental studies conducted in connection with the hysteretic behavior of the flow, there is a need to conduct more extensive studies to investigate the unknown dimensions of the flow behavior. These unknown dimensions are more noticeable in obstacles such as bridge foundations that reduce the cross-section of the flow, which have been more or less mentioned in previous studies, but no studies have been conducted in the field of rough bed. Generally, the analytical relationships in such obstacles are less consistent with the laboratory results than in other obstacles. The reason for this could be because the flow pattern against these obstacles does not provide the possibility of creating an accurate theory in accordance with the one-dimensional flow approach. Therefore, in the present research, for the first time, analytical equations were presented to investigate the hysteretic behavior of the flow on the rough bed, and then longitudinal profiles were created in the laboratory, and the possible regimes of the flow, and then the effect of this phenomenon on the amount of relative residual energy was investigated.

2. Methodology

2.1. Description of forced hydraulic jump

Forced hydraulic jump is a process in which the supercritical flow regime created by hydraulic structures is forced to transform into the subcritical regime. In the present study, the hydraulic jump is created by two components, which are described below. The first component includes a sliding valve that is installed in the channel to measure or control the incoming flow, and it converts the subcritical flow behind the valve into the supercritical flow. The second component is the change in the bed of the channel due to the aggregates arranged in the flow path, which causes the hydraulic jump and reduces the destructive energy of the supercritical flow. Figure (1) shows different longitudinal profiles under the same input conditions. Figure (1a) shows that at one or more specific flow rates, the rough bed has an effect on the flow regime, and with the formation of a hydraulic jump on it, the supercritical flow regime turns into a subcritical flow. In other words, the flow shows a strong reaction (SI) against the rough bed. As the flow rate increases, the flow speed increases and the hydraulic jump leaves the rough bed (Figure 1b). In other words, the flow regime is on the supercritical bed and the flow shows a weak reaction (WI) against the rough bed. In this stage, the flow rate is slowly reduced until it reaches the initial flow rate. In this case, it can be seen that the behavior created on the rough bed is the same as Figure (b1) and there will be no effect of hydraulic jump on the rough bed. This state can appear in one or more specific discharges. When the flow reaches the end of the rough bed, it will leave the rough bed downstream of the channel with the critical regime.

In the above figure, E_0 is the specific energy passing through the sub-valve, E_1 is the specific energy of the flow before the rough bed, E_2 is the specific energy of the flow on the rough bed, E_{min} is the minimum specific energy, hf is the energy loss due to the rough bed, and ΔH_j is the energy loss due to the hydraulic jump. be Longitudinal drop caused by the rough bed when the condition of figure (1a) is established and the hydraulic jump occurs transfers the flow regime

from supercritical to subcritical with the sign $(h_f)_L$ and when the condition of figure (1b) is established and no hydraulic jump occurred and the flow regime throughout the channel is supercritical, it is indicated by the sign $(h_f)_l$. It should be noted that when the situation in figure (1a) is established, in addition to the energy loss caused by the rough bed, there will also be an energy loss caused by the hydraulic jump.

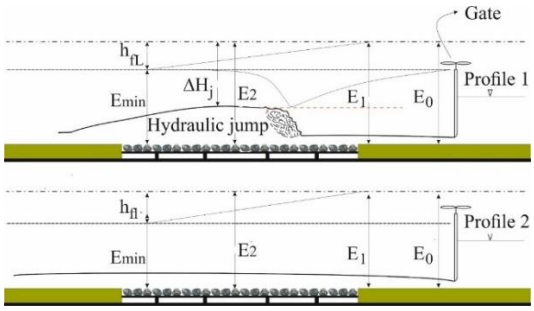


Figure 1. Longitudinal profiles of the flow created on the rough bed

2.2. Experimental equipment

The tests necessary to achieve the goals of the present research have been carried out in a laboratory flume with dimensions of 5 m in length, 0.5 m in height and 0.3 m in width, with zero longitudinal slope, walls and floor made of transparent Plexiglas. In general, 162 tests have been conducted to investigate the hysteretic behavior on the rough bed. In order to create a supercritical flow, a vertical metal valve with an opening of 2 cm, placed at a distance of 1.5 m from the inlet tank, was used. The flow entering the flume is pumped by two pumps, each with a capacity of 450 liters per minute, and the flow rate was read using rotameters installed on the pumps. In order to measure the depth of the flow, a point depth gauge with an error of ±1 mm was used. The present research has been investigated in two models with two average diameters, whose information is presented in Table 1. Figure (2) shows the schematic of the laboratory flume and the equipment installed on it, as well as the materials used in the rough bed.

Table 1. The data range and characteristics of rough bed materials

Case no.	Q (lit/min)	D_{50} (cm)	y_{cr} (cm)	y_1 (cm)	y_2 (cm)	Reynolds ($\times 10^4$)
Case 1	250~600	2.0	2.7~5.28	1.62~5.87	1.85~5.62	(5~11.2)
Case 2		1.12		1.37~4.66	1.81~4.25	

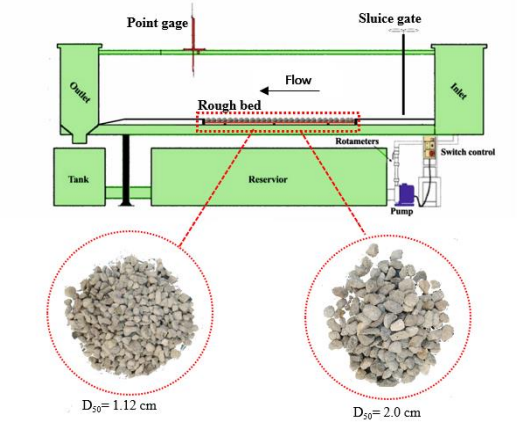


Figure 2. Schematic image of laboratory flume and rough bed materials

2.3. Longitudinal profiles

The configuration of the forced hydraulic jump in the present research includes separate parts, which are: 1- The vertical sluice gate that is installed to measure or control the flow in the channel, and its role in this research is only to form the supercritical flow, and 2- The change in the channel floor and the roughening of the bed using natural materials (sand) which causes the formation of a hydraulic jump on the rough bed and turns the supercritical flow regime into subcritical, which is very necessary to check the hydraulic parameters in this case. In Figure (1), cross-section [1] shows the starting point of the rough bed and cross-section [2] shows the flow on the rough bed and the place where the hydraulic jump is formed (in different flow rates, the position of the cross-section [2] may change). It is necessary to explain that the section [0] shows the location of the supercritical flow generating valve and the *vena cotracta* flow.

Based on the objectives of the present research and as shown in Figure (1), two types of longitudinal flow profiles can be distinguished, which are:

Profile 1: This profile shows the formation of hydraulic jump in sections [1] and [2]. Section [0] is the flow passing *vena contracta*, in which section the flow regime passing through it is supercritical. In other words, at section [1], the flow is supercritical. This flow regime is created by the upstream valve. In section [2], due to the turbulence and increase in flow depth, a hydraulic jump is formed and the flow regime is transferred to subcritical.

Profile 2: This profile indicates the absence of hydraulic jump throughout the laboratory channel. Due to the increase in flow rate, the rough bed is no longer able to maintain the hydraulic jump in its upstream, the hydraulic jump is transferred to the downstream of the channel and the regime created in sections [1] and [2] becomes supercritical. In other words, the flow regime at all points is equal to the subcritical and supercritical flow regime.

2.4. Dimensional analysis

According to Figure (1), the effective parameters for investigating the hysteretic behavior of the supercritical flow on the rough bed are as follows.

$$f_1(Q,\rho,\mu,g,a,D_{50},d,B,L,y_0,y_{cr},h_f,y_1,y_2,E_0,E_1,E_2)=0 \quad (1)$$

Where, Q is the flow rate [L^3T^{-1}], ρ is the fluid density [ML^{-3}], μ is the dynamic viscosity [$ML^{-1}T^{-2}$], g is the acceleration of gravity [LT^{-2}], a is the opening of the flow generating valve supercritical [L], D_{50} average diameter of bed material [L], d distance of valve to the beginning of rough bed [L], B width of channel [L], L length of rough bed [L], y_0 depth of flow in section 0 [L], y_{cr} critical depth [L], h_f loss due to rough bed [L], y_1 depth of flow in section 1 [L], y_2 depth of flow in section 2 [L], E_0, E_1 and E_2 according to the specific flow energy [L] in sections 0, 1 and 2. Considering the parameters ρ, y_0 and g are repeated parameters and using the Pi-Buckingham method, the dimensionless parameters are presented according to equation (2).

$$\frac{E_1}{E_0},\frac{E_2}{E_0}=f_2(Fr_0,\frac{D_{50}}{L}) \quad (2)$$

3. Results and discussion

3.1. Longitudinal profiles of flow

The longitudinal profiles of the flow on the rough bed are shown in Figures 4 and 5. As mentioned, in conducting the experiments of the present research, flow rates of 250 to 600 liters per minute (LPM) have been used in an increasing manner, and then from 600 to 250 LPM in a decreasing manner with increasing and decreasing steps of 50 LPM. Carefully in these figures, in each model with the increase and decrease of the flow rate, two different behaviors of the flow can be seen at several same flow rates, which is the hysteretic behavior of the flow in the rough bed. Table 2 and Figure 3 provide a summary of the tests performed and the hysteretic flow behavior. In the flow with increasing flow rates, the rough bed placed in the flow path causes a hydraulic jump, and during this time sections 1 and 2 are both in the subcritical regime. With the increase in flow rate, the hydraulic jump moves downstream and the flow regime becomes supercritical along the entire length of the channel. Then, with the reduction of the flow rate, the behavior that is created in the system indicates that in a certain flow rate, although not in all flow rates, two different behaviors of the flow are observed, so that the flow with a reduced flow rate created in the channel places sections 1 and 2 completely in the supercritical regime.

Table 2. Hydraulic flow parameters in model 1

Figure no.	Fr_0 *(vena contracte)*	Flow regimes (Sub/Super critical)		Profiles	Flow cycle	Case no.
		Sec. 1	Sec. 2			
3-a	2.157	Sub	Sub	P.1	Flow increasing	1
3-b	2.679	Sub	Sub		Flow increasing	
3-c	3.630	Sub	Sub		Flow increasing	
3-d	4.269	Super	Super	P.2	Increased flow caused supercritical hysteresis	
3-e	3.630	Super	Super		Decreasing flow	
3-f	2.679	Super	Super		Decreasing flow	
3-g	2.157	Sub	Sub	P.1	Decreasing flow caused subcritical hysteresis	

Figure 3 shows the regime changes and the longitudinal profiles of the flow on a rough bed with an average material diameter of 0.2 cm. By increasing the flow rate up to 350 LPM, sections 1 and 2 are in the subcritical regime. By increasing the flow rate to 400 LPM, the flow regime in the control section is transferred to supercritical. Then, with the gradual decrease of the flow rate up to 300 LPM, the control section is still in the supercritical regime, until reaching the flow rate of 250 LPM, the regime in the control section becomes subcritical.

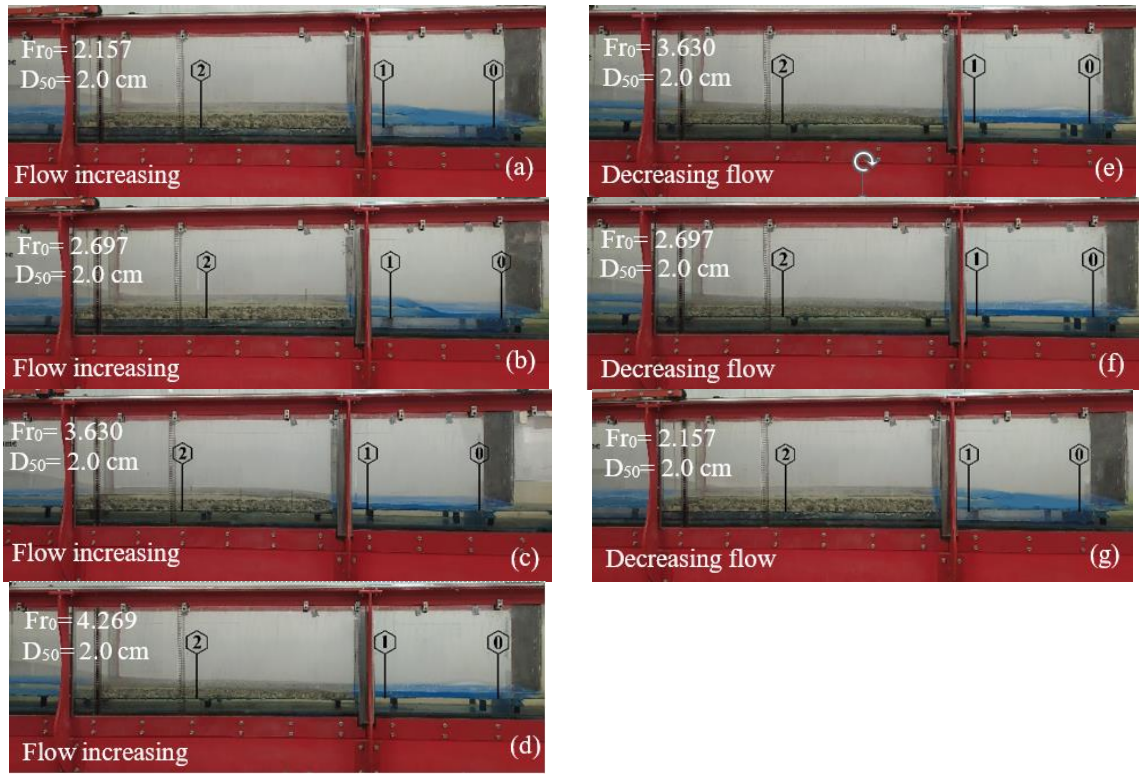


Figure 3. Case number 1 experiments to observe the phenomenon of hysteresis on a rough substrate

3.2. Relative residual energy

Figure 4 shows the changes of the relative residual energy against the Froude number of the *vena contracta* flow for model 1 with an average material diameter of 2 cm. Figure 4a, b shows the hysteretic behavior of the relative residual energy of the flow in section 1 and figures 4c, d show the said behavior in section 2.

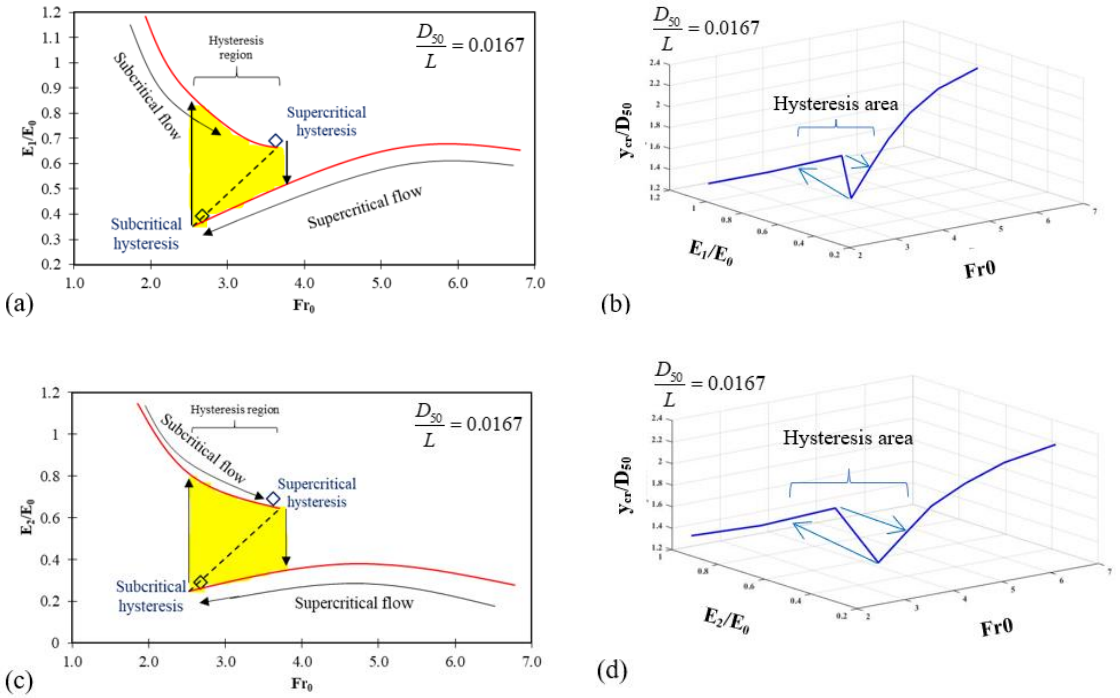


Figure 4. Reproduction of the hysteresis phenomenon by experimental data on model 1 in relative residual energy

It is carefully deduced in these figures that with the increase of the Froude number, the amount of relative remaining energy increases in both sections, but in an increasing and decreasing flow, in two flow rates with the same environmental and laboratory conditions, different behaviors are observed at flow rates of 300 and 350 LPM, it shows its hysteretic flow behavior. In these flow rates, in the initial flow, with the increase of the flow rate, a hydraulic jump is formed on the rough bed, and the flow regime becomes subcritical in the control sections. In the secondary flow, with the gradual decrease of the flow rate and when it reaches 300 and 350 liters per minute, unlike the increasing state, the hydraulic jump is not formed on the rough bed and the flow regime on the rough bed is supercritical and the Froude number in which the hysteresis phenomenon is formed and is located in the range of $2.697 \le Fr_0 \le 3.630$. Also, Figure 5 shows the changes in the hysteresis phenomenon of relative residual energy in model 2 with an average diameter of 1.12 cm. In this model, according to model 1, the phenomenon of hysteresis is formed in the Froude number range of $2.697 \le Fr_0 \le 3.630$, and its difference with model 1 is in the amount of relative energy remaining, so that in model 1, with the formation of the phenomenon of hysteresis, the amount of relative energy remaining in Sections 1 and 2 increase by 42.38% and 53.5%, respectively, and in model 2, the remaining relative energy increases by 39.5% and 45.4%. The values of the remaining relative energy increase in the present research are significant numbers and if hysteretic behavior is formed in the existing structures in nature, the downstream structures will be damaged and destroyed.

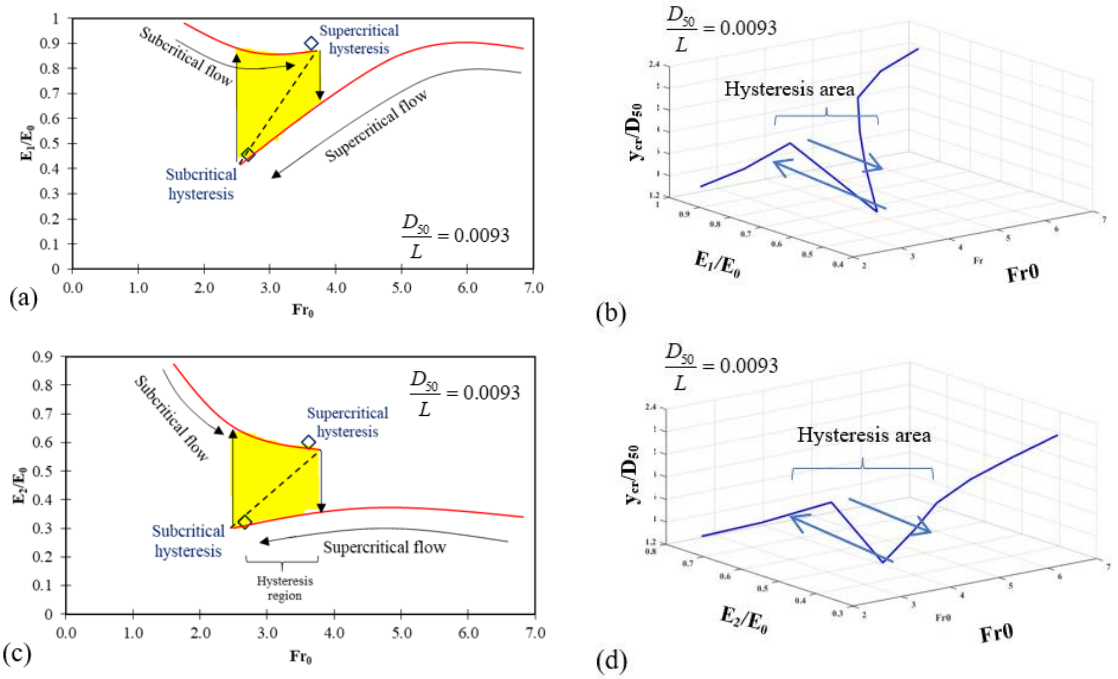


Figure 5. Reproduction of the hysteresis phenomenon by experimental data on model 2 in relative residual energy

The main reason for the formation of hysteresis phenomenon in hydraulic structures is the dependence of the flow behavior of the flow on its previous state. In this way, in the initial flow, with the increase of the flow, the flow velocity increases and with the decrease of the depth, sections 1 and 2, which were in the subcritical regime at low flow rates, become the supercritical regime. For this reason, some of the stresses created in the flow are lost with the decrease in flow rate, and some of these stresses remain as residual stress in the system, which causes the formation of hysteresis phenomenon.

The investigations carried out in the present research on the rough bed with two average diameters of the material show that with the increase of the D_{50} of the material, the residual relative energy of the flow increases. Also, the hysteretic behavior of the flow in comparing the models with each other shows that with the increase of D_{50} of the materials, the created hysteresis area has caused many changes in the amount of relative remaining energy. In other words, the hysteretic behavior of the flow on the rough bed with larger material diameter is intensified. The reason for this is that when the flow is placed on the roughness with a diameter of 2 cm, the interference of water and air in the flow of the increasing flow is high, and with the formation of the hysteresis phenomenon following the decrease of the flow, the hydraulic jump disappears and the depth of the flow decreases drastically. In other words, by increasing the average diameter of the materials, the range of hysteresis widens and causes a noticeable change in the size of the parameters. Table 3 shows the effect of hysteretic behavior on the relative residual energy parameter and the percentages of decrease or increase of these parameters. Figure 6 also shows the column chart of changes in relative residual energy values.

Table 3. Relative residual energy changes affected by hysteresis phenomenon

Model	Parameter	E_1/E_0	E_2/E_0
	Case 1	42.38%	53.59%
	Case 2	39.50%	45.41%

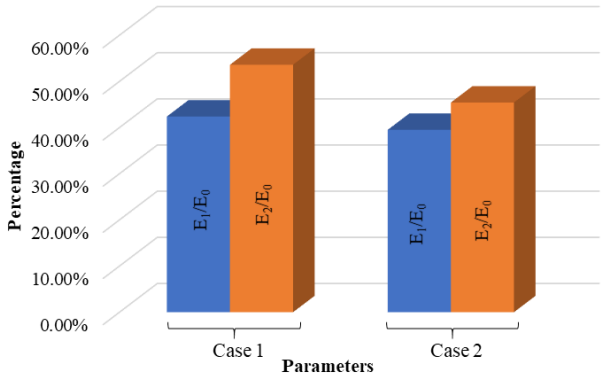


Figure 6. Column chart of relative residual energy changes affected by hysteretic behavior

4. Conclusion

The phenomenon of hysteresis in supercritical flow is one of the issues that is not well known and it is formed near the additional structures in water supply systems, water transmission lines and canals. The hysteretic behavior of the flow causes the creation of different states in the flow, and the main reason for this behavior is the dependence of the current state of the flow on its previous state, and the investigation of this phenomenon should be the attention of designers and hydraulic engineers in the hydraulic design of structures. In the present study, in order to achieve its goals, which is to investigate the conditions and reasons for the presence and absence of hydraulic jump, the formation of two different profiles and the effect of hysteretic behavior on the relative residual energy. Investigating the hysteretic behavior of the flow, the water entered the flume by creating a flow from 250 to 600 LPM and by creating a decreasing flow from 600 to 250 LPM with increasing and decreasing steps of 50 LPM.

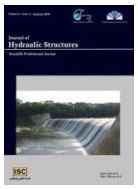
1- In model 1, where a rough bed with D_{50} = 2.0 cm was used in the flow path, the hysteresis phenomenon was formed in the range of Froude number 2.697 and 3.63, which increased the flow rate to more than 350 LPM the supercritical regime and with the flow rate decrease to less than 300 LPM, the flow regime returns to the subcritical regime.
2- With the formation of the hysteresis phenomenon, the remaining relative energy has been affected by it, so that this phenomenon has caused many changes in the amount of the remaining relative energy as follows:
   - ✓ The hysteretic behavior of the flow reduced the amount of relative residual energy in model 1 in sections 1 and 2 to 42.38 and 53.59%.
   - ✓ The phenomenon of hysteresis reduced the remaining relative energy in model 2 in stages 1 and 2 by 39.5 and 45.41%.
   - ✓ The increase in the average diameter of the substrate material aggravated the hysteretic behavior in the control section.

References

1. Abecasis F.M, Quintela A.C, (1964). Hysteresis in steady free-surface flow. Water Power 16 (4), 147–151.
2. Austria P.M, (1987). Catastrophe model for the forced hydraulic jump. Journal of Hydraulic research, 25 (3), 269–280.
3. Lawrence G.A, (1987). Steady flow over an obstacle. Journal of Hydraulic Engineering, 113(8), 981-991.
4. Baines P.G, Whitehead J.A, (2003). On multiple states in single-layer flows. Physics of fluids, 15(2), 298-307.
5. Defina A, Susin F.M, (2006). Multiple states in open channel flow. Vorticity and Turbulence Effects in Fluid Structures Interactions, pp. 105-130.
6. Akers B, Bokhove O, (2008). Hydraulic flow through a channel contraction: Multiple steady states. Physics of fluids, 20(5), 1-15.
7. Defina A, Viero D.P, (2010). Open channel flow through a linear contraction. Physics of Fluids, 22(3), 1-12.
8. Sadeghfam S, Khatibi R, Hassanzadeh Y, Daneshfaraz R, Ghorbani M.A, (2017). Forced hydraulic jumps described by classic hydraulic equations reproducing cusp catastrophe features. Arabian Journal for Science and Engineering, 42(9), 4169-4179.
9. Defina A, Susin F.M, (2003). Hysteretic behavior of the flow under a vertical sluice gate. Physics of Fluids, 15(9), 2541-2548.
10. Daneshfaraz R, Aminvash E, Sadeghfam S, (2023). Laboratory and Theoretical Study of Hysteretic Effects on Hydraulic Characteristics of Flow at the Site of Smooth to Rough Bed Conversion. Iranian Journal of Science and Technology, Transactions of Civil Engineering, 1-13.
11. Daneshfaraz R, Sadeghfam S, Aminvash E, Abraham J.P, (2022). Experimental investigation of multiple supercritical flow states and the effect of hysteresis on the relative residual energy in sudden and gradual contractions. Iranian Journal of Science and Technology, Transactions of Civil Engineering, 46(5), 3843-3858.

© 2024 by the authors. Licensee SCU, Ahvaz, Iran. This article is an open access article distributed under the terms and conditions of the Creative Commons Attribution 4.0 International (CC BY 4.0 license) (http://creativecommons.org/licenses/by/4.0/).

Journal of Hydraulic Structures
J. Hydraul. Struct., 2024; 10(1):93-105
DOI: 10.22055/jhs.2024.19076



OPEN ACCESS

Mapping Vulnerability of aquifer to saltwater intrusion using fuzzy membership function

Marjan Moazamnia [*1]
Sina Sadeghfam [2]
Alireza Babaeian Amini [1]

Abstract

Groundwater is one of the most important sources of drinking, industrial, and agricultural water in arid and semi-arid regions, where the occurrence of droughts, rapid population growth, and the corresponding increase in water demand threaten groundwater resources. Over-exploitation and mismanagement of groundwater resources result in environmental problems such as subsidence and saltwater intrusion in coastal aquifers. The risk of saltwater intrusion threatens the Urmia aquifer due to the proximity of the aquifer to Lake Urmia and severe groundwater decline. This study evaluates the vulnerability of saltwater intrusion by the GALDIT framework. The results show the conservative vulnerability index with low efficiency, where vulnerable areas are limited to a narrow strip near the coastline. Fuzzy membership functions were employed within the GALDIT framework to increase efficiency. The results of the modified GALDIT resolve the weakness of presenting conservative results in the basic GALDIT framework.

Keywords: Saltwater Intrusion, GALDIT, Water Quality Index, Groundwater Level, Urmia Plain Aquifer

Received: 09 November 2023; Accepted: 16 April 2024

[*] Email: m.moazamnia@ubonab.ac.ir **(Corresponding Author)**
[1] Department of Civil Engineering, Faculty of Engineering, University of Bonab, Bonab, East Azerbaijan, Iran.
[2] Department of Civil Engineering, University of Maragheh, Maragheh, East Azerbaijan, Iran.

CC BY

1. Introduction

In many coastal aquifers, groundwater is considered the most important source of water supply for agriculture, drinking, and industry. In these areas, freshwater sources are subject to saltwater intrusion, which causes concerns for water security. Normally, the saltwater intrusion in coastal aquifers is due to high pumping rates and drops in the groundwater level, and this causes the degradation of the groundwater quality [1-3]. It is undeniable and necessary to deal with the problem of saltwater intrusion in coastal areas, especially in cases where we are faced with the rapid growth of the human population. Therefore, it is necessary to provide management and protection solutions. Assessing the vulnerability of groundwater and mapping areas prone to saltwater intrusion can be an effective help in this direction. Considering that decontamination of groundwater is a long process and often contamination is detected when decontamination of the aquifer becomes almost impossible, therefore preventing the contamination of groundwater systems is very important in the management of groundwater resources. One of the appropriate ways to prevent groundwater pollution is to identify the vulnerable areas of the aquifer. Based on the vulnerability study of an aquifer, the areas vulnerable to saltwater intrusion are mapped. The vulnerability index is a kind of relative, dimensionless, and unmeasurable characteristic and depends on the specifications of the aquifer and its geological and hydrogeological environment.

Groundwater vulnerability assessment should be based on scientific, accurate, and objective evidence. Different methods were introduced to assess vulnerability with high accuracy. In general, simulation, statistical, indexing and overlay (I/O) methods are used to assess the vulnerability of groundwater in many parts of the world. Simulation methods use mathematical models to estimate pollution, and their limitations are the need for very accurate data and the high sensitivity of the model to input data. The statistical method uses statistical techniques to determine the relationship between spatial variables and pollutants in groundwater, while minimize the error. The limitations of the method include the dependency of result on water quality observations, data accuracy, and accurate selection of spatial variables. The I/O method is widely used due to its simplicity, less need for data, and accurate description of vulnerability compared to other methods. In this method, the degree of vulnerability is calculated according to the indicators and the results are qualitative and relative [4]. Table 1 present a summary of recent studies conducted I/O methods to determine the vulnerability of coastal aquifers to saltwater intrusion. Based on the table, the basic and modified GALDIT frameworks were widely used [5] considering human and natural factors. Table 1 shows that the most important factors for assessing the vulnerability of coastal aquifers, including sea water rise, the height of the groundwater level at sea level [6-8], risks caused by climate change, overexploitation of aquifers [3,9] and pumping rate [10-11].

Table 1. Summary of recent studies related to overlay/index (O/I) methods for mapping the vulnerability of coastal aquifers to saltwater intrusion

Researcher	Aquifer type	Validation factors	Key contributions
Lobo Ferreiraet al., (2005)	unconfined	–	• Climate change (for example, sea level rise) and overexploitation of aquifers have significant effects on saltwater intrusion.
Mahesha et al., (2011)	unconfined	Cl^-/HCO_3^-	• The GALDIT framework for assessing the vulnerability of coastal aquifers to saltwater intrusion due to sea level rise is quite effective and reasonable.
Sophiya and Syed (2013)	unconfined	Cl^-	• Temporal changes in the effective parameters in the intrusion of seawater in the aquifer are necessary.
Kura et al., (2015)	unconfined	NO_3^-	• A very strong negative correlation has been observed between GALDIT and groundwater resistance (r=-0.86).
Pedreira et al., (2015)	unconfined	Cl^-,NO_3^-	• The parameter of the height of the groundwater level above the sea level is a very important factor for evaluating the vulnerability of the aquifer to saltwater intrusion.
Recinos et al., (2015)	unconfined	Cl^-	• The height of the groundwater above the sea level and the impact of saltwater intrusion are important parameters in the vulnerability of the aquifer.
Bouderbala et al., (2016)	unconfined	WQI	• GALDIT does not include the impact of pumping wells.
Najib et al., (2016)	unconfined	Pumping rate	• The obtained vulnerability mapping corresponds to the pumping rate.
Gorgji and Moghadam (2016)	unconfined	TDS	• In case of data limitations, the pumping rate can replace the distance of the water level from the sea level.
Klassen and Allen (2017)	unconfined	EC	• It is necessary to use the chemical indicators of underground water to accurately identify vulnerable areas to saltwater intrusion.
Allouche et al., (2017)	unconfined	NO_3^- and Specific resistance of groundwater	• Land use parameter was added to GALDIT parameters. • A negative correlation has been observed between GALDIT and the specific resistance of groundwater (r=-0.61).
Motevalli et al., (2018)	unconfined, confined and leaky	EC ، TDS and SAR	• A high correlation was observed between GALDIT output mapping (mean r = 0.73) and hydrogeochemical index factors. • The depth of groundwater and the reduction of the level of groundwater were identified as the most important factors.

This study employs the vulnerability assessment of saltwater intrusion in the Urmia aquifer using the GALDIT framework. To reduce the impact of expert judgment on the allocation of recommended rates, fuzzy membership functions were incorporated. Also, the time-varying parameters of this framework were prepared in different years and its effect on the GALDIT index were evaluated.

2. Methodology

2.1.The GALDIT Framework

GALDIT is a vulnerability indexing framework for saltwater intrusion that includes two parts assigning weight and rate values to the incorporated layers, which was developed by Chachadi and Lobo-Ferreira [18]. The GALDIT framework is based on the hydrogeological (water depth, aquifer thickness), physical (distance from the coast), hydrodynamic (hydraulic conductivity), and hydrochemical (sea intrusion effect) characteristics of the aquifer. In other words, GALDIT uses relatively simple layers with data that are easily collected to quantify the saltwater intrusion vulnerability index [18].

The word GALDIT is an acronym that stands for six incorporated layers used to evaluate the vulnerability index of saltwater intrusion. These layers include (G) Groundwater occurrence (type of aquifer: unconfined, confined, and leaky), (A) Aquifer hydraulic conductivity, (L) height of groundwater Level, (D) Distance from the shore, (I) Impact of existing saltwater intrusion status, and (T) aquifer Thickness. In this system, the first step involves assigning weight and rate values for each layer. The weight assigned to each layer shows its importance compared to others in the saltwater intrusion process. After preparing layers related to parameters using geographic information system processing, weights recommended by Chachadi and Lobo-Ferreira are applied to the corresponding layer. These weights are presented in Table 2 [18]. The ranking of the layers is also applied using dimensionless numbers ranging from 2.5 to 10 (2.5, 5, 7.5, and 10), according to the recommendations of Chachadi and Lobo-Ferreira [18]. The most important layer is assigned a weight of 4, while the least important parameter is assigned a weight of 1. The highest rate value indicates the highest vulnerability index, while the lowest rate value indicates the lowest vulnerability index. Finally, the decision criterion is the weighted sum of the rates of the incorporated layers.

Table 2. Rate (left numerical column) and weight (bottom row) values for GALDIT layers

		Groundwater occurrence (G)	Aquifer hydraulic conductivity (A)	height of groundwater Level (L)	Distance from the shore (D)	Impact of existing saltwater intrusion status (I)	aquifer Thickness (T)
Rate	10	confined	>40	<1	<500	>2	>10
	7.5	unconfined	10-40	1-1.5	500-750	1.5-2	7.5-10
	5	leaky	5-10	1.5-2	750-1000	1-1.5	5-7.5
	2.5	Bounded aquifer (limited to hydrogeological boundaries)	<5	>2	>1000	<1	<5
	Weight	1	3	4	4	1	2

GALDIT index (GI) is calculated as follows:

$$GI = G_r G_w + A_r A_w + L_r L_w + D_r D_w + I_r I_w + T_r T_w \quad (1)$$

where the subscripts *r* and *w* indicate the rates and weights of layers, which are applied as per the values in Table 2. The minimum and maximum GALDIT index can be calculated according to Equation 1 and Table 2. The vulnerability of the coastal area to saltwater intrusion is estimated based on the value of the GALDIT index. The lower the value of the GALDIT index causes the lower the vulnerability of the area to saltwater intrusion. When the GALDIT index is calculated, it becomes possible to classify the desired area into several classes.

2.2.The Study Area

The study area is situated in Urmia Plain, which is located in West Azerbaijan province in the northwest of Iran. The plain covers an approximate area of 1000 km^2 and encompasses the alluvial aquifer. It also includes the main river basins, such as Shahrchay, Nazlochay, Rozechay, and Baranduzchay. The rivers originate in the Mor Daghlar mountain range, along the borders between Turkey and Iran. These rivers are fed by the Saru, Silvana, Moana, and Ziveh mountains. The general channel of surface water flow in Urmia Plain flows from west to east and towards Lake Urmia. The plain has an average height of 1320 meters above sea level, according to the Digital Elevation Model (DEM) of the Landsat satellite, as shown in Figure 1.

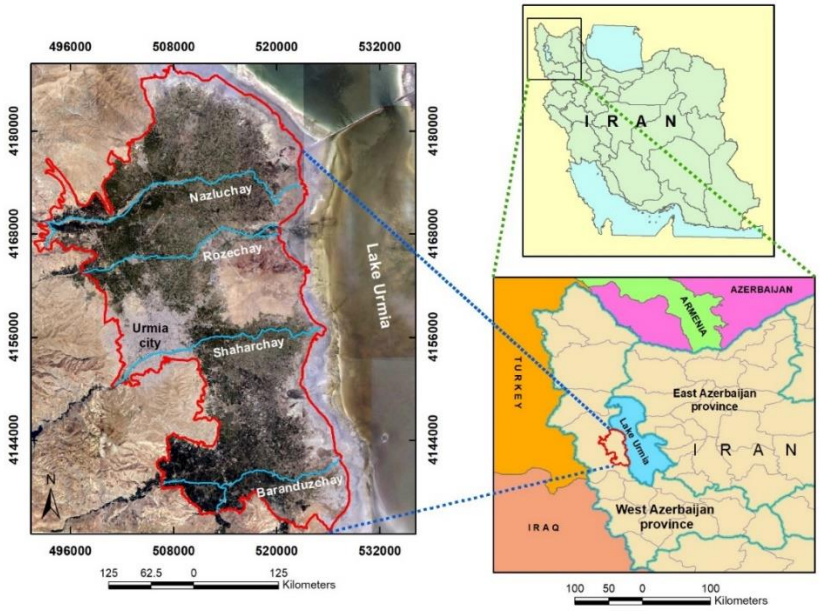


Figure 1. Location map of the study area

The quality and quantity of groundwater have a direct impact on the economic and livelihood issues of the people living in the Urmia Plain. In general, in the aquifers on the edge of Lake Urmia, extensive dam construction has hurt surface water resources. Currently, the surface and groundwater resources of Urmia Plain are facing damages due to incorrect planning, including a sharp decrease in the groundwater level, which was also reported in the survey conducted by Amiratae and Zeinalzadeh (2016) [19]. Our investigations show the monthly changes in the water level of Lake Urmia is 2.7 cm/month; and the monthly changes in the water level is 1.8 cm/month in a period of 16 years (2009-2015). Also, the correlation coefficient between the level of the lake and the level of the groundwater level was calculated as 0.71. The calculated value for the correlation coefficient indicates the mutual relationship between the lake and the aquifer.

3. Results and Discussion

3.1. Assessing the Vulnerability of Saltwater Intrusion using the GALDIT Framework

Figure 2 displays the layers that contributed to the GALDIT framework in the Urmia Plain aquifer. The first layer of GALDIT, which represents the Groundwater occurrence (G), is shown in Figure 3(a). Since the Urmia plain aquifer is an unconfined aquifer, the rate of this layer has a constant value of 7.5 and does not cause any spatial changes in the calculation of the GALDIT index. The second layer, Aquifer hydraulic conductivity (A), is presented in Figure 2(b) and is based on the result of the pumping test. The figure indicates that in the southeastern parts of the plain near the coast, its value is in the medium range, which can increase the vulnerability index of saltwater intrusion. Although the outskirts of Urmia city and west of the plain have relatively high hydraulic conductivity, their distance from the coastline is expected to prevent significant effects in increasing the vulnerability of saltwater intrusion.

The layer corresponding to height of groundwater Level (L) is shown in Figure 2(c). This layer was calculated using the data of groundwater level and sea level in August 2009 and prepared using the kriging interpolation technique. The figure indicates that this layer decreases as it approaches the coastline, which increases the vulnerability to saltwater intrusion. It should be noted that this layer is one of the dynamic parameters of GALDIT that changes over time. Therefore, the spatial distribution of this layer was prepared in different years to investigate the effect of temporal changes on the GALDIT index, which are discussed subsequently.

Figure 2(d) shows the spatial distribution of the layer related to Distance from the shore (D), which was calculated using the Euclidean distance tool in ArcMap software. The Euclidean distance decreases by approaching the coastline, which can increase the vulnerability to saltwater intrusion. Spatial distribution of the Impact of existing saltwater intrusion status (I) was calculated using the qualitative data of the ratio of chloride ions to the total of bicarbonate and carbonate ions in August 2009 and using the kriging interpolation technique, The results are shown in Figure 2(e). According to this figure, it can be seen that the value of this index is high in the eastern part of the plain near the coastline, which can increase the vulnerability to saltwater intrusion. It should be noted that this layer, like the L layer, is one of the dynamic layers of GALDIT, and its temporal changes will be evaluated in the following. The aquifer Thickness (T) as the last layer contributed in the GALDIT framework is extracted from the results of the geoelectrical profiles of the geophysical test and after interpolation with the kriging method, it is shown in Figure 2(f).

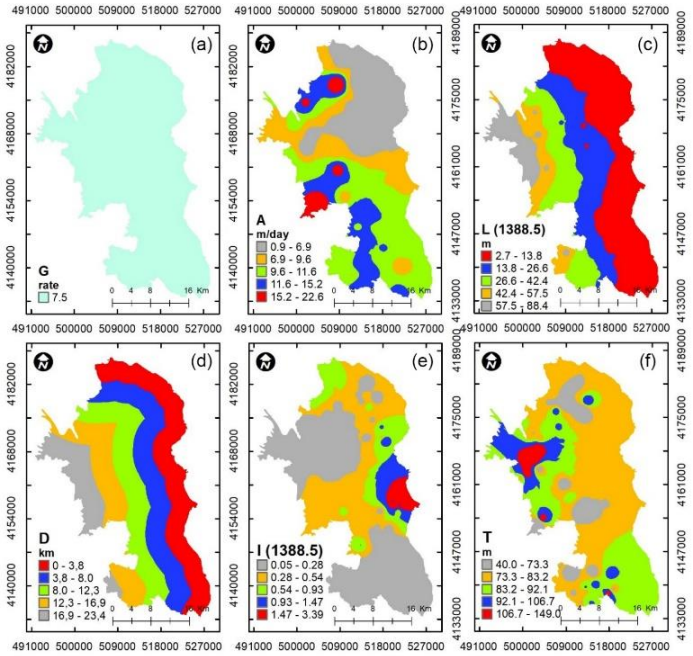


Figure 2. The GALDIT layers: (a) Groundwater occurrence, (b) Aquifer hydraulic conductivity, (c) height of groundwater Level, (d) Distance from the shore, (r) Impact of existing saltwater intrusion status and (g) aquifer Thickness

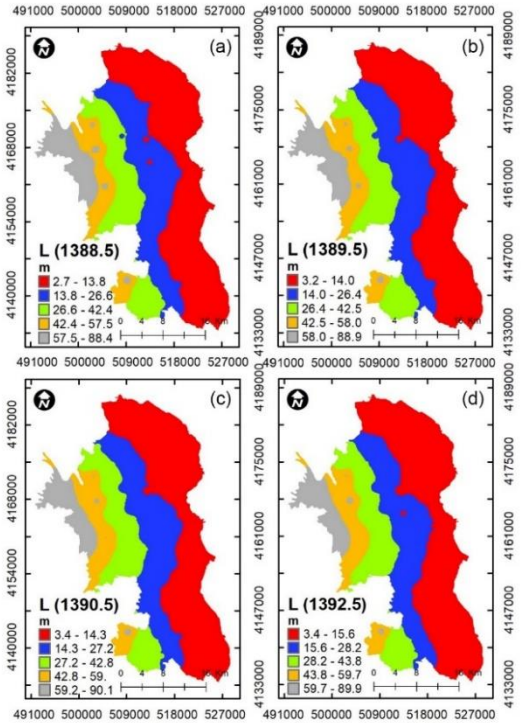


Figure 3. Temporal changes of the layer L of the GALDIT framework: (a) August 2009, (b) August 2010, (c) August 2011, (d) August 2012

Figure 3 shows the spatial distribution of the layer of height of groundwater Level (L) in August 2009, 2010, 2011, and 2012. According to the figure, it can be seen that despite the changes in L values, the spatial pattern does not change significantly. Therefore, it is expected that the temporal changes of this parameter will not have much effect on the vulnerability of saltwater intrusion. It should be noted that the selection of data in the above years was selected according to the accessibility of the data.

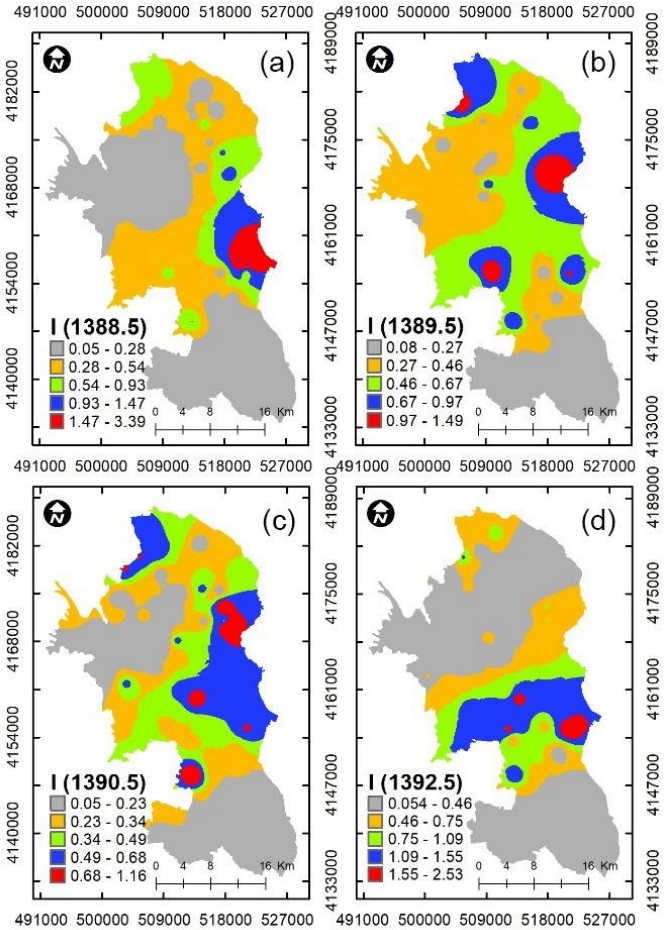


Figure 4. Time changes of parameter I of the GALDIT framework: (a) August 2009, (b) August 2010, (c) August 2011, (d) August 2012

Figure 4 shows the spatial distribution of the influence layer of the Impact of existing saltwater intrusion status (I) in August 2009, 2010, 2011, and 2012. According to the figure, it can be seen that the pattern of spatial changes of this parameter in the aforementioned years is remarkable. But despite time changes, high values for this layer are observed in the eastern part of the plain near the coastline, which can intensify the vulnerability of saltwater intrusion in these areas.

3.2.The results of Saltwater Intrusion Vulnerability using Basic GALDIT

After preparing the contributed layers in the GALDIT framework, considering that each of the layers has a different unit (dimension) and interval of changes compared to each other, these layers using the recommended rate values in Table 2 were classified, then weighted overlay analysis was performed using the weights presented in the table. The results of this analysis, which shows the GALDIT index in the vulnerability of saltwater intrusion, are presented in Figure 5. It should be noted that considering the temporal changes of L and I parameters, the vulnerability results for the years 2009, 2010, 2011, and 2012 are shown separately in this figure. It can be seen carefully in this figure that in a very narrow band near the coastline, the vulnerability of saltwater intrusion is high. In other words, GALDIT has presented very conservative results, so in the areas outside this band with a very small area, the vulnerability of the aquifer is in the low to medium range, which according to the characteristics of the study area and the researchers' knowledge of the plain Urmia does not seem logical.

3.3.Vulnerability Results using the Modified GALDIT

The reason for providing conservative results by the Basic GALDIT framework is the existence of pre-recommended rates by expert judgment, which causes the classification of some layers in one or two classes. It is worth mentioning that the classification of layers in one or two classes reduces the effect of that layer on the final result. This section aims to reduce the influence of expert judgment in the classification of layers by using fuzzy membership functions and taking into account the characteristics of the studied area. For this purpose, fuzzy membership functions were used to normalize GALDIT layers. Considering that GAIT parameters are directly related to saltwater intrusion, the values of these layers are normalized from the maximum value to the minimum value to 1 to 0 respectively. While L and D parameters are inversely related to saltwater intrusion, the values of these layers are normalized from the maximum value to the minimum value to 0 to 1, respectively. The normalization of layers using fuzzy membership functions causes the range of changes of all layers to change between zero and one, and the layers become dimensionless. Based on this process, an arbitrary pixel in a layer takes a value between 0 and 1 according to the characteristics of the same layer. While the equivalent of this process is in the Basic GALDIT framework, classification is based on recommended rates, and the number of classes is determined based on expert judgments.

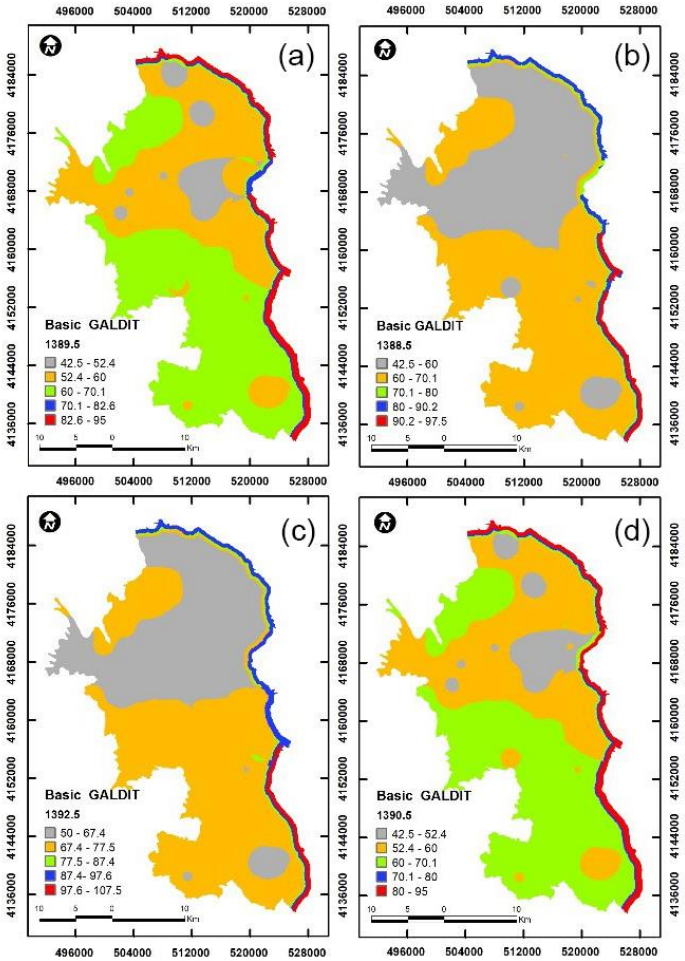


Figure 5. Spatial distribution of vulnerability index based on Basic GALDIT framework and time changes: (a) August 2009, (b) August 2010, (c) August 2011, (d) August 2012

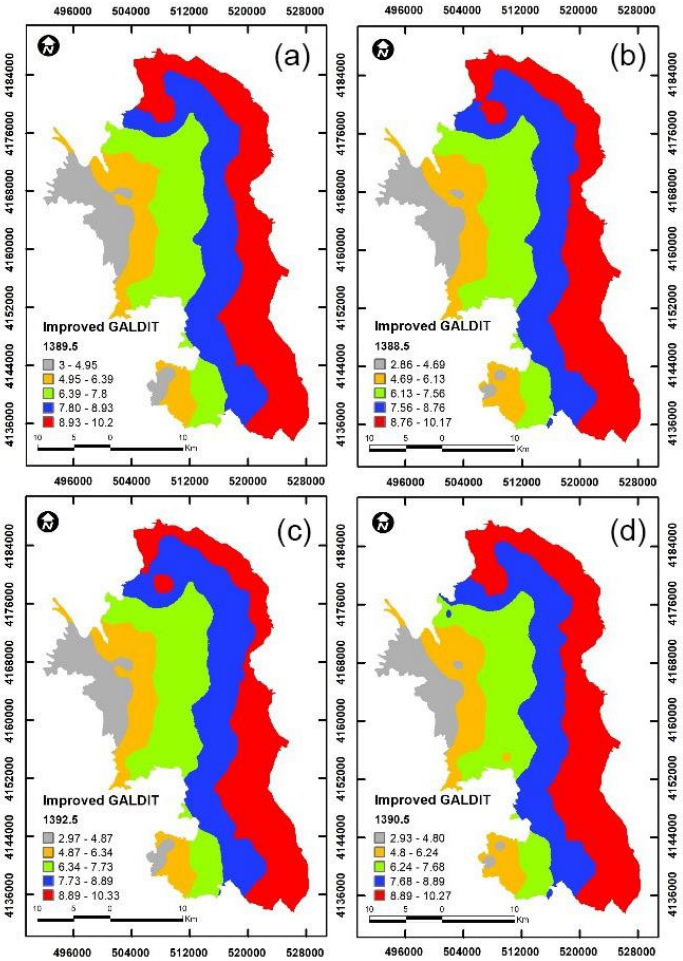


Figure 6. Spatial distribution of vulnerability index based on modified GALDIT framework and time changes: (a) August 2009, (b) August 2010, (c) August 2011, (d) August 2012

The revised GALDIT index was calculated using the relative importance of the layers by the weights presented in Table 2 and the normalized layers by the fuzzy membership functions and its results for August 2009, 2010, 2011, and 2012 are shown in Fig. 6. Considering this figure, it can be seen that the temporal changes of GALDIT dynamic layers (L and I layers) do not have a significant effect on the final result of vulnerability. Of course, this issue may not be true in other aquifers. It can also be seen that the vulnerability index increases as you get closer to the coastline. A comparison of Figure 6 and Figure 6 shows that, unlike the Basic GALDIT framework, the modified method did not provide conservative results and a significant area near the coastline has a high vulnerability index.

4. Conclusion

Fresh water stored in coastal aquifers is exposed to salinity due to its proximity to saltwater, the high demand for water, and the high population density. The salinity of groundwater sources is considered one of the main sources of pollution that threatens groundwater sources. Therefore, to protect groundwater resources in coastal areas, the intrusion of saltwater should be prevented and the management of these aquifers should be done effectively. Assessing the vulnerability of

coastal aquifers to saltwater intrusion is considered a tool to prevent groundwater salinization. The GALDIT framework has been widely used to assess the vulnerability of saltwater intrusion in coastal aquifers. The GALDIT framework is an indexing technique that includes the following six layers, which include the type of aquifer (G), hydraulic conductivity of the aquifer (A), groundwater level above sea level (L), distance from the coast (D), impact the existing state of seawater (I) and the thickness of the aquifer (T).

In this study, the vulnerability of saltwater intrusion in the Urmia Plain aquifer has been evaluated. For this purpose, the GALDIT framework, which is one of the common methods for evaluating saltwater intrusion in coastal aquifers, has been used. The results showed that the GALDIT framework provides conservative results. So the vulnerability is high in narrow areas near the coastline and most of the plain (about 90%) is in the range of low to medium vulnerability, which is not compatible with the reality of the plain. Therefore, based on the evaluations, it was determined that the reason for the presentation of conservative results by the GALDIT framework is the existence of pre-defined rates. To resolve this limitation, instead of assigning these rates, fuzzy membership functions that normalize the layers between zero and one have been used.

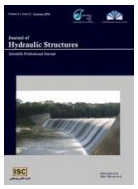
References

1. Barker, AP, Newton, RJ, Bottrell, SH, Tellam, JH, (1998). Processes affecting groundwater chemistry in a zone of saline intrusion into an urban sandstone aquifer. Applied Geochemistry, pp: 13:735-749.
2. Barlow, PM, Reichard, EG, (2010). Saltwater intrusion in coastal regions of North America. Hydrogeology Journal, pp:18:247-260.
3. Jayasekera, DL, Kaluarachchi, JJ, Villholth, KG, (2011). Groundwater stress and vulnerability in rural coastal aquifers under competing demands: a case study from Sri Lanka. Environmental monitoring and assessment, pp: 176:13-30.
4. Huan, H, Wang, J, Teng, Y, (2012). Assessment and validation of groundwater vulnerability to nitrate based on a modified DRASTIC model: a case study in Jilin City of northeast China. Science of the Total Environment, pp: 440:14-23.
5. Chachadi, AG, Lobo-Ferreira, JP, (2007). Assessing aquifer vulnerability to seawater intrusion using GALDIT framework: part 2, GALDIT indicators description. Water Celt Countries Quant. Qual Clim. Pp: pp:310:172–180.
6. Pedreira, R, Kallioras, A, Pliakas, F, Gkiougkis, I, Schuth, C, (2015). Groundwater vulnerability assessment of a coastal aquifer system at River Nestos eastern Delta, Greece. Environmental earth sciences, pp: 73:6387-6415.
7. Recinos, N, Kallioras, A, Pliakas, F, Schuth, C, (2015). Application of GALDIT index to assess the intrinsic vulnerability to seawater intrusion of coastal granular aquifers. Environmental earth sciences, pp: 73: 1017-1032.
8. Luoma, S, Okkonen, J, Korkka-Niemi, K, (2017). Comparison of the AVI, modified SINTACS and GALDIT vulnerability methods under future climate-change scenarios for a shallow low-lying coastal aquifer in southern Finland. Hydrogeology Journal, pp: 25: 203-222.
9. Mahesha, A, Vyshali, Lathashri, UA, Ramesh, H, (2011). Parameter estimation and vulnerability assessment of coastal unconfined aquifer to saltwater intrusion. Journal of Hydrologic Engineering, pp: 17: 933-943.

10. Gorgji, AD, Moghadam, AA, (2016). Vulnerability Assessment of saltwater intrusion using simplified GAPDIT method: a case study of Azarshahr Plain Aquifer, East Azerbaijan, Iran. Arabian Journal of Geosciences, pp: 9:106.
11. Klassen, J, and Allen, DM, (2017). Assessing the risk of saltwater intrusion in coastal aquifers. Journal of hydrology, pp: *551*: 730-745.
12. Sophiya, M. S, Syed, TH, (2013). Assessment of vulnerability to seawater intrusion and potential remediation measures for coastal aquifers: a case study from eastern India. Environmental earth sciences, pp: 70:1197-1209.
13. Kura, NU, Ramli, MF, Ibrahim, S, Sulaiman, WNA, Aris, AZ, Tanko, AI, Zaudi, MA, (2015). Assessment of groundwater vulnerability to anthropogenic pollution and seawater intrusion in a small tropical island using index-based methods. Environmental Science and Pollution Research, pp: 22: 1512-1533.
14. Bouderbala, A, Remini, B, Hamoudi, AS, Pulido-Bosch, A, (2016). Assessment of groundwater vulnerability and quality in coastal aquifers: a case study (Tipaza, North Algeria). Arabian Journal of Geosciences, pp:9:181.
15. Najib, S, Fadili, A, Mehdi, K, Riss, J, Makan, A, Guessir, H, (2016). Salinization process and coastal groundwater quality in Chaouia, Morocco. Journal of African Earth Sciences, pp: 115: 17-31.
16. Allouche, N, Maanan, M, Gontara, M, Rollo, N, Jmal, I, Bouri, S, (2017). A global risk approach to assessing groundwater vulnerability. Environmental modelling & software, pp: 88:168-182.
17. Motevalli, A, Moradi, HR, Javadi, S, (2018). A Comprehensive evaluation of groundwater vulnerability to saltwater up-coning and sea water intrusion in a coastal aquifer (case study: Ghaemshahr-juybar aquifer). Journal of Hydrology, pp: 557:753-773.
18. Chachadi, AG, Lobo Ferreira, JPC, (2001). Sea water intrusion vulnerability mapping of aquifers using the GALDIT framework. Coastin, pp: 4:7-9.
19. Amirataee, B, Zeinalzadeh, K, (2016), Trends analysis of quantitative and qualitative changes in groundwater with considering the autocorrelation coefficients in west of Lake Urmia, Iran. Environmental Earth Sciences, pp: 75(5):371.

© 2024 by the authors. Licensee SCU, Ahvaz, Iran. This article is an open access article distributed under the terms and conditions of the Creative Commons Attribution 4.0 International (CC BY 4.0 license) (http://creativecommons.org/licenses/by/4.0/).

Journal of Hydraulic Structures
J. Hydraul. Struct., 2024; 10(1):106-118
DOI: 10.22055/jhs.2024.19077



OPEN ACCESS

Numerical investigation on the hydraulic parameters' effects on the circular-crested weir

Mahdi Majedi Asl [*1]
Hadi Arvanaghi [2]
Mehdi Fuladipanah [3]
Omid Ghasemzadeh [1]
Tohid Omidpour Alavian [1]

Abstract

A paramount determinant in the selection of irrigation canal overflow configurations resides in their flow conveyance capacity. This overflow capacity is contingent upon the effective length and geometric characteristics of the weir. In the present investigation, the hydraulic performance and discharge coefficient (C_d) of circular-crested weir were scrutinized through the utilization of FLUENT software. Specifically, the study delved into the impact of geometric parameters, namely the radius and height of the crest, on these hydraulic aspects. Following the execution of calibration and validation procedures using FLUENT in conjunction with laboratory-derived data, the outcomes of the simulation revealed that augmenting the radius of the crest led to a corresponding escalation of 144.28% in the maximum pressure exerted on the crest and a 6.84% increase in flow depth. Conversely, the maximum velocity and C_d experienced reductions of 6.84% and 7.82%, respectively. The elevation of the weir height exhibited negligible influence on the maximum pressure magnitude at the crest. Contrastingly, a reduction in weir height constricted the range of pressure variations on the crest, indicating a more limited domain of pressure changes. Elevating the weir height induces a notable augmentation in the maximum flow velocity at the crest by 44.36%, concomitant with a reduction in both the depth and C_d by 52.66% and 68.96%, respectively.

Keywords: Weir Height, Circular Crest Weir, Crest Radius, Discharge Coefficient, Numerical Model.

Received: 09 November 2023; Accepted: 16 April 2024

[*] Email: mehdi.majedi@gmail.com **(Corresponding Author)**
[1] Department of Civil Engineering, Faculty of Engineering, University of Maragheh, Maragheh. Iran.
[2] Department of Water Sciences and Engineering, Tabriz University, Tabriz, Iran.
[3] Department of Civil engineering, Ramhormoz Branch, Islamic Azad University, Ramhormoz, Iran.

CC BY

1. Introduction

In presenting solutions for hydraulic issues, understanding the behavior of problem-causing phenomena plays a crucial role in addressing and controlling them. One of the longstanding challenges that humanity grapples with is the issue of water scarcity. Acquiring knowledge and examining hydraulic issues, as well as understanding the behavior of water flow, greatly aids engineers in the precise design and implementation of projects in contributing to measuring flow, reducing water losses, and enhancing water resource preservation and protection. The structures for measuring and controlling flow are among the most critical components of irrigation and drainage networks. Measuring the volume of flow is vital for agricultural purposes and irrigation projects. Therefore, various methods are employed to measure the flow rate in open channels. One of the primary structures for flow measurement in open channels is the weir, utilized for the passage of water flow from the upstream to the downstream of the channel. One key consideration in selecting the type of weir is its capacity. Since the weir capacity is a function of the effective crest length and geometric shape, extensive studies have been conducted in this regard. Weirs with circular and cylindrical crests find application in the measurement, conveyance, and passing of flow in irrigation networks and water convenience systems, as their design significantly influences the weir capacity. Heidarpour and Chamani (2006) proposed an analytical model based on the non-rotational and non-viscous flow equations to predict the discharge coefficient and velocity profile. It was evaluated using experimental results, demonstrating a good agreement between the model outcomes and experimental data. They concluded that the flow over a circular-crested weir can be treated similarly to non-rotational and non-viscous flow around a cylinder. Heidarpour et al. (2008) investigated the hydraulic of the flow over a semi-circular cylinder weir and provided accurate relationships for velocity distribution on the weir crest and the pressure correction coefficient. Bagheri and Heidarpour (2010) utilized Euler's equations to determine the Cd of flow over circular-crested weir models with varying heights and radius. Their results demonstrated that the proposed relationship for estimating the Cd could be effectively generalized for different parameters of circular-crested weirs. Using the potential flow theory and applying the velocity correction coefficient in the weir crest section, they derived analytical relationships for the Cd and velocity and pressure profiles on the crest of circular-crested weirs. Shabanlou et al. (2013) examined experimentally the influence of the upstream wall slope angle on the Cd and the amount of energy loss in the flow over circular-crested weirs. Their results indicated that the upstream slope has a negligible effect on the Cd and energy dissipation. Moreover, an increase in the upstream slope angle led to a more uniform velocity distribution in the vicinity of the weir crest. Kabiri Samani and Bagheri (2014) conducted an investigation on the hydraulic of the flow over circular-crested weirs to determine the Cd and velocity distribution. According to their findings, inertial forces cause the deflection of flow lines over the circular-crested weir. Mohammadzadeh-Habili et al. (2016) examined the characteristics of flow over a wide-lipped weir with flat and quarter-circle crests. Their results revealed that the flow lines pass parallel to the crest through the wide edge of the flat-crested weir to downstream. Flow separation occurs at the beginning of the crest, leading to a potential for cavitation in this area. By introducing a quarter-circle crest and inducing curvature in the flow lines, the separation is significantly controlled, eliminating the risk of cavitation. Additionally, the Cd increases in this configuration. Haghiabi et al. (2018) investigated the velocity distribution and Cd of flow over cylindrical weirs. Through a series of experiments, they presented relationships for determining the Cd and velocity distribution in the vicinity of the weir crest. Tullis et al. (2019) conducted experiments on semi-circular and quarter-circular crested weirs with varying flow rates to examine the effect of crest shape on the Cd. The magnitude of discharge variations in the semi-circular crested weir was found to be less than that

in the quarter-circular configuration. Chanson (2020), in a study on the characteristics and stability of flow over circular weirs, observed fluctuations in the water surface during the downstream transition and separation from the weir surface, resulting in some negative pressures at these points. Consequently, it was suggested to implement aeration near the downstream region of this type of weir. Parsaie and Haghiabi (2021) endeavored to establish relationships for determining the Cd of flow over circular-crested weirs using Monte Carlo methods. Their proposed relationships, after validation with experimental data, demonstrated high accuracy in estimating the Cd of flow over weirs. In a subsequent study, Parsaie et al. (2022) investigated the impact of the Cd on the ratio of upstream flow height to weir crest radius through both experimental and numerical simulation using FLOW-3D software. Their findings reported that an increase in flow velocity leads to a reduction in pressure when the flow is high. Omidpour Alavian et al. (2022) modeled and evaluated the discharge coefficient of arched labyrinth weirs. Omidpour Alavian et al. (2022) compared the hydraulic efficiency of labyrinth weirs with quarter-circle and semi-circle crest shapes. Majedi et al. (2023) investigated the hydraulic efficiency of labyrinth weirs with quarter-circle and semi-circle crest shape. Majedi et al. (2023) compared the hydraulic efficiency of labyrinth weirs with artificial intelligence methods. In the present study, numerical simulation of circular-crested weirs has been employed to investigate the geometric effects, including the crest diameter and weir height, on the Cd of circular-crested weirs under various hydraulic conditions.

2. Materials and methods

2.1. Governing equations

The Navier-Stokes equations are the governing equations for fluid motion, adhering to the principles of momentum conservation and mass continuity for moving fluids. These equations are expressed as follows:

$$\frac{\partial \overline{u_t}}{\partial X_i} = 0 \tag{1}$$

$$\frac{\partial \overline{u_t}}{\partial t} + \bar{u}_j \frac{\partial \overline{u_t}}{\partial X_j} = -\frac{1}{\rho}\frac{\partial \bar{p}}{\partial X_i} + g x_i + \frac{\partial}{\partial x_i}\left(\vartheta \frac{\partial \overline{u_t}}{\partial x_j} - \overline{u_t u_j}\right) \tag{2}$$

Here u represents the flow velocity in the horizontal axis, motion in the horizontal (i) and vertical (j) directions. v represents the velocity in the vertical axis, ρ is the fluid density, g is the gravitational acceleration, and $\overline{P}$ denotes the corrected fluid pressure at various points, calculated as follows:

$$\overline{P}=P+2\rho k/3 \tag{3}$$

The fluid kinetic energy (k), the rate of kinetic energy dissipation (E), and the fluid viscosity (μ) are also calculated using equations (4), (5), and (6):

$$\frac{\partial(\rho k)}{\partial t}+\frac{\partial(u_i k)}{\partial x_i}=\frac{\partial}{\partial x_i}\left[\left(\mu+\frac{\mu_t}{\sigma_k}\right)\frac{\partial k}{\partial x_i}\right]+G+\varepsilon\rho \tag{4}$$

$$\frac{\partial(\rho\varepsilon)}{\partial t}+\frac{\partial(u_i \varepsilon)}{\partial x_i}=\frac{\partial}{\partial x_i}\left[\left(\mu+\frac{\mu_t}{\sigma_\varepsilon}\right)\frac{\partial \varepsilon}{\partial x_i}\right]+C_{1_s}\frac{\varepsilon}{k}G-C_{2_s}\rho\frac{\varepsilon^2}{k} \tag{5}$$

$$\mu_t=\rho C_\mu \frac{k^2}{\varepsilon} \tag{6}$$

2.2. Dimensional analysis

Fig. 1 illustrates the effective parameters affecting the Cd of flow over circular-crested weirs. In this figure, w represents the weir height, R is the weir crest radius, α is the upstream face slope angle, β is the downstream face slope angle, Q is the Cd, and H_1 denotes the head over the upstream energy line. Table 1 presents the hydraulic and geometric characteristics of the models.

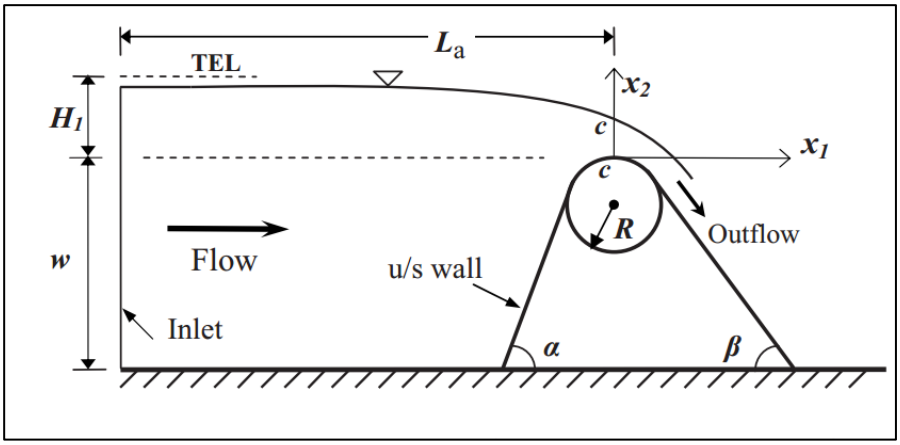


Figure 1. Schematic view of the circular-crest weir

The Cd of circular-crested weirs can be derived from the general relationship for rectangular weirs as following:

$$Q=\frac{2}{3}C_d\sqrt{2g}LH_1^{1.5} \quad (7)$$

$$C_d\frac{1.5Q}{\sqrt{2g}LH_1^{1.5}} \quad (8)$$

Herer Q represents the discharge flow rate, L is the width of the circular-crested weir, and g is the acceleration due to gravity. The relationship between the parameters influencing the Cd in the free-flow condition can be expressed as follows:

$$C_d=f(R, w, H_1, \sigma, q, g, \alpha, \beta, \rho, \mu) \quad (9)$$

By performing dimensional analysis and the Pi-Buckingham method, the dimensionless parameters are obtained as follows:

$$C_d=f(\frac{H_1}{w}, \frac{H_1}{R}, Fr, Re, We, \alpha, \beta) \quad (10)$$

Where Fr represents the Froude number, Re denotes the Reynolds number, and We stands for the Weber number. Considering that the minimum flow depth over the weir crest is greater than 0.04 meters, the influence of surface tension on the flow can be neglected. Additionally, assuming turbulent flow with Re > 10000, the viscous effects can be disregarded. Moreover, Fr is less than one in the upstream of the weir, and its variation range is small, indicating a subcritical flow regime, allowing for the neglect of its influence. Therefore, the dimensionless parameters influencing the Cd are summarized as follows.

$$C_d = f\left(\frac{H_1}{w}, \frac{H_1}{R}, \alpha, \beta\right) \quad (11)$$

Table 1. Geometry properties of the present research

Model	Weir height (m)	Weir radius (m)	Upstream slope angle	Downstream slope angle
CW1	1.16	0.15	90	90
CW2	1.16	0.15	45	45
CW3	1.16	0.20	45	45
CW4	1.16	0.10	45	45
CW5	1.50	0.15	45	45
CW6	0.60	0.15	45	45

2.3. choosing optimum mesh, turbulent model and boundary conditions

Fig. 2 depicts the schematic model along with boundary conditions. The boundary conditions of input velocity include Velocity Inlet, Pressure Inlet for air input, Pressure Outlet for the fluid surface and outlet, and a Wall condition for the flow domain walls along with the weir model. A triangular mesh is employed for model discretization, and meshes with 17586, 21560, 28842, and 34959 elements were selected for sensitivity analysis and grid independence. The obtained results are presented in Fig. 3. In this section, three turbulence models, namely k-ε (Standard), k-ε (RNG), and k-ω, were selected for the accuracy evaluation of the turbulence model. The results obtained from the water surface profile passing over the weir crest and the velocity distribution profile at the crest were compared numerically with the experimental results of Vo (1992), as shown in Fig. 4.

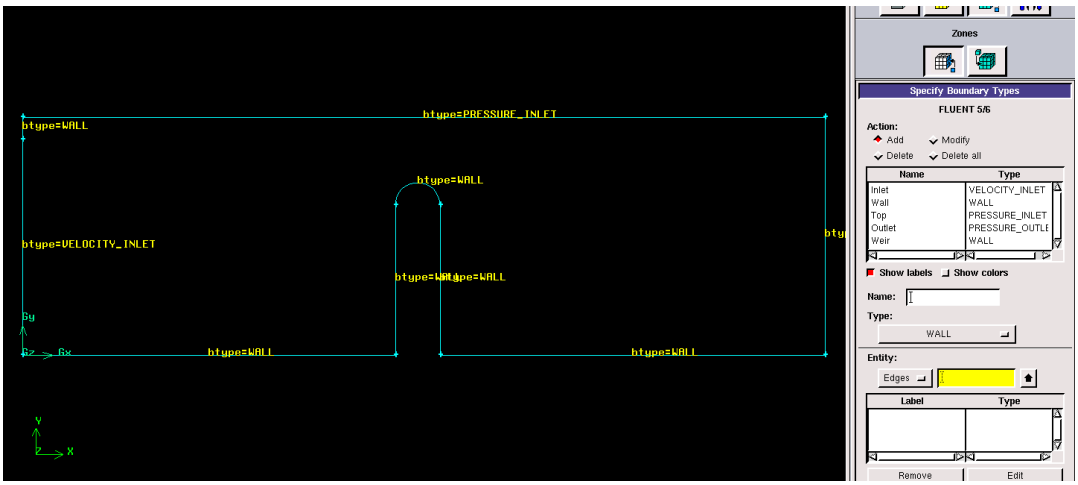


Figure 2. The definition of boundary conditions

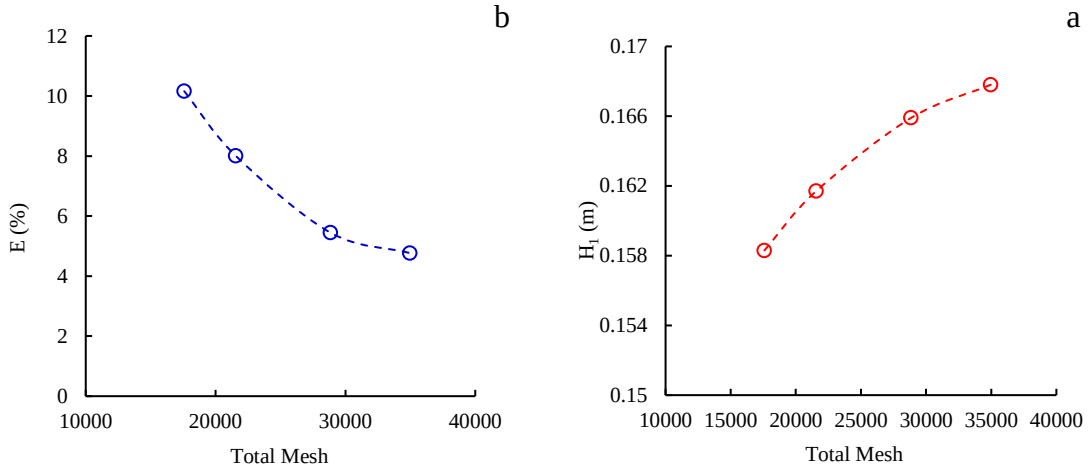


Figure 3. Optimum mesh of included models in the research

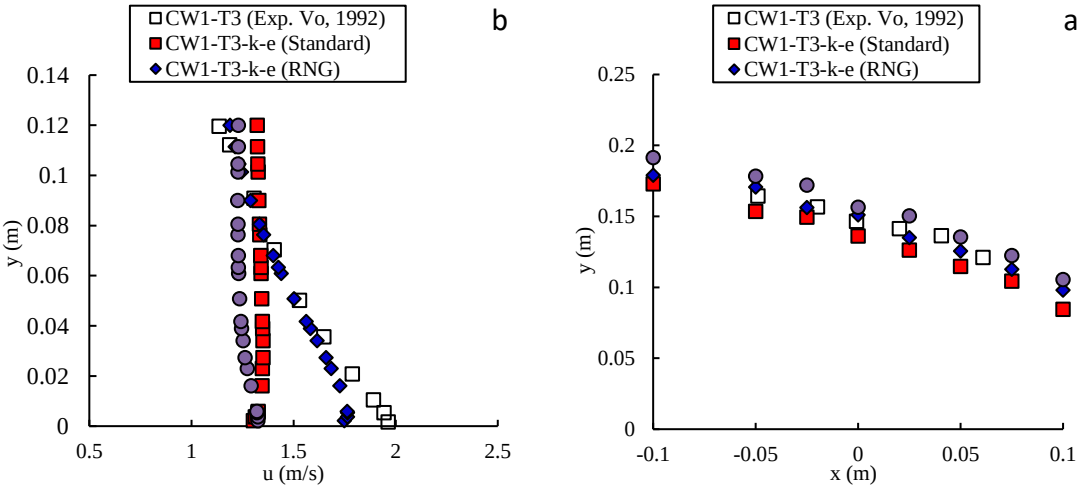


Figure 4. Comparison of (a) velocity vertical profile (b) water surface profile for included turbulent models

3. Results and discussion

The results for the optimized mesh are presented in Fig. 3. As observed, increasing in the mech number leads to a reduction in relative error percentage (E%). However, the difference in results between meshes of number 28842 and 34959 is nearly negligible. It can be concluded that the influence of the mesh size on the accuracy of the software is almost insignificant. By increasing the mesh number from 28842 to 34959, the difference in water height over the crest changes from 0.1659 to 0.1678 meters (less than 1%). Therefore, the mesh with 34959 elements can be considered as the optimal mesh. With 34959 elements, 35462 node number is corresponding to the 34959 mesh number. Referring to Fig. 4 (a and b), the results for the water surface profile and the velocity distribution over the weir crest simulation are presented. As observed, the numerical results for the water surface profile are close to the experimental results for almost all turbulence models. However, the RNG turbulence model shows better accuracy compared to the others. Additionally, by comparing the results for the velocity distribution profile, it can be observed a

slight difference between the results from the RNG turbulence model and the experimental results. Nevertheless, there is a significant difference in velocity results between the other two turbulence models and the experimental data. Table 2 presents the results of numerical simulation for various turbulence models along with the error percentage compared to experimental results. Upon careful examination of the mentioned table, it can be observed that the RNG turbulence model exhibits higher accuracy compared to the other turbulence models. On average, the relative percentage errors for k-ε (Standard), k-ε (RNG), and k-ω models for the water surface profile results are 7.62%, 3.73%, and 6.96%, respectively. Those of the velocity distribution are 15.28%, 3.55%, and 15.51%. Therefore, considering the superior output accuracy of the RNG turbulence model, it was chosen as the basis for further modeling.

Table 2. A comparison between water surface and velocity profile for turbulent models included

E-u (%)	E-h (%)	Experimental value u (m/s)	Numerical value u (m/s)	Experimental value h (m)	Numerical value h (m)	Turbulent model
31.78	0.84	1.943	1.325	0.174	0.173	
18.08	6.62	1.648	1.349	0.164	0.153	
12.05	4.61	1.528	1.344	0.156	0.149	
1.80	6.98	1.306	1.329	0.146	0.136	k-ε (Standard)
11.54	10.75	1.187	1.324	0.141	0.126	
16.42	15.94	1.135	1.321	0.136	0.114	
15.28	7.62		Mean value of relative error			
9.24	2.59	1.943	1.763	0.174	0.179	
1.97	3.92	1.648	1.615	0.164	0.171	
1.77	0.37	1.528	1.501	0.156	0.156	
1.37	3.09	1.306	1.288	0.146	0.151	k-ε (RNG)
2.25	4.48	1.187	1.213	0.141	0.135	
4.70	7.91	1.135	1.188	0.136	0.125	
3.55	3.73		Mean value of relative error			
32.01	9.75	1.943	1.321	0.174	0.191	
23.92	8.50	1.648	1.253	0.164	0.178	
19.21	9.81	1.528	1.234	0.156	0.172	
6.07	6.75	1.306	1.226	0.146	0.156	k-ω
3.54	6.35	1.187	1.230	0.141	0.150	
8.32	0.62	1.135	1.229	0.136	0.135	
15.51	6.96		Mean value of relative error			

Fig. 5 presents the results of pressure and velocity curve variations for different radii of the weir crest, including 0.1, 0.15, and 0.20 meters, with a fixed upstream and downstream slope angle (α=b=45°). It can be observed that with an increase in the weir crest radius, the pressure values on the weir crest also increase. Additionally, the pressure range on the weir crest decreases with an increase in the crest radius. For a radius of 0.1 meters, the pressure range on the weir crest is between -0.03 to 0.021 meters, whereas for radii 0.15 and 0.2 meters, it varies between 0.012 to 0.032 and 0.041 to 0.045 meters, respectively. Furthermore, the maximum pressure on the weir crest is observed to be higher for larger radii. The maximum pressure values for weir crest radii of 0.1, 0.15, and 0.2 meters are 0.021, 0.032, and 0.045 meters, respectively. Therefore, the maximum pressure on the weir crest increases by 114.28% with a twofold increase in the weir crest radius. As observed in Fig. 5-b, the velocity on the weir crest decreases with an increase in the crest radius. The reduction in velocity with an increase in the crest radius is more pronounced near the weir crest than in the flow region. The maximum velocity values for weir crest radii of 0.1, 0.15, and 0.2 meters are 2 1.77, and 1.68 meters per second, respectively. Hence, the maximum velocity on the weir crest decreases by 19.04% with a twofold increase in the weir crest radius, as depicted in Fig. 6. It is evident in Fig. 6 that the range of velocity variations on the weir crest is higher for smaller radii compared to other models.

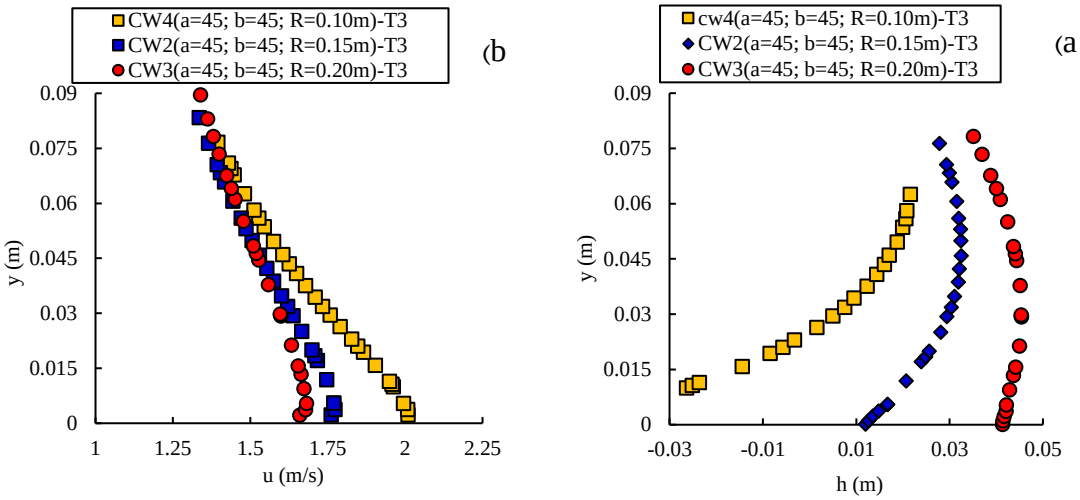


Figure 5. The effect of radius of the circular-crested weir on the (a) pressure and (b) velocity

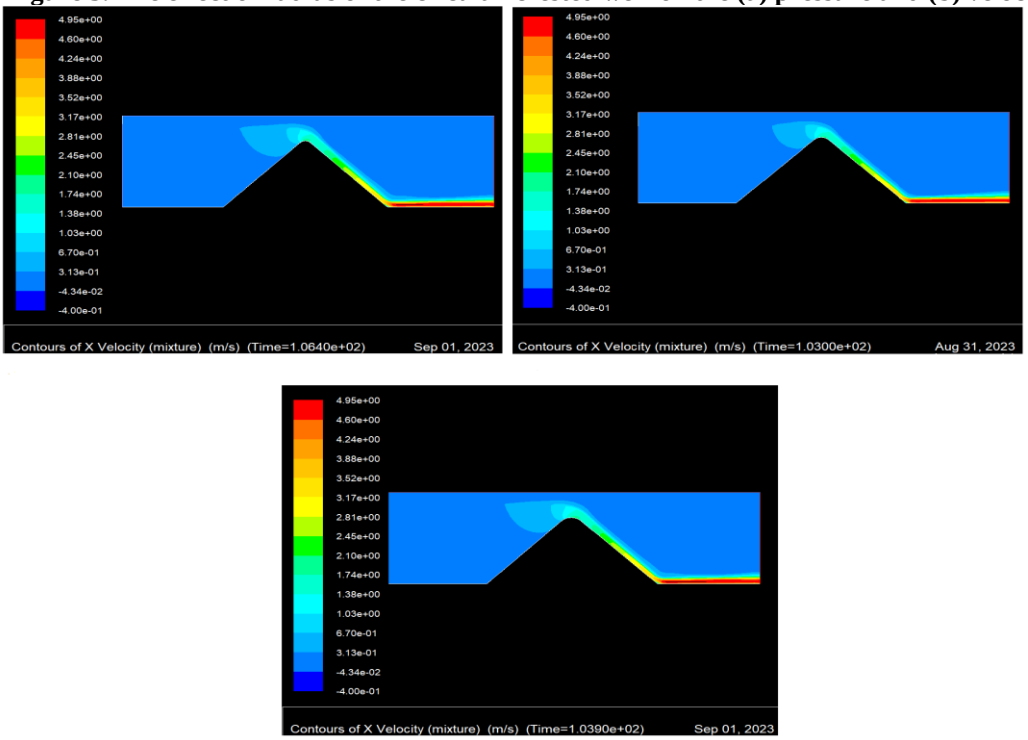


Figure 6. Flow velocity passing through circular-crested weir of radii 0.1, 0.15 and 0.2 m

Fig. 7 presents the flow surface profiles for different weir crest radii of circular-crested weir models. It is observed that with an increase in the weir crest radius, the height of the flow surface profile on the weir crest increases. In other words, as the weir crest radius decreases, the depth of the flow on the weir crest decreases. On average, with a decrease in the weir crest radius from 0.2 meters to 0.1 meters, the depth of the flow on the weir crest decreases by 6.84%.

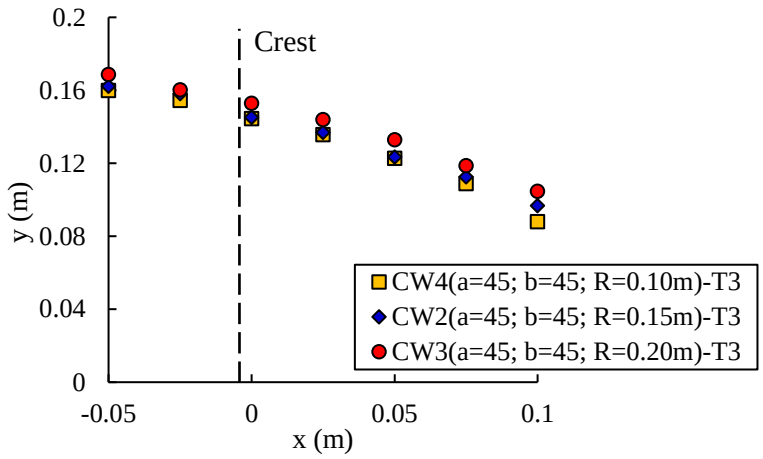


Figure 7. The effect of crest radius on the water surface profile

Fig. 8 shows the flow surface profiles for different weir crest radii for circular-crested weir models. According to this graph, an increase in the weir crest radius leads to an increase in the height of the flow surface profile on the weir crest. In other words, a decrease in the weir crest radius is equivalent to a reduction in the depth of the flow on the weir crest. On average, with a decrease in the weir crest radius from 0.20 meters to 0.1 meters, the depth of the flow on the weir crest decreases by 6.84%.

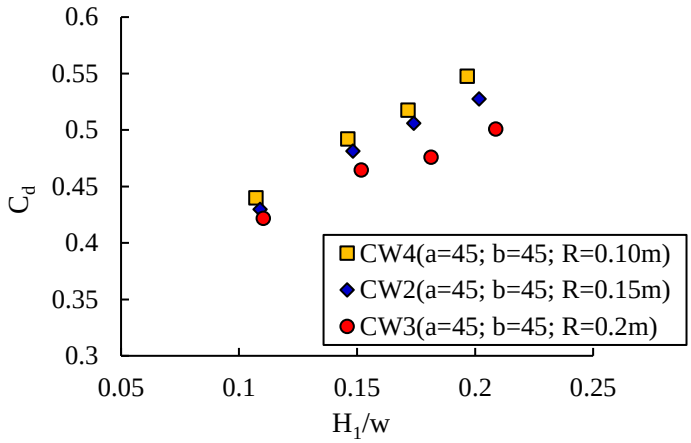


Figure 8. The variation of Cd vs. H1/W for various radii

In Fig. 9, the results of pressure and velocity curve variations are presented for different weir heights, including 0.6, 1.16 and 1.5 meters, considering a fixed upstream and downstream slope angle (α=β=45°). It is observed that the trend of the pressure distribution curve on the weir crest changes with the variation of weir height. Increasing the weir height leads to the expansion of the pressure distribution range on the weir crest, and as the weir height decreases, the range of pressure values on the crest becomes more limited. For instance, for a height of 0.6 meters, the pressure range on the crest is between -0.032 to 0.017 meters, while for heights of 1.61 and 0.5 meters, it ranges from 0.012 to 0.032 and -0.016 to 0.032 meters, respectively. The maximum pressure values on the weir crest are nearly identical for all three different weir heights, as shown in Fig. 9-

b. Additionally, the velocity on the weir crest increases with the rise in weir height, and the increase in velocity with the increase in weir height near the weir crest is more significant than the flow surface. The maximum velocity values for weir heights of 0.6, 1.61, and 1.5 meters are 1.42, 1.77 and 2.05 meters per second, respectively. Consequently, the maximum velocity on the weir crest increases by 44.36% with a two-and-a-half-fold increase in weir height. In Fig. 10, it is observed that the range of velocity variations on the weir crest and downstream is greater for larger weir heights compared to other models.

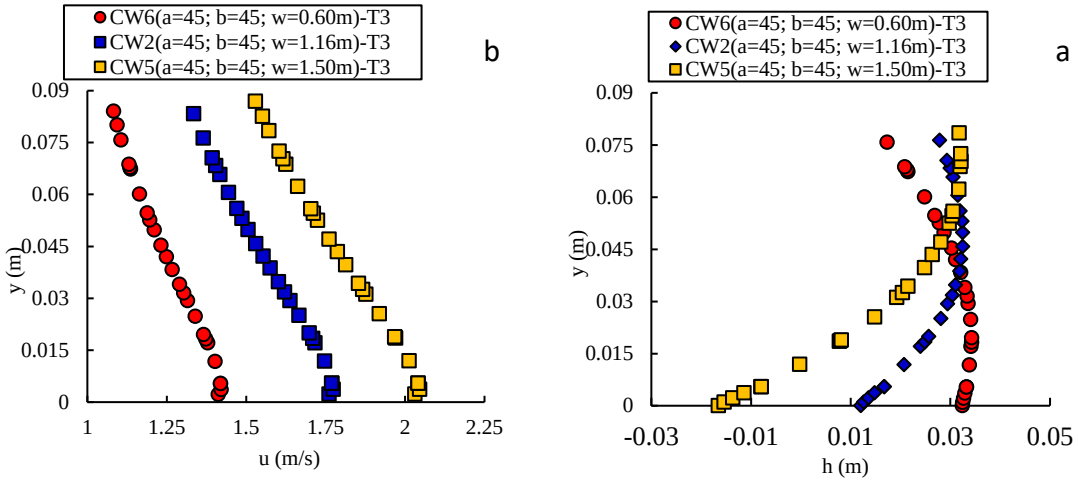


Figure 9. The effect of the weir height on the (a) pressure (b) velocity distribution

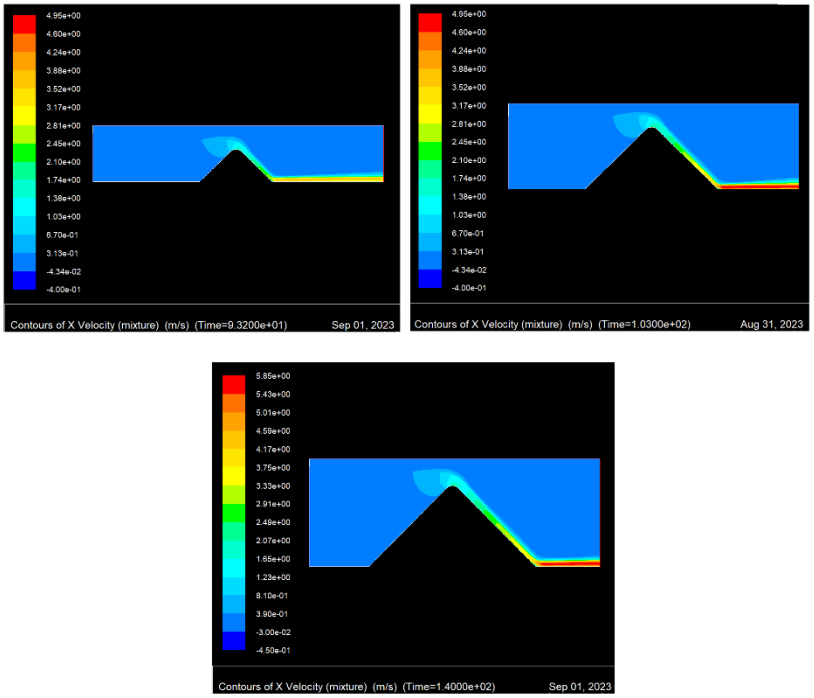


Figure 10. The passing flow velocity counter through circular-crested weir of heights 0.6, 1.16 and 1.5

Fig. 11 reveals the profiles of the flow surface over the weir crest for different weir heights. It is observed that with an increase in weir height, the height of the flow surface profile over the weir crest also increases. In other words, as the weir height decreases, the depth of the flow over the weir crest decreases. On average, with a decrease in weir height from 1.5 meters to 0.6 meters, the depth of the flow over the weir crest decreases by 52.66 %.

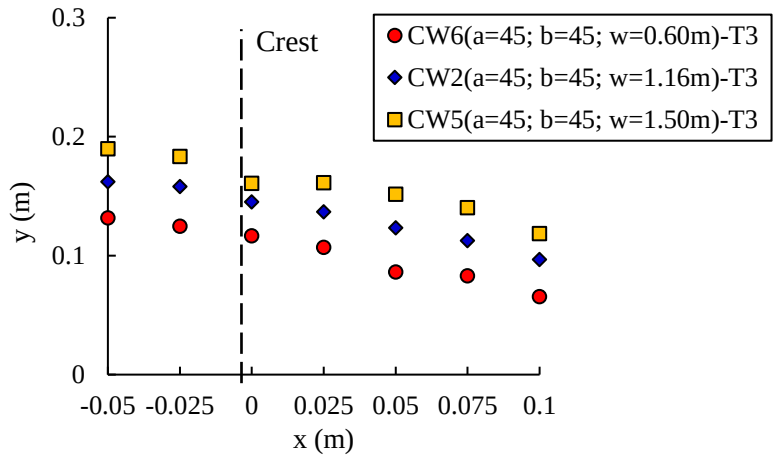


Figure 11. The effect of the weir height on the water surface profile passing through the crest

Fig. 12 illustrates the variations of the C_d for flow over circular-crested weir models with respect to weir height. It is observed that, in all models, the C_d increases with an increase in H_1/R. The main difference lies in the slope of the increasing trend of the C_d with the increase in H_1/R at different weir heights. In other words, the increasing trend of the C_d becomes steeper with a decrease in weir height. With an increase in weir height, the Cd decreases due to the increased flow depth upstream of the weir. On average, an increase in weir height from 0.6 meters to 1.50 meters results in a 68.96% reduction in the C_d.

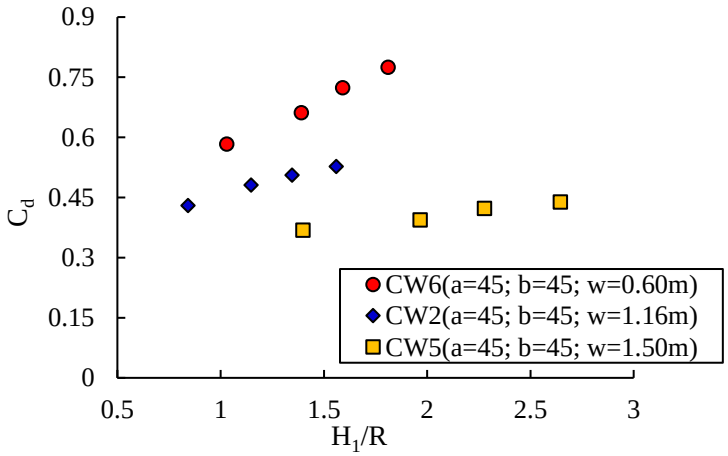


Figure 12. The variation of C_d vs. H_1/R of various weir height

4. Conclusion

This research investigates the influence of geometric parameters of circular-crested weirs, including weir's radius and height on the flow characteristics, such as pressure and velocity distribution on the crest, flow profile and Cd. Three turbulence models, namely k-ε (Standard), k-ε (RNG), and k-ω, were opted for evaluating the accuracy of the turbulence model. The results of the surface profile and depth-averaged velocity distribution from the numerical simulation of flow over the circular-crested weir were compared with experimental results. The k-ε (RNG) turbulence model exhibited higher accuracy compared to the other turbulence models. The findings indicate that:

- With a raise in the weir crest radius, the pressure values on the weir crest increase.
- The pressure range on the weir crest decreases with an increase in the weir crest radius.
- The velocity on the weir crest decreases with an growth in the crest radius.
- The velocity reduction with an increase in the crest radius is more pronounced in the vicinity of the weir crest than in the flow surface.
- By reducing the weir crest radius, the depth of the flow on the weir crest declines. On average, with a decrease in the weir crest radius from 0.2 meters to 0.1 meters, the depth of the flow on the weir crest decreases by 6.84 percent.
- With an increase in the weir crest radius, the Cd decreases. The decrease in the Cd is more noticeable in higher values of H1/w.
- On average, increasing the weir crest radius from 0.1 meters to 0.2 meters results in a 7.82 percent decrease in the Cd.

Increasing the weir crest height results in the expansion of the pressure distribution range on the crest. As the crest height decreases, the range of pressure values becomes more restricted. The maximum pressure on the crest is the same for all three different crest heights, while the velocity on the crest increases with an amplification in crest height. The velocity raise is more pronounced near the crest compared to the flow surface.

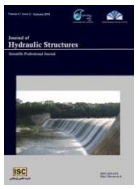
References

1. Heidarpour, M., Chamani, M. R. (2006). Velocity distribution over cylindrical weirs, Journal of Hydraulic Research, 44, 5, 708- 711.
2. Heidarpour, M., Habili, J. M., Haghiabi, A. H. (2008). Application of potential flow to circular-crested weir. Journal of hydraulic research, 46(5), 699-702.
3. Bagheri, S., Heidarpour, M. (2010). Overflow characteristics of circular-crested weirs. Journal of Hydraulic Research, 48(4), 515- 520.
4. Shabanlou, S., Khorami, E., Rajabi, A. (2013). The effects of various upstream arches of crest of the circular crested weir on hydraulic parameters. Flow Measurement and Instrumentation, 32, 103-106.
5. Kabiri-Samani, A., Bagheri, S. (2014). Discharge coefficient of circular-crested weirs based on a combination of flow around a cylinder and circulation. Journal of Irrigation and Drainage Engineering, 140(5), 04014010.
6. Mohammadzadeh-Habili, J., Heidarpour, M., Haghiabi, A. (2016). Comparison the hydraulic characteristics of finite crest length weir with quarter-circular crested weir. Flow Measurement and Instrumentation, 52, 77-82.
7. Haghiabi, A. H., Mohammadzadeh-Habili, J., Parsaie, A. (2018). Development of an evaluation method for velocity distribution over cylindrical weirs using doublet concept. Flow Measurement and Instrumentation, 61, 79-83.

8. Tullis, B. P., Crookston, B., Bung, D. (2019). Weir head-discharge relationships: A multi-lab exercise. E-proceedings of the 38th IAHR World Congress, Panama City, Panama, 1-15.
9. Chanson, H., and Montes, J. S. (1997). Overflow characteristics of cylindrical weirs. Res. Rep. No. CE 154, Dept. of Civil Engineering, University of Queensland, Brisbane, Australia.
10. Parsaie, A., Jaafer Suleiman Shreef, S., Haghiabi, A. H., Hoobi Irzooki, R., Khalaf, R. M. (2022). Numerical simulation of flow on circular crest stepped spillway. Applied Water Science, 12 (215), 1-10
11. Parsaie, A., Haghiabi, A. H. (2021). Uncertainty analysis of discharge coefficient of circular crested weirs. Applied Water Science, 11(2), 1-6.
12. Omidpour Alavian, T., and Majedi-Asl, M, Sohrabi, F, Shamsi, V. and Ayami, M. (2022c). Modeling and evaluation of the discharge coefficient of an arched Labyrinth with the Qnet met model method, the first modern national conference in civil and environmental engineering. Ramsar, Iran.
13. Omidpour Alavian, T., Majedi-Asl, M, Soltani, M, Mohammadi, E. and Shamsi, V. (2022b). Comparison of the hydraulic efficiency of Labyrinth Weirs with quarter-circle and semi-circular crest shape using met model method (ANN), 8th.International Labyrinth on Civil Engineering, Architecture and Urban Development / 07-09 March. 2023, Tehran, Iran.
14. Majedi Asl, M., Omidpour Alavian, T and Kouhdaragh, M. (2023). Comparison of The Hydraulic Efficiency of labyrinth Weirs with a Quarter and Semi-Circular Crest Shape Using Neural Networks (QNET, SVM, GEP, ANN). Iranian Journal of Irrigation and Drainage No.4, Vol. 17, Oct.-Nov. 2023, p. 787-804.
15. Majedi Asl, M., Omidpour Alavian,, Kouhdaragh, M and Shams, V. (2023).Comparison of Hydraulic Efficiency of Arched Non-linear Weirs in Plan Using GEP and SVM Neural Networks. Journal of Water and Soil Science Vol. 27, No. 3, Fall 2023, Isfahan University of Technology, Isfahan, Iran.
16. VO, N. D. (1992). Characteristics of curvilinear flow past circular-crested weirs. Ph.D. thesis, Concordia Univ., Montreal, Canada.

© 2024 by the authors. Licensee SCU, Ahvaz, Iran. This article is an open access article distributed under the terms and conditions of the Creative Commons Attribution 4.0 International (CC BY 4.0 license) (http://creativecommons.org/licenses/by/4.0/).

Journal of Hydraulic Structures
J. Hydraul. Struct., 2024; 10(1):119-126
DOI: 10.22055/jhs.2024.19078



OPEN ACCESS

The effect of slot in reducing scour depth of cylindrical bridge pier using Flow3D software

Milad Kazemian [*1]
Kazem Esmaeili [1]

Abstract

Scouring is one of the most important factors in the destruction of bridge piers. One of the ways to reduce scouring depth is to use a slot in the bridge pier. In this research, the Flow 3D model was used to simulate the effect of a slot with the same dimensions in two positions parallel to the bed and close to the water surface. The tests were performed at two relative speeds of 0.87 and 0.92. Uniform and non-cohesive bed sediments with a geometric standard deviation of 1.4 and an average diameter of 1 mm were used. The results showed that the slot created in the pier of the bridge weakens the eddies around the pier and is effective in reducing scour depth. The slot close to the surface, on average, about 6%, and the slot parallel to the bed, about 26%, are effective in reducing the maximum scour depth compared to the control pier. Also, with the increase of Froud number from 0.376 to 0.380, scour depth has increased by 11% on average.

Keywords: Scour, Bridge Pier, Near-Surface Slot, Bed-Level Slot, Flow 3D Model.

Received: 09 November 2023; Accepted: 16 April 2024

1. Introduction

Scouring is a phenomenon that occurs due to the interaction of flow conditions and the movement of sediments on the rivers and waterways due to the passage of the current. The depth caused by bed erosion compared to the original bed is called scour depth [1]. Over the past 30 years, more than 1,000 of the 600,000 bridges built in the United States have been destroyed, 90% of which were due to scour [2].

reduction methods of scouring are divided into two main categories. In the first method, the bed is reinforced and its resistance to driving forces is increased, such as the stonework of concrete protection layers, and the second method changes the flow pattern around the pier to reduce the downward flow and vortex systems that Those methods of modifying the flow say that this method can be referred to the use of Piling, collar and slot [3]. Azhari et al. (2010) simulated the scour depth around a series of three cylindrical vertical bridge foundations in a river using a three dimensional numerical model and a physical model.

* Email: m.kazem19717730@gmail.com (**Corresponding Author**)
[1]Department of water structures, Ferdowsi University of Mashhad, Mashhad, Iran.

CC BY

The results showed that the maximum depth of scour occurred around the first pier and the results of the numerical model are in good agreement with the information obtained from the physical model [4]. Qaderi and Abbasi (2019) investigated the local scouring of the airfoil pier by considering the collar using a numerical model. The results showed that the use of the collar in the pier reduces the maximum scour depth in front of the bridge pier and reduces the eddies behind the pier [5]. Nazari Sharabian (2020) investigated the effect of piles with different configurations on reducing scour depth of bridge pier using folw 3D model. The results showed that the models that have a single pile installed in front of the pier and at a distance of five times the diameter of the pier are more effective in reducing scour depth [6]. Hassanzadeh et al. (2020) Using a numerical model, investigated the effect of the distance and placement of adjacent piers on the flow pattern and erosion of the sand bed around the bridge piers. By examining the changes in the distance between the piers in two cases, it was found that by reducing the distance, due to creating a wider barrier against the flow and creating a water jet between the piers, scour increases [7]. Danesh Faraz (2022) conducted the effect of cable on reducing scouring of the bridge pier using artificial neural networks and ANFIS methods. They used two types of cables with diameters of 10 and 15% of the pier diameter and twist angles of 15 and 12 degrees, respectively.

The results showed that the use of cable can reduce scouring depth by 10 and 22% respectively. And conducting tests with angles of zero, 10 and 15 degrees to the direction of the flow, showed that the pierss with an angle of 15 degrees to the flow have the greatest scour depth[8].

Many researches have been done using Flow3D numerical model on the methods of reducing scour depth around the pier of cylindrical bridge by using collar, slot in center of pier, etc. In this research, the effect of the slot around the pier body of the cylindrical bridge, in order to reduce the scour depth in two positions parallel to the bed and close to the water surface, was investigated using the Flow 3D model, which is unique from this point of view. In this research, the effect of the slot around the pier body of the cylindrical bridge, in order to reduce the scour depth in two positions parallel to the bed and close to the water surface, was investigated using the Flow 3D model, which is unique from this point of view.

2. Material and Methods

In the current research, the Flow 3D model was used to simulate the scouring of the bridge pier and the effect of the slot on it, which will be discussed further. Flow3D model is one of the most powerful models in the field of fluid dynamics. This model has the capability of three-dimensional analysis of the flow field and also has a very wide application range in problems related to fluids. And to solve the turbulent, it uses five methods of Parantel's mixing length, one-equation model, two-equation K-ε model, RNG and LES. The differential equations that must be solved in the Flow-3D model can be written in both Cartesian and cylindrical coordinates. The three-dimensional analysis of the Navier-Stokes-Reynolds equations in the Cartesian coordinate system which are solved by the finite volume method in the incompressible fluid state is in the form of relations 1 to 4.

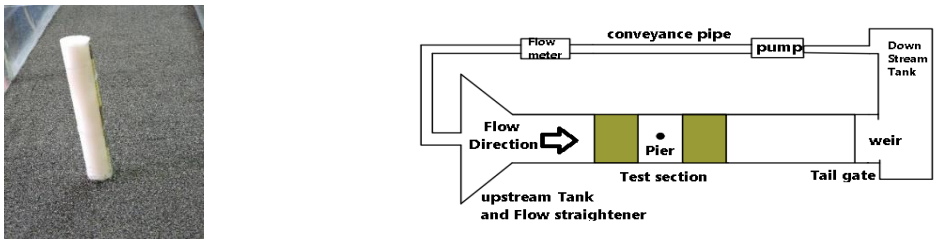
$$V_F\frac{\partial \rho}{\partial t}+\frac{\partial(\rho u A_x)}{\partial x}+\frac{\partial(\rho v A_y)}{\partial y}+\frac{\partial(\rho w A_Z)}{\partial z}=R_{SOR} \quad (1)$$

$$\frac{\partial u}{\partial t}+\frac{1}{V_F}\left(uA_x\frac{\partial u}{\partial x}+vA_y\frac{\partial u}{\partial y}+wA_z\frac{\partial u}{\partial z}\right)=-\frac{1}{\rho}\frac{\partial P}{\partial x}+G_x+f_x \quad (2)$$

$$\frac{\partial v}{\partial t}+\frac{1}{V_F}\left(uA_x\frac{\partial v}{\partial x}+vA_y\frac{\partial v}{\partial y}+wA_z\frac{\partial v}{\partial z}\right)=-\frac{1}{\rho}\frac{\partial P}{\partial y}+G_y+f_y \quad (3)$$

$$\frac{\partial w}{\partial t}+\frac{1}{V_F}\left(uA_x\frac{\partial w}{\partial x}+vA_y\frac{\partial w}{\partial y}+wA_z\frac{\partial w}{\partial z}\right)=-\frac{1}{\rho}\frac{\partial P}{\partial z}+G_z+f_z \quad (4)$$

where V_F is the fraction of the volume associated with the flow, ρ is the fluid density, (u,v,w) are the velocity components, (Ax, Ay, Az) is the fraction of the area associated with the flow, (Gx Gy, Gz) is the mass acceleration, R_{SOR} The Source term, (Fx, Fy, Fz) is the viscous acceleration in the (x, y, z) directions and p is the pressure. In this research, the laboratory results of Kazemian et al. (1400) have been used [9]. The laboratory results obtained for the control pier were carried out in a laboratory flume with a length of 10.5 meters, width and height of 0.5 meters. The flume was made of glass and polyglass and its slope was 0.001. The location of the pier was a Teflon plastic plate with a height of 0.02, a width of 0.5 and a length of 1.06 meters, and two platforms with a height of 0.12, a width of 0.5 and a length of one meter were located upstream and downstream of it. Figure 1 shows a picture of the general design of the channel and the control pier used in the laboratory.



(A) **(B)**

Figure 1. control pier (A) and Flume schematic (B)

The pier used in the experiment has a diameter of 4 cm. Relative velocity is defined as the ratio of flow velocity to critical velocity. In this experiment, two relative speeds of 0.870 and 0.92 were used.

Bed sediments were used in a uniform and non-cohesive form with an average diameter of 1 mm and a geometric standard deviation of 1.4. And also the sediment beds were 15 cm high.

In this research, AutoCAD software was used to draw the geometry of the channel and pier. To save the calculation time, it was simulated in about 1.5 meters of the length of the laboratory channel. Figure 2 shows the geometry of the created channel, bed and pier.

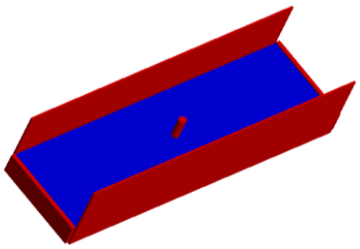
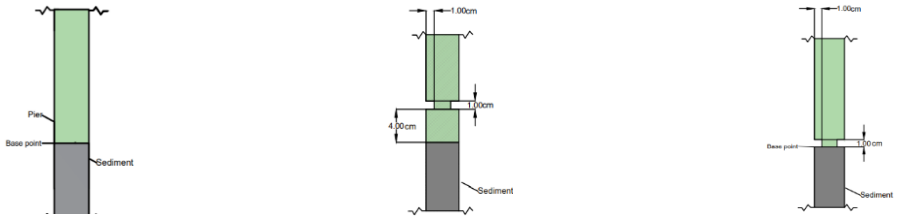


Figure 2. Geometry created by AutoCAD software

The piers used in the numerical model include three types of piers. The S0 pier without slot as a control pier has the same characteristics as the laboratory sample in order to validate the results. The height and indentation of the slot was introduced as a measure of the diameter of the pier and it was considered as a quarter of the diameter of the pier. The pier S1 has a slot with a height of one centimeter all around the pier and the position is 4 cm away from the bed. The S2 base has a slot with the same specifications as the S1 pier, and is positioned level with the bed. The indentation depth of the slot in both types of sloted pier is one centimeter. In such a way that the diameter of the base at the place of the slot is 3 cm with a decrease of one centimeter. The specifications of the piers in Figure 3 are shown.



(A) **(B)** **(C)**

Figure 3. control pier (A), pier with a slot close to the surface (B) and pier with a slot parallel to the bed (C)

The information related to sediments, fluid and other effective parameters were entered into the software.

Also, flow rate and flow depth were introduced to the software as initial conditions. The geometry of the model was entered into the software, and for more accuracy in obtaining scour depth and showing the characteristics of the pier, a another block was considered around the bridge pier. The boundary conditions defined in this study are shown in Figure 4, where the inlet boundary condition (Xmin) was considered as a constant discharge (Q). In the laboratory model, at the inlet boundary, water flows with a known depth and discharge, and for this reason, the inlet condition of a constant discharge with a constant water height was used. For the outlet of the channel (Xmax), the boundary condition was considered in such a way that the fluid is in contact with the air. As mentioned, to reduce the calculation time, 1.5 m of the length of the laboratory channel was simulated in such a way that the pier is placed in the middle of the channel. The boundary of meshing on the bed of the channel is one centimeter above the bed (within the sediments), and in the width of the channel one centimeter on both sides of the channel wall (according to the distance of one centimeter from the width of the channel on both sides, the boundarys of the meshing are inside the water and instead of 50 cm 48 cm was considered.) was placed. These boundaries were defined as symmetry (the conditions outside the solution network are considered exactly the same as the conditions on the internal boundary of the domain). This type of boundary condition is used in symmetric simulations. The free surface of the fluid was also considered symmetrical.

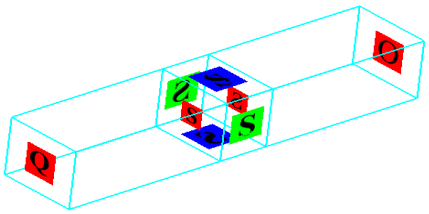


Figure 4. created boundary conditions

RNG model of turbulence has been used to model turbulence in this research. Compared to the k- Ɛ turbulence model, this model needs fewer experimental constants and has shown better performance for simulating regions with flow separation [10]. In addition, three models k-Ɛ, RNG and LES were investigated to obtain the maximum scour depth under the same conditions, and the results showed that the RNG model has a better match with the experimental observations.

3. Results and Discussion

One of the most important parts of numerical solution is determining the size of computing domains or the size of cells in meshing. The number of cells in a mesh depends on the determined range and size and affects the accuracy and time of calculations. As a result, it is necessary to

adopt a suitable meshing that both meets the accuracy required in the calculations and is within the conventional limits in terms of the calculation time. Cartesian meshing is used in this numerical simulation. Appropriate meshing was investigated in two modes of uniform and non-uniform meshing, and then according to the geometry of the model and also the sensitivity to observe as well as possible the maximum depth of scour and its location, non-uniform meshing was done around the pier of the bridge. So that the pier and its surroundings have a finer mesh.

To determine the optimal number of meshes, the meshes started from 50,000 and increased with steps of 50,000. The results showed that for meshes less than 400,000, the rigid boundaris of the channel as well as the slot in the pier could not be identified completely by the model. But gradually, with the increase in the number of cells, the detection ability increased. For example, the identified solid boundaries for the channel, bridge pier and bed with the number of 200 thousand meshes and 600 thousand meshes are presented in Figure 5. Research showed that for a mesh number of more than 500,000, the software can fully recognize all parts of the channel. For this reason, for meshes more than 500 thousand, the compatibility of the model results with the laboratory results was considered. For 500, 550, 600, 650, 700 and 750 thousand meshes, the relative error between the modeling results and the laboratory results related to the control pier for the relative flow speed of 0.92 is presented in Table 1.

Table 1. The maximum scour depth in the exoerimental model and the numerical model with a relative speed of 0.92

The number of meshes	Maximum scouring depth in the experimental model, cm	Maximum scouring depth in the numerical model, cm	Relative error, %
500000	6.2	3.2	48
550000	6.2	3.3	46
600000	6.2	4.6	25
650000	6.2	6	3
700000	6.2	6	3
750000	6.2	6	3

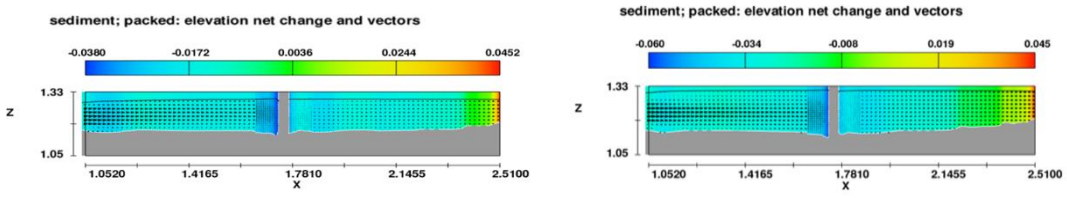


(A) **(B)**

Figure 5. Shows the mesh created in the software for 200 thousand meshes (A) and 600 thousand mesh (B)

For the number of mesh equal to 650 thousand, the relative error is equal to 3% and with the increase of the number of mesh to 750 thousand, there was no significant change in the maximum scour depth. Therefore, to reduce the calculations, the number of meshes equal to 650 thousand was chosen as the optimal number of meshes, and then all the numerical simulations were performed with 650 thousand meshes. It should be noted that the data of the maximum scour depth in the above table for the numerical model are in the test time of 800 seconds. The duration of the test should be chosen in such a way that the maximum scour depth can be reached and balance can be created in the scour hole and at the around pier. For this purpose, the test time was done starting from 400 seconds and adding a step of 200 seconds for different meshing. The results showed that for a time of 800 seconds and an optimal mesh of 650 thousand, the relative error is about three percent. Also, by increasing the test time to 1000 seconds, no effect was observed on

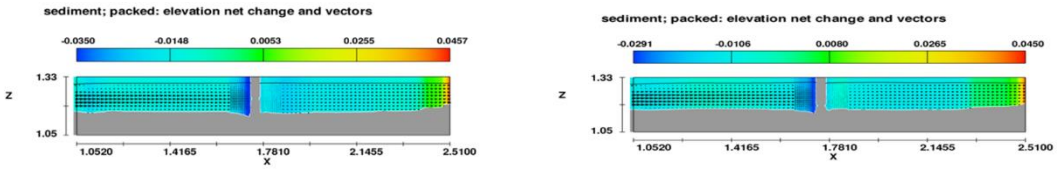
the test results. Therefore, this time was considered as the test time. The purpose of this research is the effect of slots in reducing the scour depth of the bridge pier and the comparison of scour in the sloted pier and control. Therefore, considering that 60% of the scouring depth occurred in 400 seconds, this time was considered as the test time to save calculation time. Figure 6 shows the maximum scour depth with the optimal mesh of 650,000 at times of 400 seconds and 800 seconds.



(A) **(B)**

Figure 6. The maximum scouring depth after 400 seconds (A) and 800 seconds (B)

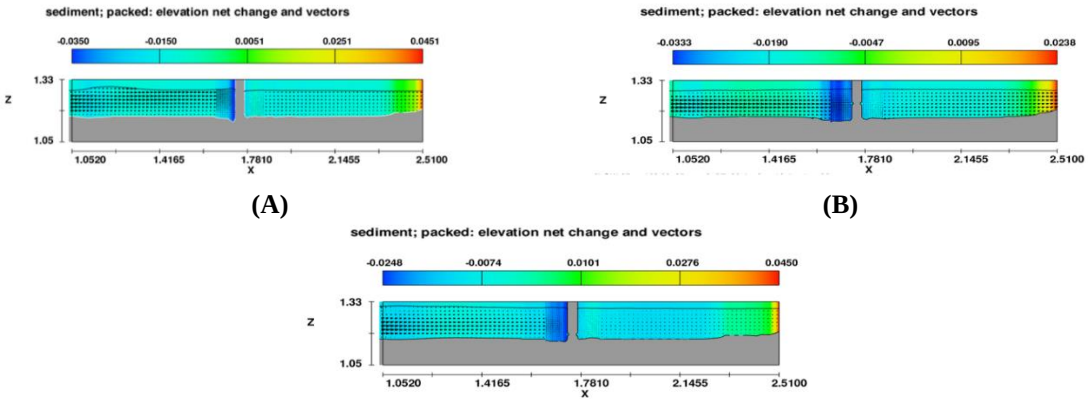
The comparison of the maximum scour depth at the relative speed of 0.92 in piers S_1 and S_2 in 400 seconds is shown in Figure 7. According to the results obtained at the relative speed of 0.92, the pier with the slot close to the surface (S_1) is about 8% and the pier with the slot parallel to the bed (S_2) is about 24% compared to the control pier had effective in reducing the maximum scour depth.



(A) **(B)**

Figure 7. The maximum scouring depth in pier S1 (A) and pier S2 (B) at relative speed of 0.92

The comparison of the maximum scour depth in foundations S_0, S_1 and S_2 with a relative speed of 0.87 is shown in Figure 8. According to the results obtained at a relative speed of 0.87 the slot close to the surface has an effect of 4.8% and the slot parallel to the bed has an effect of 29% compared to the control pier in reducing scour depth. Also, with the increase in flow rate and as a result the relative speed increase, scouring depth has increased in different pier models.



(A) **(B)**

(C)

Figure 8. The maximum scouring depth with a relative speed of 0.870 in the control pier (A), the pier with a slot close to the surface (B) and the pier with a slot close to the bed (C)

Froude number in the rectangular channel is defined as the relation 5.

$$Fr = \frac{V}{\sqrt{gy}} \quad (5)$$

where V is the speed of the flow, g is the acceleration of gravity and y is the depth of the flow. Figure 9 shows the effects of increasing the Froude number on the maximum scour depth in the control pier (S_0), the pier with a slot close to the surface (S_1) and the slot parallel to the bed (S2). The results showed that with the increase of the Froude number from 0.376 to 0.380, the maximum scour depth in piers S_0, S_1 and S_2 has increased by about 8, 6 and 20 percent, respectively.

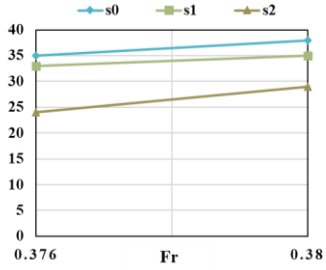
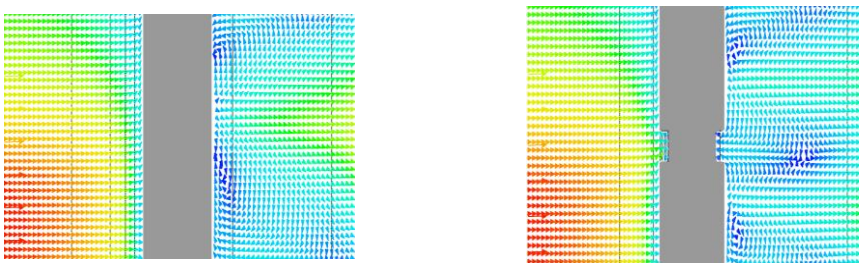


Figure 9. The effects of increasing Froude number on scour depth in different piers

Figure 10 shows the velocity vectors in the control pier and the pier with a slot close to the surface. According to the figure, the results showed that the use of slots around the bridge pier weakens the eddies around the bridge pier as the main factor of scouring phenomenon and also reduces the flow speed and Froud number in that area.



(A) **(B)**

Figure 10. Velocity vectors around the control pier (A) and the pier with a slot close to the surface (B)

4. Conclusion

In general, it can be said that with the increase in the flow intensity and consequently the Froude number and flow speed, the scour depth will increase. With the increase of relative speed from 0.87 to 0.92, scouring depth has increased by 11% on average. The results showed that in different relative velocities, on average, the slots around the pier in the position close to the water surface (S1) are 6% and in the position parallel to the bed (S2) are effective in reducing the maximum depth of scouring by 26%. In general, the use of slots around the bridge pier weakens the eddies around the bridge pier and the speed in that area and reduces scour depth.

References

1. Shafaei bajestan, M. (2013). Hydraulic of sediment transport. 4nd ed., Shahid Chamran University of Ahvaz Publications. (in Persian)
2. Sumer, B.M. and Fredsoe, J. (2002). *The mechanics of scour in the marine environment*. Advanced series on ocean engineering,vol 17.World Scientific.
3. Mashahir, M. B and Zarrati, A. R. (2002). Effect of Collar on Time Development of Scouring around *Rectangular Bridge Piers*. International Journal of Engineering, Transactions B: Applications 25(1©):11-17.
4. Azhari, A. and Saghravani, S.F. and Mohammadnezhad, B.A., (2010), "*3D Numerical modelling of local scour around the cylindrical bridge piers*," XVIII International Conference on Water Resources CMWR 2010 J. Carrera (Ed) CIMNE, Barcelona.
5. Ghaderi, A., & Abbasi, S. (2019). *CFD simulation of local scouring around airfoil-shaped bridge piers with and without collar*. *Sādhanā*, *44*, 1-12.
6. Nazari-Sharabian, M., Nazari-Sharabian, A., Karakouzian, M., & Karami, M. (2020). *Sacrificial piles as scour countermeasures in river bridges a numerical study using flow-3D*. Civil Engineering Journal, 6(6), 1091.
7. Hasanzadeh, Y. Kardan, N. and Tamizi, A., (2020). *Numerical study of the effect of the distance and the placement of the adjacent piers on the flow pattern and erosion of the sand bed around the bridge piers.* Iran Water and Soil Research (Agricultural Sciences of Iran), 51(7), 1753-1737. SID. (in Persian)
8. Daneshfaraz, R., Abam, M., Heidarpour, M., Abbasi, S., Seifollahi, M., & Abraham, J. (2022). *The impact of cables on local scouring of bridge piers using experimental study and ANN, ANFIS algorithms*. *Water Supply*, *22*(1), 1075-1093.
9. kazemian, M., Gohari, S., & shahverdi, K. (2021). *The Effect of Height and Vertical Position of Slot on the Reduction of Scour Depth around Cylindrical Bridge Pier in Uniform and Non-uniform Sediments*. *Journal of Hydraulics*, *16*(4), 37-48. doi: 10.30482/jhyd.2021.285672.1527. (in Persian)
10. Sicilian JM, Hirt CW and Harper RP, (1987). FLOW-3D: *Computational modeling power for scientists and engineers*. Report FSI-87-00-1, Flow Science, Los Alamos, NM.

© 2024 by the authors. Licensee SCU, Ahvaz, Iran. This article is an open access article distributed under the terms and conditions of the Creative Commons Attribution 4.0 International (CC BY 4.0 license) (http://creativecommons.org/licenses/by/4.0/).

Journal of Hydraulic Structures

Volume 10 – Issue 2 – April 2024

Contents:

01 Editorial: Special Issue of 22nd Iranian Conference on Hydraulics

Hamid R. Ghafouri

02 Predicting Morphological Changes in Rivers Using Image Processing (Case Study: Qizil Ouzan River)

Jafar Chabokpour; Morteza Raji

11 Performance Evaluation of Artificial Intelligence Models in Estimating the Discharge Coefficient of Labyrinth Weirs with Semicircular Crests

Hamed Heydarzadeh; Sarvenaz Asef; Jafar Chabokpour; Reza Norouzi

20 Laboratory investigation of the removal pattern of salinity from the base of coastal reservoirs during the first water impounding

Shaghayegh Pourbabak; Hojjat Ahmadi; Amir Raouf; Shuqing Yang

30 Modeling of discharge Coefficient of nonlinear weirs with QNET and SVM methods

Mahdi Majedi-Asl; Tohid Omidpour Alavian; Yousef Seyfari; Mehdi Kouhdaragh

46 Investigating and predicting hydraulic jump energy loss with threshold (Experimental and regression analysis)

Hamidreza Abbaszadeh; Parisa Ebadzadeh; Rasoul Daneshfaraz; Reza Norouzi

55 Reducing the extent of vortices upstream of the sliding valve

Parisa Ebadzadeh; Hamidreza Abbaszadeh; Rasoul Daneshfaraz; Reza Norouzi

62 Determining Thermal Stratification of Zayandeh Roud Dam Reservoirs Using Two-Dimensional CE-QUAL-W2 Model

Negar Varshabi; Ramtin Moeini

72 Investigating sediment changes during dry and wet periods at both upstream and downstream stations of the Karkheh Dam

Somayeh Rezaeimanesh; Sara Parvizi; Ali Talebi

82 Laboratory investigation of the effect of hysteresis phenomenon of supercritical flow on the rough bed on the relative residual energy parameter

Ehsan Aminvash; Rasoul Daneshfaraz; Sina Sadeghfam; Seyed Bahman Mousavi

93 Mapping Vulnerability of aquifer to saltwater intrusion using fuzzy membership function

Marjan Moazamnia; Sina Sadeghfam; Alireza Babaeian Amini

106 Numerical investigation on the hydraulic parameters' effects on the circular-crested weir

Mahdi Majedi-Asl; Hadi Arvanaghi; Mehdi Fuladipanah; Omid Ghasemzadeh; Tohid Omidpour Alavian

119 The effect of slot in reducing scour depth of cylindrical bridge pier using Flow3D software

Milad Kazemian; Kazem Esmaeili

Shahid Chamran University of Ahvaz